BULGARIAN CHEMICAL COMMUNICATIONS

Investigation on the adsorption mechanism of copper (II) ions onto a biosorbent based on lemon balm

L. P. Ivanova, P. S. Vassileva, V. G. Koleva, A. K. Detcheva*

Institute of General and Inorganic Chemistry, Bulgarian Academy of Sciences, Acad. Georgi Bonchev Str., Bl. 11, 1113, Sofia, Bulgaria

In the present work an attempt is made to elucidate the mechanism of Cu(II) adsorption on a plant material based on lemon balm. Batch experiments were carried out in order to study the effects of acidity, contact time and initial metal concentration on Cu(II) removal. Langmuir, Freundlich and Dubinin-Radushkevich isotherm models were used to explain equilibrium experimental data and the maximum adsorption capacity was calculated. The mechanism of retention of copper ions on the biosorbent surface was studied by means of SEM, FTIR and XPS methods, as well as low-temperature nitrogen adsorption. Desorption experiments were also performed. It was proved that the investigated plant material could be used for the removal of copper ions from contaminated waters.

Keywords: Lemon balm, biosorption, copper ions, SEM, FTIR, XPS

INTRODUCTION

Heavy metal pollution is one of the most important problems around the world nowadays due to their toxic effects and persistence [1]. Copper is among the most common contaminants, found in surface water and groundwater, as well as industrial wastewater [2]. Copper pollution is generated from various sources and has resulted in an accumulation of large quantities of liquid effluents, loaded with high levels of toxic metallic species. It is of great importance to remove or reduce the concentration of copper ions before their discharge into aquatic environments, because it is harmful for living beings, especially for water organisms. Conventional treatment techniques like chemical precipitation, activated carbon adsorption, reverse osmosis, ion-exchange, membrane processes, ultrafiltration, solvent extraction, electrochemical processes, etc, used for removal of metal ions from aqueous solutions, have disadvantages and biosorption can be a reliable low-cost and eco-friendly alternative of these methods [3, 4]. The mechanism of this process relies on sorption of metal ions from aqueous solution to chemical functional groups present on the surface of the cell wall of the biomass [5]. It is known that lignocellulosic materials have good sorptive characteristics due to their structure. A number of studies discuss the use of biosorbents for heavy metal removal, but there is a growing interest in utilizing biosorbents, based on ethereal oil plants [6, 7].

Lemon balm (*Melissa officinalis* L.) as a representative of the ethereal oil plants is a perennial herbaceous plant in the mint family, native to South-Central Europe, the Mediterranean Basin, Iran, and Central Asia, but now naturalized elsewhere. Different parts of the plant are used in folk medicine for their digestive, carminative, antispasmodic, sedative, analgesic, tonic, and diuretic properties. Various studies have shown that it also possesses high antioxidant activity through its chemical compounds including high amount of flavonoids, rosmaric acid, gallic acid, phenolic contents [8]. Lemon balm, like other herbs, has multicomponent composition, a large part of which comprises cellulose, hemicellulose, pectin and lignin [6, 7]. Materials derived from lemon balm biomass are not used as biosorbents for metal ions until now, but they were used for remediation of polluted soils [9, 10].

In the present work a plant material based on *Melissa officinalis* L., denoted as MO was examined as a biosorbent for copper(II) ions. An attempt for elucidation of the adsorption mechanism using FTIR and XPS methods, as well as linear isotherm models has also been performed [11-13]. Desorption studies were carried out to estimate the possibility of regeneration of the used biosorbent.

EXPERIMENTAL

Materials and methods

The commercially available leaves of lemon balm were washed several times with distilled water to remove surface-adhered and water-soluble particles and dried at 60°C in an electric oven for 48 h. Thus prepared material was milled in an electric grinder to a size of particles below 200 µm. No other physical or chemical treatment was performed.

* To whom all correspondence should be sent:
E-mail: albena@svr.igic.bas.bg

The surface morphology of the biomaterial was observed on a scanning electron microscope (SEM) - Tescan instrument model SEM/FIB Lyra I XMU. The porous structure of the studied materials was investigated by low-temperature (–196°C) nitrogen adsorption using a Quantachrome Nova 1200 apparatus (Quantachrome Instruments, USA). Before nitrogen adsorption, the samples were degassed at 80°C for 3 h. Specific surface area was calculated on the basis of the Brunauer–Emmett–Teller (BET) equation; the pore size distribution was calculated according to the Barrett-Joyner-Halenda (BJH) method. The total pore volume was estimated in accordance with the rule of Gurvich at a relative pressure of 0.99. The volume of the micropores was calculated using the Dubinin-Radushkevich equation and the volume of the mesopores by the difference of V_{total}–V_{micro}. The Fourier transform-infrared (FTIR) spectra of the samples (raw MO and MO after Cu(II) sorption - MOS) were taken with a Nicolet spectrometer in the region of 4000–400 cm^{-1} using KBr pellets (resolution 2 cm^{-1}, 64 scans). Prior to the spectra measurements, the samples were pre-heated in a vacuum dryer at 120°C for 48 hours in order to eliminate partly the adsorbed water molecules. For each sample at least two KBr pellets were measured. XPS investigations were carried out by means of ESCALAB MKII spectrometer with Al Kα (unmonochromatized) source at 1486.6 eV with a total instrumental resolution of ~1 eV, under a base pressure of 10^{-8} mbar. The C1s, O1s, N1s and Cu2p photoelectron lines were recorded and calibrated to the C1s line at 285.0 eV. XPSPEAK 4.0 fitting program was used for deconvolution of the photoelectron peaks. All data were recorded at 45° take-off angle.

Adsorption studies

Batch experiments were performed to determine the adsorption properties of the studied material. They were carried out using stoppered 50-mL Erlenmeyer flasks containing about 0.2 g of sample and 20 mL of aqueous solution of Cu(II) ions. The mixture was shaken at room temperature (20°C) by an automatic shaker. After the experiment the biomaterial was removed by filtration through a Millipore filter (0.2 μm). The initial and equilibrium copper concentrations were determined on a Prodigy 7 ICP-OES spectrometer (Teledyne Leeman Labs, USA) and determinations were performed by the interference-free Cu-analytical line of 217.894 nm.

The amount of adsorbed copper ions per gram sorbent Q_e was calculated using the following relationship:

$$Q_e = (C_0 - C_e) * V/m \qquad (1)$$

where C_0 = initial concentration (mg L^{-1}), C_e = equilibrium concentration (mg L^{-1}), m = mass of adsorbent (g), and V = solution volume (L). All measurements were replicated and the average results were discussed.

The effect of contact time on the amount of adsorbed Cu^{2+} ions with concentrations of 200 mg L^{-1} was studied at pH 4.0. The effect of the medium acidity on Cu^{2+} removal efficiency was investigated over the pH range 1.8–5.0 with concentration of 200 mg L^{-1} (pH-meter model pH 211, Hanna instruments, Germany). To determine the effect of the initial metal ion concentration on the adsorption capacity, Cu^{2+} concentrations in the range of 50–500 mg L^{-1} at pH 4.0 were chosen. The initial pH of the working standard solutions was adjusted to the required value with 0.1 M HCl and NaOH solutions before mixing the suspension.

Desorption of copper from MO sorbent was studied in a batch system using three eluents: 0.1 M HNO_3, 1 M HNO_3 and 0.1 M EDTA. Pre-adsorbed MO (0.1 g) was added to 10 mL of the above mentioned eluents and stirred for 24 h. The eluents were then filtered and tested for desorbed copper.

Working standard solutions of Cu^{2+} ions with concentrations of 50–500 mg L^{-1} were prepared by stepwise dilution of a stock solution with concentration of 1000 mg Cu L^{-1} ($CuCl_2$ in H_2O), Titrisol® Merck, (Darmstadt, Germany). All reagents used throughout the experiments were of analytical grade.

RESULTS AND DISCUSSION

Texture parameters

The calculated textural parameters of MO are summarized in Table 1. The studied material shows relatively low surface area and total pore volume. The calculated average pore diameter (6.4 nm) corresponds to a mesoporous structure. The measurement of slurry pH indicates that the sample displays pH values of 5.8, which points to slightly acidic reaction of the aqueous suspension.

Table 1. Texture characteristics and pH of the water leachates of MO

BET surface area, $m^2 g^{-1}$	Pore volume, $cm^3 g^{-1}$	Micropore volume, $cm^3 g^{-1}$	Mesopore volume, $cm^3 g^{-1}$	Average pore diameter, nm	pH
0.8	0.001	-	0.001	6.4	5.8

Effect of acidity and contact time

In the present study the removal of copper ions strongly depends on the acidity of the initial solutions. Upon increasing the pH values the amounts of adsorbed ions increased and the optimum pH range was found to be about 4.0 (Fig. 1a).

The adsorbed amount of Cu(II) ions increased rapidly within the first 2 min and remained constant after 10 min, thus indicating that the kinetics is fast and the equilibrium is reached (Fig. 1b). This is a proof for the good affinity of MO towards Cu(II) ions.
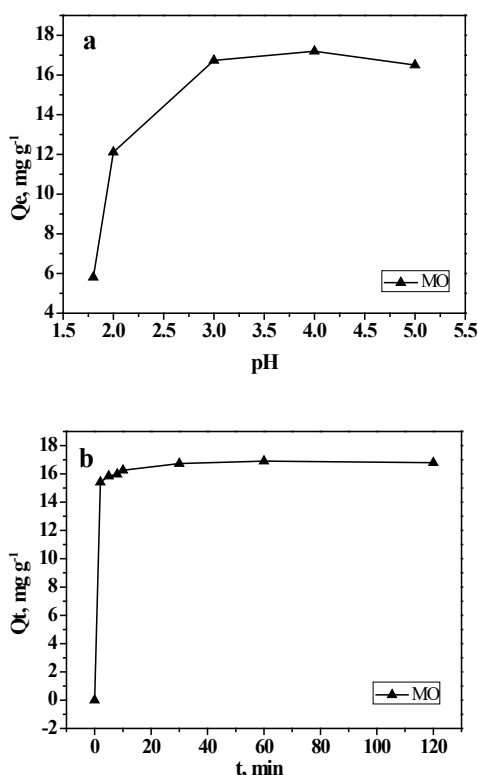

Fig. 1. Effect of acidity (a) and contact time (b) on the amount of adsorbed Cu(II) ions.

Adsorption isotherms

The effect of the initial copper ion concentration on the adsorption capacity was determined using Cu(II) concentrations in the range of 50-500 mg L^{-1} at pH 4.0 (Fig. 2) and three isotherm models were employed to analyze the batch experimental data - the Langmuir, Freundlich and Dubinin-Radushkevich [7].

The linear form of the Langmuir isotherm is expressed by the following equation:

$$C_e/Q_e = 1/K_L Q_0 + C_e/Q_0 \quad (2)$$

where C_e is the concentration of metal ions in the equilibrium solution (mg L^{-1}), Q_e is the amount of ion adsorbed (mg) per unit mass of adsorbent (g), Q_0, the maximum adsorption capacity (mg g^{-1}), K_L is the Langmuir constant related to the enthalpy of the process.

The Langmuir model supports the following hypothesis: the adsorbent has a uniform surface: absence of interactions between the solid molecules; the sorption process takes place in a monolayer.

The linear form of the Freundlich model is expressed by the following equation:

$$\ln Q_e = \ln k_F + (1/n) \ln C_e \quad (3)$$

where k_F is a constant related to the adsorption capacity and n is an empirical parameter related to the intensity of adsorption.

The Freundlich model is valid for heterogeneous surfaces and predicts an increase in the concentration of the ionic species adsorbed onto the surface of the solid when increasing the concentration of certain species in the liquid phase.

The Dubinin–Radushkevich isotherm reveals the adsorption mechanism based on the potential theory. The linear form of the Dubinin–Radushkevich isotherm is described by the following equation:

$$\ln Q_e = \ln Q_m - \beta \varepsilon^2 \quad (4)$$

where Q_e is the amount of metal ion (mg) adsorbed per unit mass of adsorbent (g), Q_m is the maximum adsorption capacity (mg g^{-1}), β is the adsorption energy constant (mol^2 J^{-2}), and ε is the Polanyi potential, described as:

$$\varepsilon = RT \ln(1+1/C_e) \quad (5)$$

where R is the gas constant (J $mol^{-1}K^{-1}$) and T is the temperature (K). The mean adsorption energy E (kJ mol^{-1}) can be calculated using the parameter β as follows:

$$E = 1/(-2\beta)^{1/2} \quad (6)$$

This is a substantial step to predict the mechanism of adsorption. Langmuir, Freundlich and Dubinin-Radushkevich equations are based on entirely different principles and the fact that the experimental results fit to one or other equation indicates the most probable adsorption mechanism.

Table 2. Constants of Langmuir, Freundlich and Dubinin-Radushkevich isotherms for the adsorption of Cu(II) ions onto the biomaterial MO

Langmuir parameters			Freundlich parameters			Dubinin–Radushkevich parameters		
Q_0 (mg g^{-1})	K1 (L mg^{-1})	r^2	kF (mg^{1-n}L^{n}g^{-1})	n (L mg^{-1})	r^2	Qm$_{(0)}$ (mg g^{-1})	E (kJ mol^{-1})	r^2
59.95	0.031	0.9709	1.08	1.58	0.9525	27.42	0.146	0.7970
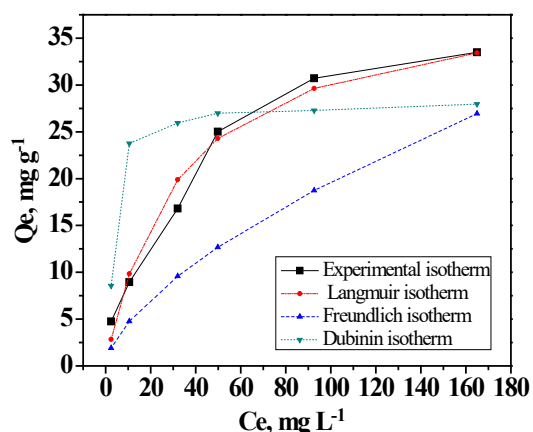
Fig. 2. Adsorption isotherms towards Cu(II) ions

It is important to note that every model has its own limitations in accurately describing equilibrium data. The corresponding parameters are given in Table 2. The correlation coefficients (r^2) showed that Langmuir model most adequately describes the adsorption process. This means that the surface of the investigated biomaterial is homogeneous, there are no interactions between the adsorbed molecules and the uptake of copper ions occurs by monolayer adsorption. The calculated values for non-linear chi-square test χ^2, calculated as it is described by Gentscheva et al. [14] (0.0051, 0.3074 and 0.0362 for Langmuir, Freundlich and Dubinin-Radushkevich equations, respectively) confirm this assumption. The smaller the value of χ^2, the better the experimental data with the given model are described.

The non-linear dependences of the amount of adsorbed Cu(II) ions from the equilibrium concentration using Langmuir, Freundlich and Dubinin-Radushkevich models and experimental data are given in Fig. 2. The constant k_F is an approximate indicator of adsorption capacity, while 1/n is a function of the strength of adsorption in the adsorption process. 1/n is a heterogeneity parameter, the smaller 1/n, the greater is the expected heterogeneity [15]. If n is between one and ten, this indicates a favorable sorption process [16]. From the data in Table 2, the value of n=1.58 indicates that the

adsorption of Cu(II) onto MO is favorable. On the other hand, the linear Langmuir model is usually applied for calculation of maximum adsorption capacity. In the present study the maximum adsorption capacity for copper ions was found to be 59.95 mg g^{-1}. The adsorption capacity of lemon balm is compared with those reported in literature [7, 11, 17-23] (Table 3). It is evident that the biomaterial MO displays reasonably good adsorption capacity for Cu(II) and it could be used as potential adsorbent for the effective removal of these ions from contaminated aqueous solutions.

Table 3. Comparison of adsorption capacities with respect to Cu(II) ions in the present study with those reported in the literature.

Biosorbent	Qmax (mg g^{-1})	References
Watermelon rind	5.73	Liu et al. [17]
Banana peels	8.24	Liu et al. [17]
Sugarcane bagasse	9.48	Liu et al. [17]
Lagenaria vulgaris shell	12.15	Stanković et al. [18]
Chestnut shell	12.56	Yao et al. [19]
Persimmon leaves	19.42	Lee and Choi [20]
Eichhornia crassipes	22.70	Zheng et al. [11]
Achillea millefolium L.	28.11	Vassileva et al. [7]
Thymus vulgaris L.	38.93	Ivanova et al. [21]
Banana leaves	48.7	Darweesh et al. [22]
Ocimum bacilicum seeds	73.10	Adeel et al. [23]
Melissa officinalis L.	59.95	present study

Furthermore, desorption studies have also been performed. The Cu(II) ions adsorbed onto the

investigated biosorbent were eluted with 0.1M HNO₃, 1M HNO₃ and 0.1M EDTA. Dilute HNO₃ could not be used for desorption of Cu(II) ions (34% desorption). Both eluting agents 1M HNO₃ and 0.1M EDTA showed higher, equal recovery efficiency of 100%.

SEM analysis

The morphology and structure of the biosorbent MO before and after Cu(II) adsorption was investigated with SEM (Fig. 3). The SEM micrographs show that the investigated biomaterial is of rough and heterogeneous morphology, containing a large number of pores of different size. This type surface is expected to favor the sorption of various ions in the different parts of the biosorbent. As can be seen, the adsorbed copper ions (marked in green) are distributed homogeneously on the biosorbent surface.
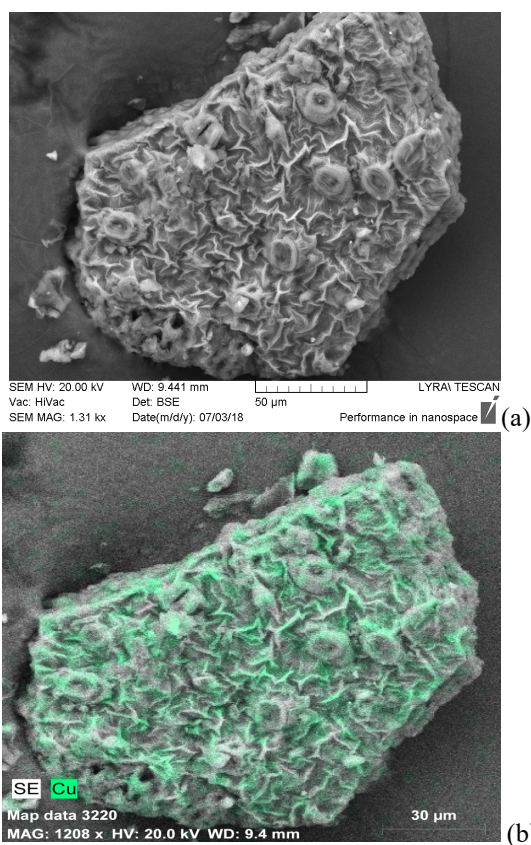

(a)

(b)

Fig. 3. Scanning electron micrographs of the surface of MO before (a) and after (b) Cu(II) adsorption, respectively

FTIR analysis

FTIR spectroscopy was used to obtain information about the functional groups from the plant material responsible for the metal ion sorption. On Figure 5 the IR spectrum of raw MO and that after Cu(II) adsorption (MOS) are compared. For a better understanding, the bands affected by the

Cu(II) retention are marked by red asterisk. Despite the compositional difference, the spectral picture observed for raw MO resembles those reported for other plant materials [11-13, 24]. Lemon balm, like other herbs, has multicomponent composition. In addition to the common constituents of the plant cells (cellulose, hemicellulose, pectin and lignin) over 100 compounds have been identified in lemon balm [25, 26]. Phytochemical investigations on MO have revealed that the main components are: a large number phenolic acids (more than 15), particularly derivatives of hydroxycinnamic acid; tannins; flavonoids; monoterpene glycosides; sesquiterpenes and essential oils [26]. The rich multicomponent nature of MO determines a complex IR spectroscopic picture, which is characterized by intensive overlapping of a huge number of bands associated with vibrations of the various structure units building its individual constituents (Fig. 4).
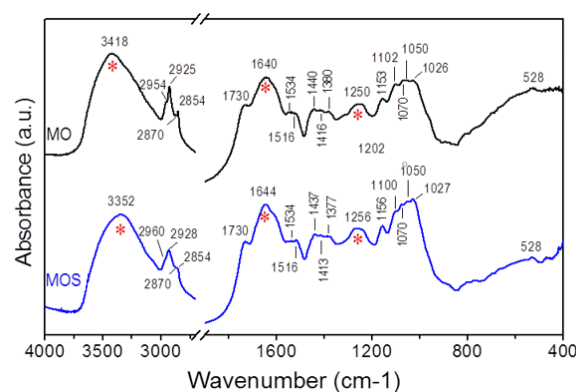

Fig. 4. FTIR spectra of raw MO and after Cu(II) biosorption process (MOS).

The hydroxyl groups from different phenolic structures, COOH groups and water molecules, all involved in hydrogen bonds, give rise to the strong band centered at 3418 cm^{-1} (O-H stretching vibrations). The presence of methylene, methyl and unconjugated carbonyl groups is doubtless: bands in the regions of 2960-2850 cm^{-1} (C-H stretching vibrations) and 1440-1380 cm^{-1} (C-H bending vibrations) and the band at 1730 cm^{-1} (C=O stretches). The strong absorption at 1640 cm^{-1} is attributed to the stretching vibrations of C=C double bonds (isolated and conjugated), ring conjugated C=O bonds and C-O bonds in carboxylate groups. The bands at 1534 and 1516 cm^{-1} can be related to the aromatic ring vibrations and C-O stretching modes in carboxylate groups. The stretching vibrations ν(C−O) in both phenolic OH and COOH groups plus ν(C−O−C) stretching vibrations in esters and aromatic ethers are mainly responsible for the band around 1250 cm^{-1}. The spectral picture in the

region of 1150 - 1020 cm^{-1} also has very complex origin: ν(C–O) stretching modes in alcoholic C-OH groups, ν(C–O–C) stretching modes in esters and aliphatic ethers, cyclic ring vibrations, aromatic C-H bending and CH$_3$ bending vibrations. The broad asymmetric absorption observed below 850 cm^{-1} is a result of intensive overlapping of bands associated with bending vibrations of different groups (aromatic C-H, O-H, =CH, C-C rings), skeleton deformations of aromatic and unsaturated structures, etc.

From the spectroscopic analysis it can be concluded that MO offers many oxygen-containing functional groups which are able to interact with the Cu(II) ions. The comparison of the IR spectra of the plant material before and after treatment indicates that the IR spectrum is very little affected by the Cu(II) retention. The overall spectral picture remains almost the same and only a frequency shift of three bands can be surely detected (shift greater than the instrumental resolution). These are: the one at 3423 cm^{-1} which exhibits a large low-frequency shift with 26 cm^{-1}, and the other two bands at 1640 and 1250 cm^{-1} which display a smaller high-frequency shift with 4 and 6 cm^{-1}, respectively. From the interpretation given above it follows that the spectral changes refer mainly to OH (phenolic and carboxylic ones), carbonyl and carboxyl groups. The participation of C-O-C groups from esters and aromatic ethers is not so obvious, but it cannot be fully ignored since the stretching vibrations of these groups contribute to the band at 1256 cm^{-1} as well. The observed band shifting after the copper retention gives indication for a change in the strength of intramolecular interactions of the type O-H, C-O, C=O and C-O-C which could be related with interactions between Cu(II) ions and the oxygen atoms from the functional groups.

It should be mentioned that in the literature the values of the observed band frequency shifts due to metal ion retention, including copper ions, on natural sorbents vary within broad limits, between 3 and 37 cm^{-1} as the largest shifts have been found for the ν(OH) band [11, 12, 24, 27].

In the literature different mechanisms of metal ions adsorption on herbs including complexation, ion exchange and electrostatic attraction have been discussed [27, 28] Unequivocal interpretation is very difficult, thus the retention of Cu(II) on MO cannot be attributed directly to one of them. Probably, this process is a combination of all possible interactions, pointing to its complex nature.

XPS analysis

XPS is one of the most useful tools for analyzing the adsorption interaction and the type and relative amount of chemical groups on the adsorbent surfaces. The surfaces of the investigated material – before (MO) and after adsorption of Cu(II) ions (MOS) were studied. To elucidate the retention mechanism of Cu(II) onto MO surface, the changes in the C1s, O1s and Cu2p3/2 photoelectron spectra were recorded and are presented in Figure 5 and Table 3.

In order to get an insight into the concentration of the functional groups before and after Cu(II) adsorption, a curve-fitting procedure for carbon C1s peaks was performed as follows. The high resolution C1s photoelectron peaks recorded for the examined samples were split to three components named C1, C2 and C3, respectively and related to different existing bonds on their surfaces. The major C1 peak component (at $\approx$ 285 eV) is associated to C-C bond; the second C2 peak at ~286.5 eV corresponds to the C-OH, C-O bond, or C-N; and the C3 peak situated at ~288.0 eV corresponds to O-C=O bond.
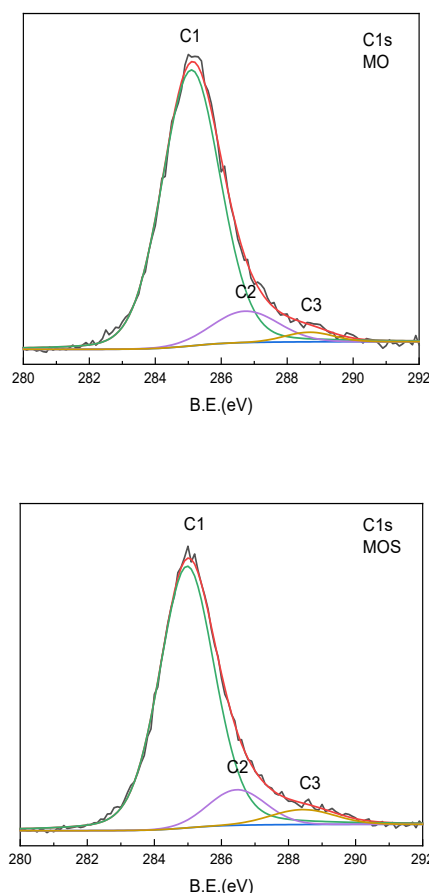

Fig. 5. C1s photoelectron spectra/binding energies (B.E.) of MO and MOS

Table 4. Calculated relative amounts of carbon functional groups present on the surface of MO and MOS

Sample	C1 C-C, %	C2 C-O-C, C-OH, C-N, %	C3 O-C=O, %	O1 C=O, %	O2 C-O, %
MO	87.1	10.5	2.4	34.6	65.4
MOS	84.2	10.8	5.0	62.3	37.7

% from total carbon and oxygen

These peaks can be assigned to C atoms in the form of C–C, C–O (alcoholic or ether), O–C–O (ether) and O–C=O (carboxylate or ester groups), respectively [11, 29]. The O1s spectra (figures not presented) show two components at around 532.5 eV and 533.5 eV. Both components can be assigned to the existence of functional groups such as C=O and C-O/C-OH, respectively, but not to Cu-O.

On the other hand, the XPS results show that the Cu2p3/2 peak has binding energy at around 933.5 eV accompanied by the satellite peak at around 943 eV, typical for Cu(II). The relative contents of C-C, C-OH or C-O/C-N and C=O functional groups changed after Cu(II) adsorption which is in accordance with the FTIR analysis. The relative amount of C-C and C=O increase after copper adsorption while the relative amount of C-O, C-OH, C-N decreases (Table 4) pointing out that the mechanism of copper ions retention on MO has a multiplex character. The contribution of XPS results to the above discussion additionally reveals the complex nature of the investigated biosorption process between Cu(II) and MO, which proved to be a combination of surface complexation, ion exchange and electrostatic attraction, in accordance with literature data [11-13].

CONCLUSIONS

Biomaterial based on lemon balm (*Melissa officinalis* L.) was evaluated as a sorbent for Cu(II) removal from aqueous media. The influence of the acidity of the initial metal ion solutions on its adsorption was investigated, and the optimal pH value was found to be about 4. The adsorption equilibrium was established within 10 min. The adsorption isotherm exhibits mainly Langmuir behaviour which assumes that the uptake of copper ions occurs on a homogeneous surface by monolayer adsorption. Desorption studies demonstrate that 1M HNO$_3$ and 0.1 M EDTA could be used as eluting agents. The maximum adsorption capacity was found to be 59.95 mg g^{-1}, showing that MO could be used as an effective biosorbent for the removal of copper ions.

The sorption mechanism was further investigated by means of FTIR and XPS. It was established that the retention of Cu(II) ions on the surface of raw MO and its biomass is a result of interactions between these ions and the OH groups from the phenolic structures and COOH groups, but the participation of esters and aromatic ether groups cannot be ignored. The adsorption proved to be a multiplex process that involves surface complexation, ion exchange and electrostatic attraction.

REFERENCES

1. I. Ugulu, *Appl. Spectrosc. Rev.*, **50**, 113 (2015).
2. M. Aryal, *Rev. Chem. Eng.*, **37**, 715 (2021).
3. H. Zhang, X. Hu, H. Lu, *Water Sci. Technol.*, **76**, 859 (2017).
4. A. A. Redha, *Arab. J. Basic Appl. Sci.*, **27**, 183 (2020).
5. K. Chojnacka, M. Mikulewicz, *TrAC – Trend. Anal. Chem.*, **116**, 254 (2019).
6. L. Ivanova, P. Vassileva, G.. Gencheva, A. Detcheva, *J. Environ. Prot. Ecol.*, **21**, 37 (2020).
7. P. S. Vassileva, L. P. Ivanova, A. K. Detcheva, *Bulg. Chem. Commun.*, **54**(A), 19 (2022)
8. S. Miraj, M. Rafiean Kopae, S. Kiani, *J. Evid. Based Complementary Altern. Med.*, **22**, 385 (2017)
9. S. A. Aransiola, U. J. J. Ijah, O. P. Abioye, J. D. Bala, *Int. J. Environ. Sci. Technol.*, **20**, 1823 (2023)
10. V. D. Zheljazkov, E. A. Jeliazkova, N. Kovacheva, A. Dzhurmanski, *Environ. Exp. Bot.*, **64**, 207 (2008)
11. J.-C. Zheng, H.-M. Feng, M. H.-W. Lam, P. K.-S. Lam, Y.-W. Ding, H.-Q. Yu, *J. Hazard. Mater.*, **171**, 780 (2009).
12. W. S. Wan Ngah, M. A. K. M. Hanafiah, *J. Environ. Sci.*, **20**, 1168 (2008).
13. X. Liu, Z.-Q. Chen, B. Han, C.-L Su, Q. Han, W.-Z. Chen, *Ecotox. Environ. Safe.*, **150**, 251 (2018).
14. G. Gentscheva, P. Vassileva, N. Marinkov, C. Tzvetkova, D. Kovacheva, *C. R. Acad. Bulg. Sci.*, **73**, 1229 (2020).

15. A. O. Dada, A. P. Olalekan, A. M. Olatunya, O. Dada, *IOSR J. Appl. Chem.,* **3**, 38 (2012).
16. P. Vassileva, D. Voykova, I. Uzunov, S. Uzunova, *C. R. Acad. Bulg. Sci*., **71**, 1192 (2018).
17. C. Liu, H. H. Ngo, W. Guo, K.-L. Tung, *Bioresour. Technol*., **119**, 349 (2012)
18. M. N. Stanković, N. S. Krstić, J. Z. Mitrović, S. M. Najdanović, M. M. Petrović, D. V. Bojić, V. D. Dimitrijević, A. L. Bojić, *New J. Chem*., **40**, 2126 (2016)
19. Z.-Y. Yao, J.-H. Qi, L.-H. Wang, *J. Hazard. Mater*., **174**, 137 (2010)
20. S.-Y. Lee, H.-J. Choi, *J. Environ. Manage*., **209**, 382 (2018)
21. L. Ivanova, P. Vassileva, A. Detcheva, *Mater. Today: Proc*., **61**, 1237 (2022)
22. M. A. Darweesh, M. Y. Elgendy, M. I. Ayad, A. M. M. Ahmed, N. M. Kamel Elsayed, W. A. Hammad, *S. Afr. J. Chem. Eng.,* **40**, 10 (2022)
23. H. M. Adeel, B. Parveen, N. Rasool, M. Riaz, K. G. Ali, Y. Gull, M. Noreen, M. Asghar, *Int. J. Chem. Biochem. Sci*., **4**, 38 (2013)
24. X. Zhu, H. Yu, H. Jia, Q. Wu, J. Liu, X. Li, *Anal. Methods*, **5**, 4460 (2013).
25. C. G. Boeriu, D. Bravo, R. J. A. Gosselink, J. E. G. van Dam, *Ind. Crop. Prod*., **20**, 205 (2004);
26. A. Shakeri, A. Sahebkar, B. Javadi, J. Ethnopharmacol., 188, 204 (2016).
27. M. Petrović, T. Šoštarić, M. Stojanović, J. Petrović, M. Mihajlović, A. Ćosović, S. Stanković, *Ecol. Eng*., **99**, 83 (2017).
28. M. Khormaei, B. Nasernejad, M. Edrisi, T. Eslamzadeh, J. *Hazard. Mater*., **149**, 269 (2007).
29. G. Vázquez, M. Calvo, M. S. Freire, J. González-Alvarez, G. Antorrena, J. *Hazard. Mater*., **172**, 1402 (2009).

In vitro corrosion behavior, mechanical properties of nano biocomposite coated 316L SS for dental applications

S. Mohandoss[1*], S. Suja[2], S.P. Srinivasan[1], S. Chitradevi[3], B. Venkatachalapathy[4], T. M Sridhar[5]

[1]*Department of Chemistry, Rajalakshmi Engineering College, Chennai - 602105, India*
[2]*Department of Chemistry, S.A. Engineering College, Chennai - 600077, India*
[3]*Department of Chemistry, Rajalakshmi Institute of Technology, Chennai - 600124, India*
[4,]*Karpagam Academy of Higher Education, Coimbatore - 641021, India*
[5]*Department of Analytical Chemistry, University of Madras, Chennai - 600085, India*

In the present study, 316L stainless steel (SS) surface was modified with nano yttria stabilized zirconia (YSZ) and nano chitosan by electrophoretic deposition (EPD) and dip coating method. Further, characterizations using XRD, FTIR, FESEM with EDAX confirmed the structural and morphological properties of the coated samples. The corrosion behavior of nano chitosan/YSZ coated 316L SS samples in artificial saliva medium with different concentrations of citric acid and tartaric acid was studied using open circuit potential (OCP) time measurements, Nyquist impedance and cyclic potentiodynamic polarization studies (CPP). The composition and the morphology of nano chitosan/YSZ coated 316L SS samples were analyzed by SEM with EDAX and XRD. The cell viability of nano chitosan/YSZ coated 316L SS and uncoated 316L SS samples was analyzed by the MTT assay method.

Keywords: 316L SS, YSZ, Chitosan, EPD, Dip coating, Electrochemical performance

INTRODUCTION

Recently, dental implants are made of materials such as metals, ceramics, alloys, polymers and composites. Corrosion is a significant issue in the fabrication and selection of metals and alloys for service *in vivo* [1, 2]. Implant loosening and failure may occur due to various corrosion mechanisms in the oral environment [3, 4]. Stainless steel includes a wide range of steel types suitable for corrosion or oxidation resistance applications in different environments [5-7]. In the field of biomaterial industry, stainless steel and ceramics have been successfully used in advanced medical devices and implants [8]. Yttria-stabilized zirconia (YSZ) is an advanced ceramic material that exhibits excellent properties like low thermal conductivity, very high thermal stability, mechanical strength and fracture toughness [9, 10].

YSZ nanomaterials are used in biomedical and orthopaedic applications, mainly for repair and replacement of damaged parts of bones, human skeleton, joints and teeth due to their good biocompatibility, osseointegration, and bio inertness. YSZ are also used as catalysts [11, 12].

Chitosan is a biodegradable biopolymer, N-deacetylated product of chitin. It is highly hydrophobic and insoluble in water [13], but soluble in dilute organic acids such as acetic acid [14]. It possesses a regenerative effect on connective gum tissue and accelerates the formation of osteoblast responsible for bone formation. In addition, it has antimicrobial property that helps to protect the host from infection. Due to this property, it is widely used in dental applications. The chitosan thin film developed on the surface of ceramic-coated metal surfaces leads to the formation of a bio composite layer. This bio composite chitosan layer stops the various ions present in saliva from attacking the coating and on the other hand it accelerates the development of osteoblast responsible for new bone formation. The chitosan coated dental implants possess high biocompatibility [15].

Electrophoretic deposition (EPD) is a fast and cost-effective method to obtain a high-purity layer of desired thickness. This coating technique provides more uniform particle distribution compared to other conventional methods like electro deposition, dip coating, spin coating, plasma spray and ion beam coating. This technique is based on the electrophoresis mechanism in which the charged particles move from the suspension to the metal surface in an electric field yielding a thin uniform deposit on a substrate under various surfaces [16, 17]. The dip coating method is the most reliable method compared to other coating methods as it requires less time and simple low-cost equipment. Coating thickness depends on time and viscosity of the solution and it is optimized by changing the concentration of solution and time [18-20].

The nanocomposite coating embedded in YSZ and chitosan (CS) protects the 316L SS against aggressive ions attacks from the oral environment and chitosan resists bacterial attacks from different foodstuffs [21, 22].

EXPERIMENTAL

Materials

Chitosan (degree of deacetylation 100), nano YSZ (99.99%) (particle size <100 nm) were obtained from Thermo Fisher Scientific. The IPA solvents, acetic acid and artificial saliva substances used were of AR grade.

Substrate preparation

ASTM F-89 standard 316L stainless steel (316L SS) (sized 10×10×2 mm) was used as a working electrode after polishing it mechanically using grit silicon carbide papers followed by gentle wash in dilute HCl and soap solution. Further, the samples were ultrasonically cleaned and oven dried. The dried 316L SS substrates were stored in desiccators prior to the EPD process. The chemical composition of 316L SS and 314 SS is given in Table 1.

Nano YSZ suspension preparation

2% nano YSZ suspension was prepared by mixing of 2g nano YSZ powder in isopropyl alcohol. In order to get an agglomerate-free suspension an ultrasonication process was carried out for about 10 minutes.

Chitosan solution preparation

2 % chitosan solution was prepared by mixing of finely ground 2g of chitosan flakes in 2% glacial acetic acid. The resultant solution was stirred constantly for 10 hours. The obtained homogeneous solution was stored in a cool place [23].

Nano YSZ deposition on metal substrate by EPD process

316L SS (sized 10×10×2 mm) was used as working electrode and a thin plate of 314 SS was used as anode. About 1 cm distance was maintained between the two electrodes. The working electrode was covered on one side with non-conducting Teflon tape and the covered part was immersed in the 2% nano YSZ suspension so that only the uncovered substrate faced in front of the anode can be coated. During the EPD process, the YSZ suspension was gently stirred. Deposition was carried out on a 1 cm^2 surface area with an applied potential of 70V at a constant time of 5 minutes. The obtained nano YSZ coating was gently taken out from bath and dried at room temperature for 5 minutes followed by air sintering at 800°C. The structural and morphological properties of the obtained samples were determined.

Chitosan coating on nano YSZ surface by dip coating

The chitosan solution was freshly prepared and nano YSZ coated 316L SS samples were dipped for 1 to 5 minutes. All the specimens were then gently removed from the chitosan bath. The obtained chitosan-coated samples were dried at room temperature.

Artificial saliva (AS) preparation

AS was prepared according to the literature reported [24]. Briefly, methyl-p-hydroxybenzoate (MPS) (2.00 g), sodium carboxymethyl cellulose (10.00 g), potassium chloride (0.625 g), magnesium chloride hexahydrate (0.059 g), calcium chloride dihydrate (0.166 g), potassium hydrogen phosphate (0.804 g), potassium dihydrogen phosphate (0.326 g) were mixed together in one liter of double distilled water. Finally, the pH of AS was adjusted to 6.75 using KOH solution.

Characterization

The microstructure and uniformity of nano chitosan/YSZ was investigated using FESEM (Carl Zeiss). Bruker model was used to obtain XRD patterns of nano chitosan/YSZ. Electrochemical workstation (Bio Logic SP240) was used to investigate electrochemical impedance. Five samples were analyzed for each OCP, CPP and impedance studies. The cell viability of all samples was analysed by the MTT assay method.

Table 1. Chemical composition of 316L SS and 314 SS

Element	% C	% Cr	% Ni	% Mn	% Mo	% P	% Si	% S	% Fe
316L SS	0.03	17.8	14.2	2.0	2.28	0.025	0.72	0.03	62.915
314L SS	0.26	24.6	21.8	2.0	-	0.045	2.10	0.03	49.165

RESULTS AND DISCUSSION

Micro hardness studies

Figure 1 presents the micro hardness of bare 316L SS and nano bio composite coated on 316L SS. A constant load of 100 g was applied on the specimen to check the micro hardness. The bio composite layer displays a higher hardness value (355 HV) compared to uncoated specimen (157 HV). This analysis confirms that the bio composite layer possesses high mechanical strength and high stability compared to nano YSZ coated and uncoated specimen [25].
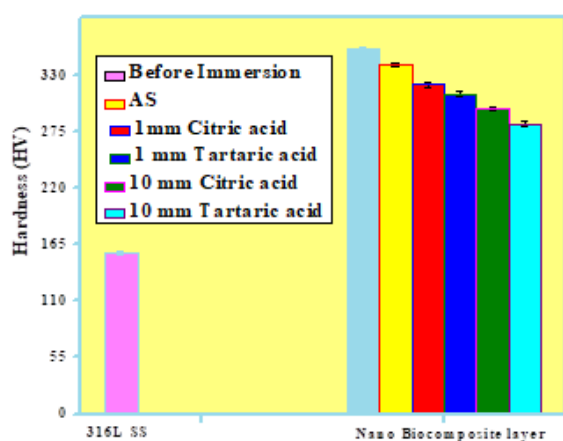

Figure 1. Micro hardness of bare 316L SS and nano biocomposite layer coated on 316L SS before immersion in AS, AS, AS + 1 mm citric acid, AS + 1 mm tartaric acid, AS + 10 mm citric acid and AS + 10 mm tartaric acid, respectively.

X-ray diffraction studies (XRD)

Figure. 2 presents the XRD pattern of the nano biocomposite layer coated on 316L SS before immersion in AS, AS, AS + 1 mm citric acid, AS + 1 mm tartaric acid, AS + 10 mm citric acid and AS + 10 mm tartaric acid. The XRD data confirm the presence of chitosan and nano YSZ and the diffraction patterns matched with JCPDS file No. 82-1246 and 79-0418. The intense peaks appearing at 2θ = 11, 19.8, confirm the crystalline nature of chitosan and those at 30.2, 50.4 and 60.0 confirm the crystalline nature of nano YSZ [26, 27] without any impurities in the coatings.

Fourier transform infrared spectroscopy (FT-IR)

The FTIR spectra of the nano biocomposite layer coated on 316L SS before immersion in AS, AS + 1 mm citric acid, AS + 1 mm tartaric acid, AS + 10 mm citric acid and AS + 10 mm tartaric acid are presented in Figure. 3.
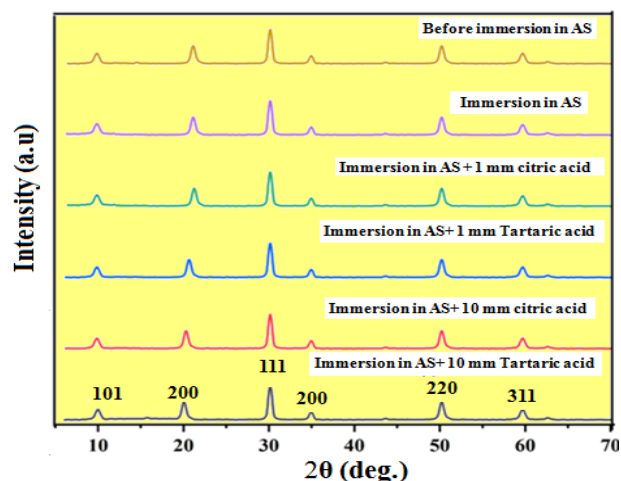

Figure 2. X-ray diffraction of nano biocomposite layer coated on 316L SS in before immersion in AS, AS, AS + 1 mm citric acid, AS + 1 mm tartaric acid, AS + 10 mm citric acid and AS + 10 mm tartaric acid, respectively.
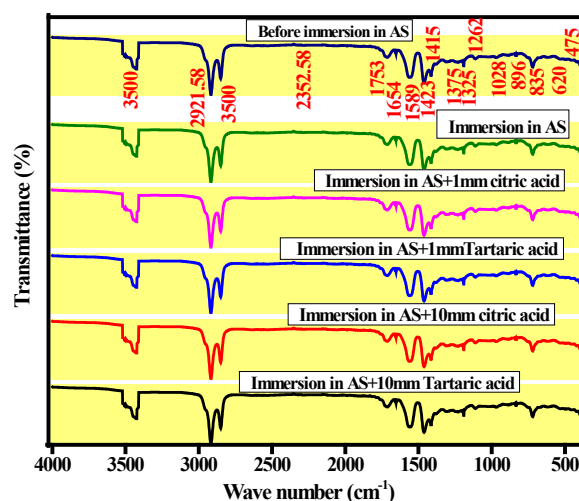

Figure 3. FTIR spectra of nano biocomposite layer coated on 316L SS in before immersion in AS, AS, AS + 1 mm citric acid, AS + 1 mm tartaric acid, AS + 10 mm citric acid and AS + 10 mm tartaric acid, respectively.

Strong and weak FTIR peaks are observed within the range of 3500-1000 cm^{-1}. The peaks at 3500, 2921, 1589 and 1423 cm^{-1} are attributed to the presence of O-H, C-H, N-H, C-O-C and C-N bonds of chitosan, respectively [28, 29]. The peaks at 636 cm^{-1} indicate the presence of nano YSZ along with chitosan.

The nano YSZ coating was made by an EPD process and chitosan was coated on nano YSZ surface by dip coating. The uniformity and crack-free nature of the nano chitosan /YSZ bio composite coating was observed using optical microscope and FESEM. The observed results for optical microscopic image and FESEM image of nano chitosan /YSZ are depicted in Figure 4.
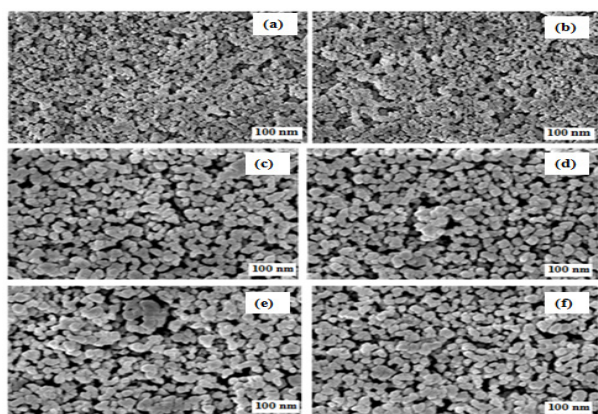
Figure 4. FESEM images of the nano biocomposite layer coated on 316L SS before immersion in AS, AS, AS + 1 mm citric acid, AS + 1 mm tartaric acid, AS + 10 mm citric acid and AS + 10 mm tartaric acid, respectively.

These images confirm the uniform, crack-free nature of nano chitosan/YSZ. This study further confirms that the nano biocomposite coatings are composed of 40 -80 nm grain sized YSZ and 80-200 nm grain sized chitosan.

EDAX analysis was helpful to identify the elemental composition of nano chitosan /YSZ. The presence of C, O, Y, Zr and N in chitosan and nano YSZ without any impurity is shown in Figure. 5.
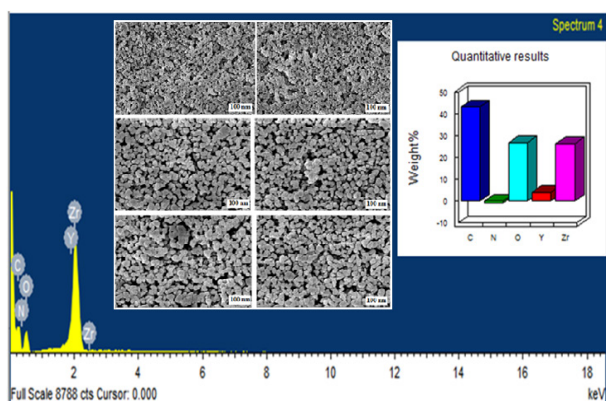

Figure 5. EDAX spectrum of nano bio composite coated on 316L SS

This study further confirms the absence of oxidized products of the base metal (iron oxide) during the sintering process and also the lack of decomposition of chitosan and nano YSZ during EPD and dip coating process.

Electrochemical studies

Open circuit potential (OCP). The OCP time measurement results [30] of nano biocomposite layers with various concentrations of (a) AS + 1 mm citric acid (b) AS + 1 mm tartaric acid (c) AS + 10 mm citric acid (d) AS + 10 mm tartaric acid and uncoated 316L SS are presented in Figure. 6. The OCP studies of all samples were carried out at

different concentrations for about 1 hour. A nobler shift was observed for nano biocomposite coated samples in all media when compared to the uncoated 316L SS sample indicating the better corrosion resistance of the nano biocomposite layer. On adding different concentrations of citric acid and tartaric acid to AS the OCP values slightly decreased due to biofilm-acid interaction.
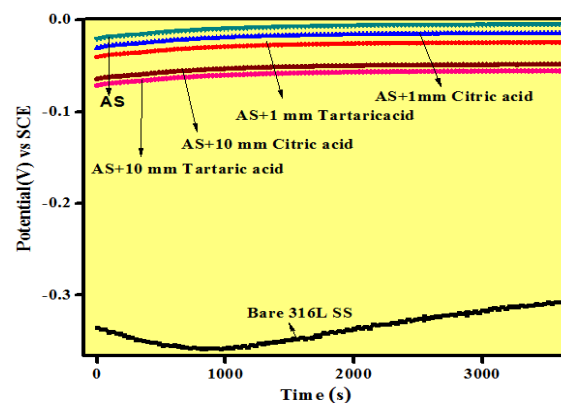

Figure 6. Open circuit potential time measurement for uncoated and nano biocomposite layer coated on 316L SS in (a) AS + 1 mm citric acid (b) AS + 1 mm tartaric acid (c) AS + 10 mm citric acid (d) AS + 10 mm tartaric acid, respectively.

Electrochemical impedance studies (EIS). EIS studies were carried out for all specimens under OCP conditions after immersion in various concentrations of AS + 1 mm citric acid, AS + 1 mm tartaric acid, AS+10 mm citric acid, AS+10 mm tartaric acid and uncoated 316L SS in the frequency range from 10 kHz to 10 mHz. EIS and the corresponding equivalent circuit results are presented in Figure 7.
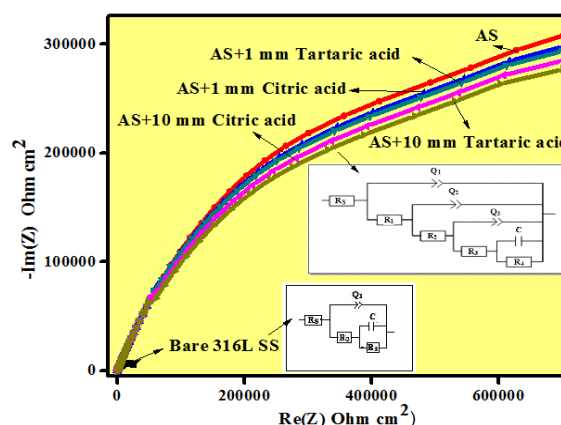

Figure 7. Nyquist plot obtained for uncoated and nano biocomposite layer coated on 316L SS in AS, AS + 1 mm citric acid, AS + 1 mm tartaric acid, AS + 10 mm citric acid and AS + 10 mm tartaric acid, respectively.

Nano biocomposite layer coated 316L SS for about 3 minutes possesses maximum impedance (30 $M\Omega$ cm^{-2}) compared to other coated samples and uncoated 316L SS.

The electrochemical parameters were obtained by Z Sim curve fitting analysis where, Rs is solution resistance, R_1 and Q_1 corresponding polarization resistance and constant phase element (CPE) of nano YSZ coated layer. R_2 and Q_2 represent corresponding polarization resistance and CPE of passivation layer on metal surface, R_3 and C correspond to resistance and capacitance of metal surface. In Figure 7 Rs represents solution resistance, R_1 and Q_1 correspond to polarization resistance and CPE of chitosan layer. R_2 and Q_2 represent corresponding polarization resistance and CPE of nano YSZ layer. R_3 and Q_3 depict polarization resistance and CPE of passivation layer, R_4 and C represent polarization resistance and capacitance of passivation layer. The obtained results are presented in Table 1.

The chitosan barrier resistance (R_{b1}) and passivation resistances (Rp) of biocomposite layer coated for about 3 minutes was maximum compared to uncoated 316L SS. The charge transfer resistance of the uncoated specimen was much less than that of nano biocomposite layer and uncoated metal. This indicates that nano biocomposite layer possesses higher resistivity toward aggressive ions attack from AS medium and it does not allow electron transfer from the metal surface to the bulk of AS medium.

Bode impedance and Bode phase plots of biocomposite layer in AS, AS + 1 mm citric acid, AS + 1 mm tartaric acid, AS + 10 mm citric acid, AS + 10 mm tartaric acid and uncoated 316L SS are given in Figure 8 (a, b). Maximum impedance values are observed for biocomposite layer coatings for about 3 minutes when compared to uncoated 316L SS specimens.

Table 1. Z fit values of nano biocomposite coated samples in AS medium along with citric and tartaric acid and comparison with uncoated 316L SS

| Acid concentration	|Z| Ω cm^2	R_S Ωcm^2	Q_{coat} (F cm^{-2}s^n)	n_{coat}	R1 (chitosan layer)	R2 YSZ coat	Q_b (F cm^{-2}s^n)	n_b	R3 Ω cm^2	C_{dl} F cm^2	R4 Ωcm^2
Uncoated 316L SS	5644	388	----	0.81	----	----	----	----	190	3.933×10^{-5}	534.5
AS	308078	20.5	8.19×10^{-11}	0.28	5.48×10^6	2.06×10^6	7.51×10^{-10}	0.22	1.20×10^6	9.52×10^{-11}	184484
AS+1mm citric acid	295578	27.8	6.59×10^{-11}	0.30	5.76×10^6	1.64×10^6	6.89×10^{-10}	0.24	0.98×10^6	8.92×10^{-11}	164504
AS+1mm tartaric acid	299078	24.5	7.49×10^{-11}	0.32	5.88×10^6	1.86×10^6	7.01×10^{-10}	0.26	1.01×10^6	9.04×10^{-11}	168424
AS+10mm citric acid	293578	30.8	5.96×10^{-11}	0.33	5.24×10^6	1.48×10^6	6.64×10^{-10}	0.29	0.86×10^6	8.42×10^{-11}	158400
AS+10mm tartaric acid	291278	32.9	5.43×10^{-11}	0.35	5.08×10^6	1.24×10^6	6.21×10^{-10}	0.31	0.78×10^6	8.34×10^{-11}	152444
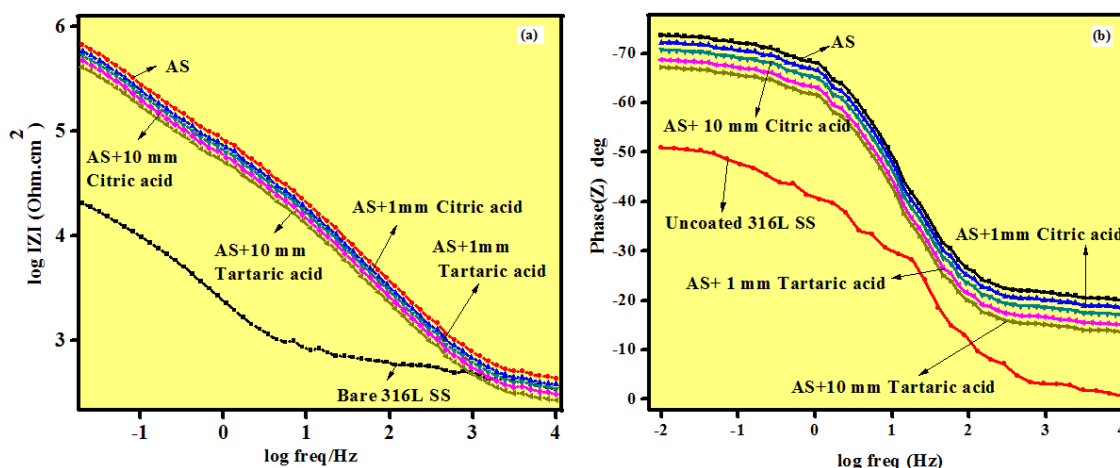
Figure 8. (a) Bode impedance (b) Bode phase plots obtained for uncoated and nano biocomposite layer coated on 316L SS in AS, AS + 1 mm citric acid, AS + 1 mm tartaric acid, AS + 10 mm citric acid and AS + 10 mm tartaric acid, respectively.

The shape of the phase angle *vs.* frequency relationship indicates the capacitive behavior of the coatings. The phase angle of the biocomposite layer displays a significant shift to −70° and this result confirms that the biocomposite layer exhibits a highly capacitive behavior compared to all other specimens. It was also observed that the corrosion resistivity of the biocomposite layer was significantly higher than that of uncoated 316L SS samples [31, 32].

Cyclic potentiodynamic polarization

The cyclic potentiodynamic polarization studies were carried out for all specimens with various concentrations of AS, AS+ 1 mm citric acid, AS + 1 mm tartaric acid, AS + 10 mm citric acid, AS + 10 mm tartaric acid and uncoated 316L SS and the obtained results are presented in Figure. 9.
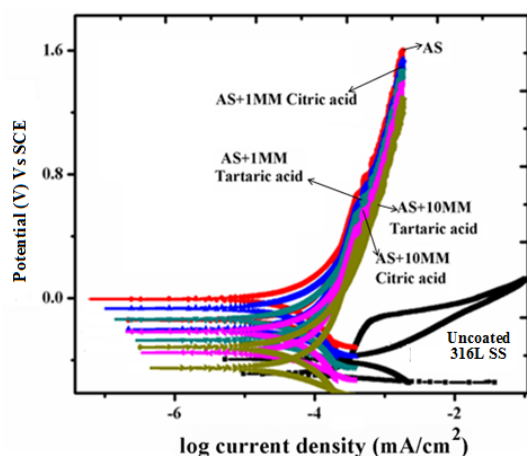

Figure 9. Cyclic potentiodynamic polarisation curves obtained for uncoated and nano biocomposite layer coated on 316L SS in AS, AS + 1 mm citric acid, AS + 1 mm tartaric acid, AS + 10 mm citric acid and AS + 10 mm tartaric acid, respectively.

The parameters obtained from the polarization curve are corrosion potential (Ecorr) and corrosion current density (Icorr). The Ecorr and Icorr values were determined by Tafel slope extrapolation, and the passive current density was obtained from the passive zone where the corrosion current remained approximately constant. The corrosion potential (E_{corr}) and corrosion current density (I_{corr}) values are given in Table 2. The nano biocomposite layer coated for 3 minutes possesses a higher corrosion potential E_{corr} -172.569 mV and a lower corrosion current density I_{corr}0.001μA value among all specimens. The E_{corr} values are shifted in less negative direction from uncoated sample to chitosan coated sample. This is due to the stable nature of the nano biocomposite layer toward aggressive ions attacks from the AS medium and this layer stops the release of ions from substrate to solution. Corrosion

18

rate can be calculated by using ASTM-G 102-89 standard equation:

$$\text{Corrosion rate(CR)} = \frac{K1 \times I_{corr}}{\rho} \times EW \text{ mm/year}$$

where, CR is corrosion rate, EW is equivalent weight of the metal, ρ is density, $K1 = 3.27 \times 10^{-3}$, Icorr is corrosion current. These results indicate that nano biocomposite layers on the metal surface are more stable and possess better barrier property compared to uncoated 316L SS.

Table 2. Tafel fit values of nano biocomposite coated samples in AS medium along with citric and tartaric acid and comparison with uncoated 316L SS.

AS and acid concentration	$E_{corr\,(mV)}$ *vs* SCE	I_{corr} μAcm^{-2}
316L SS	-425	2.308
AS	-088	0.001
AS+1 mm citric acid	-105	0.003
AS+1 mm tartaric acid	-107	0.002
AS+10 mm citric acid	-110	0.004
AS+10 mm tartaric acid	-115	0.005

Biocompatibility studies

The cytotoxicity studies of uncoated 316L SS, nano biocomposite coated 316L SS samples immersed in AS, AS+1 mm citric acid, 1 mm tartaric acid, 10 mm citric acid and 10 mm tartaric acid are shown in Figures 10 and 11, respectively. These studies were carried out using human MG-63 osteoblast cell line by MTT assay method [28]. Most of the human MG-63 osteoblast cell line were viable on nano chitosan /YSZ coated 316L SS rather than nano YSZ and 316L SS samples. Hence, the cell viability of nano chitosan /YSZ coated sample was found to be highly uniform and non-porous coating on the metal surface [33].
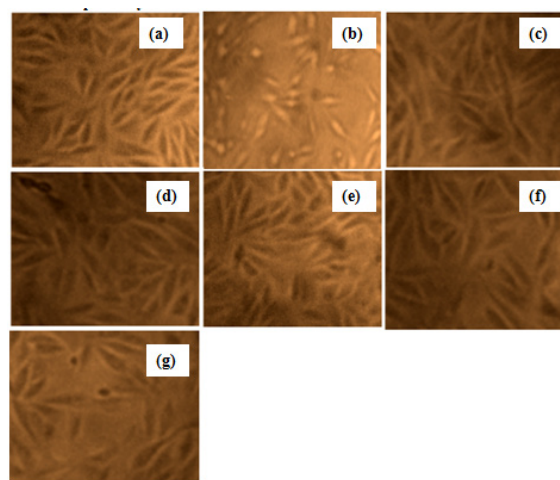

Figure 10. (a),(b),(c),(d).(e),(f) and (g) Microscopic images of Cell for control cell line, uncoated, nano bio composite coated sample immersed in AS, AS+1 mm citric acid,1 mm tartaric acid, 10 mm citric acid and 10 mm tartaric acid.
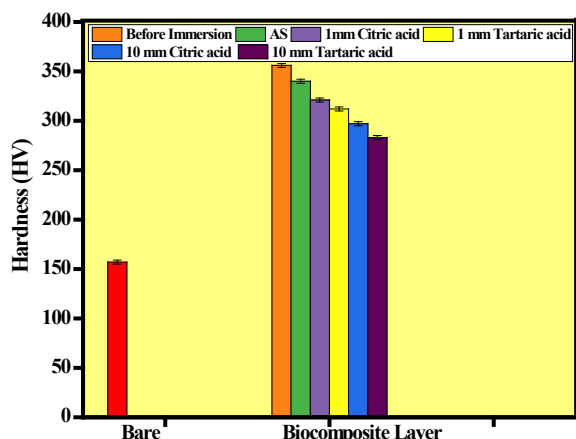
Figure 11. MTT assay results obtained for bare 316L SS compared with nano bio composite coated sample immersed in AS, AS+1 mm citric acid, 1 mm tartaric acid, 10 mm citric acid and 10 mm tartaric acid.
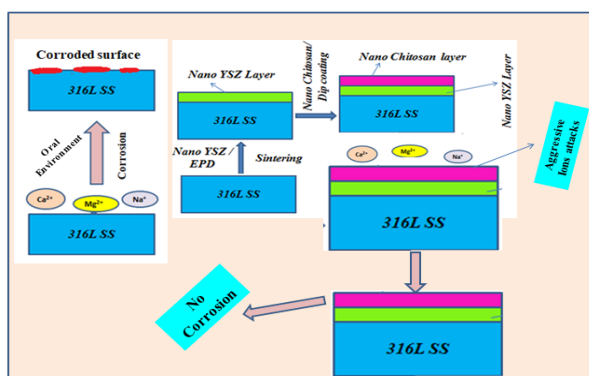
DISCUSSION

Figure 12. Schematic representation of the corrosion mechanism on the surface of bare 316L SS and biocomposite coated 316L SS.

Figure 12 is a schematic representation of the corrosion mechanism on the surface of bare 316L SS and biocomposite coated 316L SS and this paper deliberates the development of nano biocomposite coating by means of nano YSZ and nano chitosan along with determination of its surface morphology and electrochemical properties. Dip coating process was utilized to develop chitosan coatings on air sintered nano-YSZ coated 316L SS samples. The coated samples were characterized using XRD, FTIR, FESEM and EDAX in order to evaluate their structural, functional and morphological properties. Further, the optimized samples were subjected to electrochemical studies in artificial saliva medium in the presence of various concentrations of citric acid and tartaric acid which was not reported earlier by any researchers using this bio composite. In our previous research work nano YSZ alone was coated on the surface of 316L SS but in the present work a nano biocomposite is coated on the surface of 316L SS. The hardness, electrochemical characteristics

OCP, CPP and electrochemical impedance studies confirmed that the biocomposite coated 316L SS samples possess very good corrosion resistance in artificial saliva medium. The OCP value moves in nobler direction when compared with nano YSZ coatings. The Nyqust value and Bode impedance value also confirm the above statement. The Ecorr and Icorr values also confirm that the biocomposite coated samples possess better corrosion resistivity than nano YSZ coated samples. The obtained results for the optimized sample using citric and tartaric acid depict a better electrochemical performance compared to uncoated 316L SS in artificial saliva medium.

CONCLUSIONS

Nano YSZ coating on 316L SS was obtained by electrophoretic deposition and chitosan film was formed on the nano YSZ by dip coating. FESEM studies confirmed that YSZ particles deposited on 316L SS were in the nano scale range (40-80 nm) roughly spherical; chitosan size was in the 80-200 nm range. Electrochemical studies of the bio nanocomposite revealed its higher corrosion resistance compared to nano YSZ/316L SS and bare metal substrate. OCP studies indicated that the bio nanocomposite coated samples shifted in nobler direction indicating that the bio nanocomposite film exhibited better polarization resistance and lower capacitance values as observed from EIS studies. Electrochemical studies revealed that the nano biocomposite layer could act as an effective barrier against corrosive ions attack and resist ions intercalation from artificial saliva of various composition. Chitosan is water-insoluble and possesses very good hydrophobicity. It hardly reacts with citric acid and tartaric acid in the oral environment at room temperature. As foodstuffs contain very little amounts of acids and the acids only contact with implants in few seconds, therefore this type of acids not readily attack the dental implants. The composite coatings enhanced the durability and stability of the base metal. Finally, the developed bio nanocomposite coated sample would be an ideal choice for dental implant applications.

REFERENCES

1. N. Eliaz, *J. Mech. Behav. Biomed. Mater.*, **12,** 234 (2008).

2. G. Manivasagam, D. Dhinasekaran, A. Rajamanickam, *Recent Patents Corros. Sci.,* **2**, 40 (2010).
3. T. V. Thamaraiselvi, S. Rajeswari, *Trends Biomater. Artif. Organs,* **18,** 9 (2004).
4. C.Viazzi, J. P. Bonino, F. Ansart, *Surf. Coat. Technol.*, **20**, 3889 (2006).
5. N. K. Sahoo, S. C. Anand, J. R. Bhardwaj, P. Sachdeva, B. L. Sapru, *Med. J. Armed Forces India*, **50** (1), 10 (1994).
6. R. N. Brown, B. E. Sexton, M. G. Chu, T. R. Katona, K. T. Stewart, H. M. Kyung, S. S. Liu, *Am. J. Orthod.* **145**(4), 496 (2014).
7. P. M. Hashemi, E. Borhani, M. S. Nourbakhsh, *Nanomed. J.,* **3**(4), 202 (2016).
8. M. Holzapfel, *Drug Delivery Rev.*, **65**, 581 (2013).
9. J. R. Kelly, I. Denry, *Dent. Mater.*, **24**, 289 (2008).
10. X. Y. Gu, X. Li, Q. Liu, Y.X. Chen, Y. Li, *Mater. Eng.*, **38**, 1044 (2009).
11. C. Viazzi, J. P.Bonino, F. Ansart, Surf. Coat. Technol. 201, 3889, (2006). **Same as ref. 4**
12. T. V.Thamaraiselvi, S. Rajeswari, *Trends Biomater. Artif. Organs,* **18**, 9 (2004).
13. D. E. Ali-Komi, M. R. Hamblin, *Int. J. Adv. Res.,* **4**(3), 411 (2016).
14. Q. Y. Deng, Ch. R. Zhou, B. H. Luo, *Pharmaceutical Biology*, **44**(5), 336 (2006).
15. Sh. H. Hsu, H. J. Tseng, T. L. Tsou, H. J. Wang, *Journal of Tissue Engineering and Regenerative Medicine*, **7**(1), 20 (2013).
16. L. Besra, M. Liu, *Prog. Mater. Sci.*, **52**, 1 (2007).
17. M. Boehmer, *Langmuir,* **12**, 5747 (1996).
18. M. Nakashima, T. Ebine, M. Shishikura, K. Hoshino, K. Kawai, K. Hatsusaka, *Mater. Interfaces*, **2**(5), 1471 (2010).
19. M. Deepa, T. K.Saxena, D. P. Singh, K. N. Sood, S. A. Agnihotry, *Electrochim Acta,* **51**,1974 (2006).
20. S. Patil, U. Hoshing, D. Rachalwar, *Journal of Current Research,* **9**(11), 61490 (2017).
21. S. Singh, G. Singh, K. Aggarwal, *International Journal of Biological Macromolecules,* **151**, 519 (2020).
22. S. Singh, G. Singh, N. Bala, *Materials Chemistry and Physics,* **237**,121884 (2019).
23. A. Domard, M. Rinaudo, *International Journal of Biological Macromolecules,* **5**(1), 49 (1983).
24. S. Patil, U. Hoshing, D. Rachalwar, *Journal of Current Research*, **9** (11), 61490 (2017).
25. V. M. Matyunin, A. Yu. Marchenkov, A. N. Demidov, *Materials Science and Engineering Metals Tech.*, **6**, 53 (2013).
26. M. N. Tsampas, F. M. Sapountzi, P. Vernoux, *Catalysis Science & Technology,* **5**(11), 4884 (2015).
27. J. A. M. Oliveira, R. A. C. De Santana, A. D. O. W. Wanderley, *Neto Progress in Organic Coatings.* **143**,105631, (2020).
28. T. Lertwattanaseri, N. Ichikawa, T. Mizoguchi, Y. Tanaka, S. Chirachanchai, *Carbohydrate Research,* **344**(3), 331 (2009).
29. K. Alagarsamy, V. Vishwakarma, G. S. Kaliaraj, N. C. Vasantha, S. J. R. Samuel, *Journal of Adhesion Science and Technology*. **34**(4), 349 (2020).
30. Ch. Chen, J. Zuo, Y. Wang, *Int. J. Electrochem. Sci.*, **15**, 4944 (2020).
31. J. M. Bastidas, J. L. Polo, C. L. Torres, E. Cano, *Corrosion Science,* **43**(2), 269 (2001).
32. D. Predo, S. L. Iconar, M. V. Predoi, *Coatings,* **10**(905), 1 (2020).
33. W. Jun, Ch. Peng, J. Wen, G. Mingzhi, *Biomedical Research,* **289**(10), 1 (2017).

Chemometric assessment of agricultural samples from the vicinity of a lead-zinc smelter

M. G. Karadjov

Geological Institute, Bulgarian Academy of Sciences, 1113 Sofia, Acad. G. Bonchev Str. BL 24, Bulgaria

In the present article the pervasion of toxic elements (As, Cd, Pb, Zn) in edible and forage parts of plants grown in the fields near a Pb-Zn smelter was studied in order to propose efficient measures to minimize adverse effects on human health and ecosystems in the region. Statistical treatment of results based on hierarchical cluster analysis (HCA) and non-hierarchical clustering algorithm (K-means) showed that soil and air contamination by toxic chemical elements is the major environmental problem especially near to a Zn-Pb smelter (Plovdiv, Bulgaria). Subject of the present paper are the amounts of 4 toxic elements in different parts (21) of plants collected in the above-mentioned area, which were introduced in the formed matrix for data classification and interpretation. The result of the chemometric examination accentuates on Cd pollution, especially the inadmissible Cd content in carrots planted on the fields about 5-7 km from the factory.

Keywords: Zn-Pb factory, toxic elements, uptake from agro products, chemometrics

INTRODUCTION

In the 60ies, a lead-zinc metallurgical complex and a plant for pesticides production near the smelter were built in the vicinity of Plovdiv city. The construction of these plants in the fertile fields of the Upper Thracian Plain, near the second-largest Bulgarian city, is an example of poor management decision causing constant eco-problems for the district. After the political changes in Eastern Europe at the end of the 80ies a series of studies have been carried out to assess the real level of anthropogenic pollution and to propose new measures for limitation of the waste emissions from both factories. Chemical pollution of the region, concomitant effect of Pb-Zn emissions and pesticides production is a subject of 2 important international projects [1, 2], as well as a subject of national monitoring (at the beginning of the 21th century automatic analytical stations have been installed to control emissions of pollutants). Most of the investigations performed in the region are devoted to the assessment of concentrations of toxic elements and their distributions in the environmental compartments – water, soil and air. The investigations confirmed that Pb, Cd, As and Zn are major toxicants and elevated contaminant concentrations are registered not only near the industrial facilities but pollution spreads and affects a larger region depending on the climatic conditions, geographical locations and local mineralogy.

The degree of biouptake of toxic elements in fruits and vegetables from the region has been the purpose of several comparative studies. The results of the analyses of some agricultural products obtained under the project WATMETAPOL [1] are slightly more favorable compared to the data from the previous international scientific project [2] in the Plovdiv area. Compared to other published data [3, 5, 6] for the vicinity of Pb-Zn factories the current results are almost identical.

Plants analysis would serve as an indirect approach to assess pollution of the region as far as the biouptake of contaminants in the plant species is from one side *via* roots or from the other side by direct atmospheric deposition onto the plant surfaces. In addition, biouptake depends on factors such as plant physiology, soil properties, climate and fertilization. It is worth mentioning that determination of toxic elements content in agro production would provide information to local administration concerning: (i) eco control on emitting factories; (ii) delineation of zones in risk for agriculture and recommendation for vegetables suitable to be grown in the region without adverse effect on animal and human health.

The major goal of the present study is the chemometric evaluation of similarities (or dissimilarities) of the quantities of toxic elements found in the samples (edible parts of vegetables and fodder grown in the region). This will allow clarification of the boundaries of the zones in risk, distribution and degree of pollution.

---

* To whom all correspondence should be sent:
E-mail: metodi@geology.bas.bg

EXPERIMENTAL

Sampling and Analysis

Plants have been collected from different points in the risk zone, taking into account data for pollution spreading obtained in the frame of WATMETAPOL project and factors such as wind rose and soil composition. Plant samples were collected directly from the field, at the end of October, in this way ensuring longest possible aerosol exposure (Map 1).
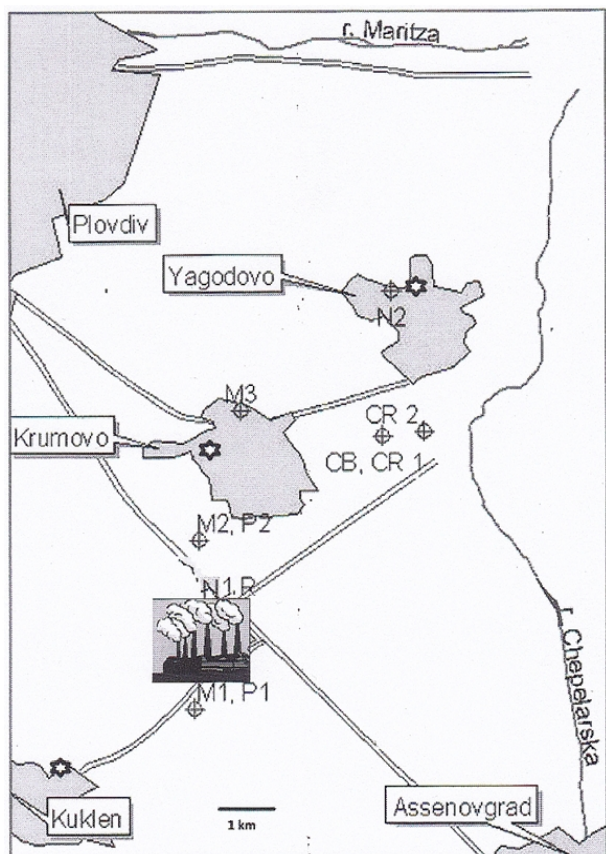
Map 1. Test agricultural production from the region. The sampling points are marked as: M – maize (*Zea mays*); N – nuts (*Juglans regia*); P – peppers (*Capsicum spp.*); CR- carrots (*Daucus carota sativa*); CB – cabbage (*Brassica oleracea capitata*);

Collected plants were carefully washed and their edible and nonedible parts were separated. All parts were dried up at room temperature to constant weight (BDS EN 13804 [7]) and grinded. A total of 21 analytical samples were formed from leaves, stems, kernels and seeds [4].

About 0.5 g of dried sample, precisely weighed, was decomposed with nitric acid according to BDS EN 13805 [8]. Toxic elements were measured using ICP-OES and ETAAS under optimal instrumental parameters taking into account BDS EN 14082 [9] and our own experience [10]. The resulting toxic element concentrations are summarized in Table 1.

RESULTS

The inspection of the analytical results led to several conclusions:

1. Lead, zinc and cadmium oxides or carbonates from aerosol are retained on the surface of the leaves of the plants and further absorbed;

2. Difference in the concentrations between the leaves and veins (stalks) show that As biouptake is mostly from the soil;

3. Concentrations of toxic elements in corn leaves decrease 3-10 times between the outer and inner leaves;

4. Concentrations of Pb, Zn and As in walnut and maize grains are within acceptable limits, only cadmium slightly exceeding the permissible limits (Ordinance No 31 [11]).

Chemometrics

The statistical classification of the analytical results was undertaken with the idea to master the IBM's SPSS "Statistics" software package. The data set (matrix of 21 samples × 4 elements) was subjected to statistical cluster analysis (hierarchical and non-hierarchical mode). The raw data set was standardized by the use of a z-transform procedure in order to avoid differences in dimensions of the variables and to normalize the data. The hierarchical clustering was performed using squared Euclidean distances as similarity measure, Ward's method of linkage and Sneath's criterion for cluster significance. K-means method was used as non-hierarchical clustering approach. Both methods are well known and documented with detailed description [12].

The goal of the multivariate interpretation was to associate the variables (elements) or the cases (samples) in clusters according to the similarities on different steps of study. Further, it was of substantial interest to detect discriminating features for each of the identified clusters in order to better understand the reasons of clustering (classification). The first step of the intelligent data analysis was to detect specific relationships between the samples (patterns of similarity) which could be attributed to the content of the toxic elements and hierarchical cluster analysis was used for this procedure of grouping.

As can be seen from Fig. 1, the behavior of the pollutant As differs substantially from that of the other three metals studied. As it is evident that Pb and Zn content is due to industrial emitters, the biouptake of As probably depends on different sources (soil composition) or different biouptake mechanisms.

Table 1. Element contents [ppm] in the studied agricultural samples

| No	Sample	Label	Pb	Cd	Zn	As
1	Walnuts, edible parts 1	N1	0.04	0.14	46.8	0.008
2	Walnut green husks	N1h	121.3	2.5	304.3	0.117
3	Walnuts, edible parts 2	N2	0.03	0.12	25.9	0.021
4	Cabbage leaves	Cb	11.7	<0.002	23.7	0.79
5	Carrots 1	C1	0.32	0.83	8.6	0.026
6	Carrot leaves 1	C1l	20.4	5.56	88.5	0.66
7	Carrots 2	C2	0.15	0.7	23.2	0.012
8	Carrots leaves 2	C2l	15.8	0.9	35.8	0.73
9	Peppers, edible parts 1	P1	11.6	1.53	35.4	0.148
10	Pepper leaves 1	P1l	128.1	5.05	500	2.43
11	Peppers, edible parts 2	P2	2.1	0.87	23.9	0.169
12	Pepper seeds 2	P2s	0.04	0.65	24.3	0.201
13	Pepper leaves 2	P2l	77.8	4.42	303	0.97
14	Veins from pepper leaves 2	P2v	59.3	3.12	232	0.03
15	Maize kernels 1	1M	0.02	0.17	31.2	0.015
16	Corn stalks 1	M1	0.16	0.44	25.5	0.286
17	Corn silks 1	M1s	0.48	0.39	93.7	1.77
18	Husk leaves – inside 2	M2i	14.2	0.46	28.9	0.6
19	Husk leaves – outside 2	M2o	56.9	2.8	314	0.51
20	Husk leaves – outside, washed 2	M2w	0.08	0.01	5.9	<0.002
21	Corn stalks 3	M3	19.3	1.14	87.9	0.85
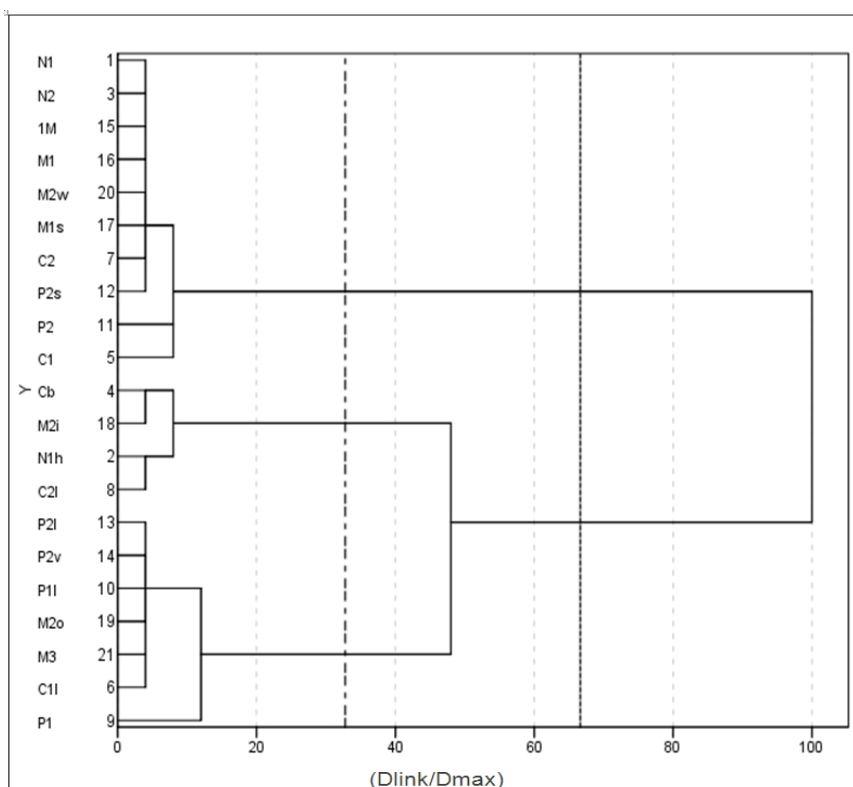
Figure 2. Hierarchical clustering of the 21 samples.

Table 2. Members of the 3 different clusters and distance from respective cluster center

Sample	No	Label	Distance
Members of Cluster No 1 (in21z) and distances from respective cluster center. Cluster contains 4 cases.			
Walnut green husks	2	N1h	.096
Cabbage leaves	4	Cb	.079
Carrots leaves 2	8	C2l	.039
Husk leaves – inside 2	18	M2i	.062
Members of Cluster No 2 (in21z) and distances from respective cluster center. Cluster contains 7 cases.			
Carrot leaves 1	6	C1l	.083
Peppers, edible parts 1	9	P1	.141
Pepper leaves 1	10	P1l	.034
Pepper leaves 2	13	P2l	.028
Veins from pepper leaves 2	14	P2v	.028
Husk leaves – outside 2	19	M2o	.109
Corn stalks 3	21	M3	.052
Members of Cluster No 3 (in21z) and distances from respective cluster center. Cluster contains 10 cases.			
Walnuts, edible parts 1	1	N1	.022
Walnuts, edible parts 2	3	N2	.021
Carrots 1	5	C1	.115
Carrots 2	7	C2	.025
Peppers, edible parts 2	11	P2	.110
Pepper seeds 2	12	P2s	.030
Maize kernels 1	15	1M	.020
Corn stalks 1	16	M1	.024
Corn silks 1	17	M1s	.049
Husk leaves – outside, washed 2	20	M2w	.029

Results for Cd undoubtedly showed that Cd pollution is due to natural presence of Cd together with main elements and confirming same industrial source of pollution.

The hierarchical clustering of the 21 different plant part samples is presented in Fig. 2. Three clusters are observed, after dividing by 33 and 66% statistical certainty. The smallest cluster includes 4 intermediately polluted samples. The second cluster contains 7 samples with the highest levels of pollutants. The biggest cluster 3 combines 10 samples – edible parts and inside leaves, relatively clean according to the analytical results.

Keeping in mind these results, non-hierarchical clustering was additionally performed. The K-means grouping of the into 3 clusters resembles almost the same clustering as already obtained by hierarchical clustering. In Table 2 the members of each supervised cluster and distances are indicated. The

next figures 3 and 4 display the distribution of elements and samples according to the K-means clustering.

DISCUSSION

In general, the results of the hierarchical clustering confirm the obvious conclusions based on the results from chemical analysis. The observation on the separation of the variables (elements) (Figs. 1 and 3) marks the specific behavior of As and confirms previous findings that agricultural products absorb toxic metals from the air, but the source of the metalloid is contaminated soil. The positions of Cd (Figs. 1 and 3) do not clearly indicate how the pollutant accumulates in agricultural products. The concentrations of cadmium follow the Zn and Pb contents in the air and reflect their contents in the various industrial concentrates or ore sources supplied to the smelter. Discrimination of cases

(samples) presented on Figs. 2 and 4 confirmed the conclusion that the leaves, owing to their large surface, additionally adsorb dust and atmospheric deposits, in this way accumulating higher levels of toxic elements. As seen, the inner parts of agricultural products such as corns and nuts are much more protected from pollution. It might be generally concluded that aerosol deposition of pollutants dominates over their biouptake from the soil.
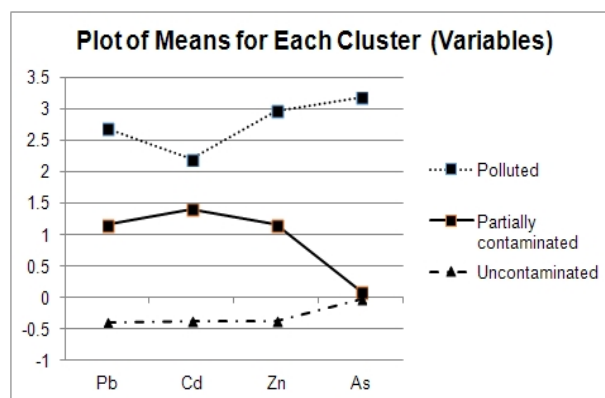
Figure 3. Averages for the 4 elements in each of the identified non-hierarchical clusters.
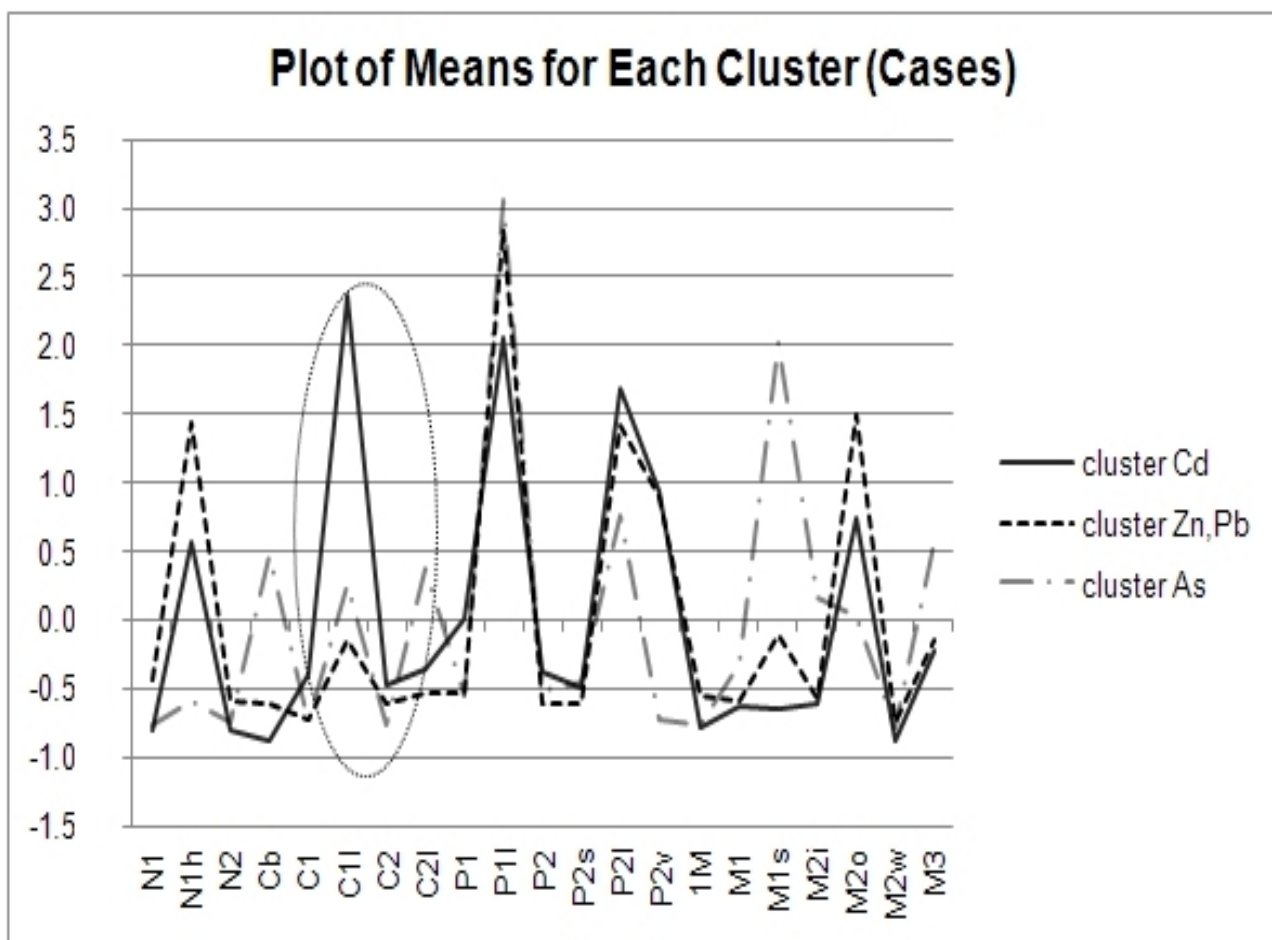
Figure 4. Averages for the 21 samples for each identified cluster.

The chemometric procedures mark new information to the peculiarities of Cd accumulation in agricultural products. The mean value for Cd in Fig. 3 marks a big Max for the moderately contaminated samples, insignificant Max for the relatively clean samples and a Min for the highly contaminated samples. This explains the neglect of Cd in a previous research with the participation of the present author [4] and its polluting impact. Carrot leaves C2l fall into the cluster of moderately contaminated samples (see Fig. 2) while C1l carrot leaves are among the most polluted, although the distance between the sampling points (map 1) is not large. This is even more clearly seen in Fig. 4 (the positions surrounded by an ellipse), with the C1l peak being the highest in the Cd series. Evidently, the high Cd content in the carrot leaves is not proportionally transferred to the edible parts of carrots.

Verma *et al.* [16] modeled the accumulation of cadmium in the vegetables (carrots, spinach, radishes and cabbage) and showed that the uptake rate was highest for the carrots, 1.5 times smaller for spinach and 2 times smaller for cabbage and radishes. Another conclusion from this modeling is that saturation with Cd in vegetables occurs for spinach and radishes after 40 days of planting, for cabbage after 65 days, and for carrots after 100 days. It follows that carrots are the most affected by cadmium contamination.

An overview of the analysis data in this study shows that such saturation occurs in the studied carrots, but at values exceeding about 8 times MPL [11] in edible parts of plants. The observed excess of 1.5 times in the edible parts of walnuts and corn might be estimated as an analytical error. (the presence of toxic elements in the edible parts of peppers is not representative because they were rimed).

The inadmissible Cd pollution in the carrots accentuated from the multivariate interpretation is described by several researchers from different countries [13-15]. Biological investigations consider this phenomenon as a critical problem, because it shows a direct transport of Cd from the carrots to the human through food chain [17, 18].

The latter sentence is an addition to a brochure, issued in 2013 by the Center for Risk Assessment – Bulgarian Agency for Food Safety [19] for Cd as a serious environmental pollutant. The current chemometric examination leads to the conclusion that cadmium is the most dangerous pollutant in the studied area and the practical recommendation to the agro producers could be: The carrot seedlings must be at least 10 km least distant from the Cd source.

CONCLUSION

In general, the chemometric analysis of the chemical results makes it possible to correctly assess the pollution risk with toxic elements, the mobility of the pollutants and the quality of life in an industrially impacted region. It is obvious that chemometric interpretation even for a small data set updates government documents and argues true instructions to local agro producers.

REFERENCES

1. NATO Science for Peace Program Project SiP 973739 WATMETAPOL (2001-2004) http://www.brgm.fr/sites/default/brgm/publications/georama_13/index.html#2.

2. P. Bojinova, L. Stanislavova, in: Untersuchungs-methoden, Bewertungsmasstabe und staatliche Regelungen für den Bodenschutz (Symposium mit Osteuropäischen Staaten, Schmalenberg, Deutchland, 1-4 Dezember, 1993), p. 115.

3. D. Voutsa, A. Grimanis, C. Samara, *Environ. Pollut.*, **94 (**3), 325 (1996). https://doi.org/10.1016/S0269-7491(96)00088-7.

4. E. N. Pentcheva, N. Velitchkova, M. Karadjov, in: SGEM Sci. Papers (Proc. 3rd Int. Sci. Conf. - SGEM2003, Albena, Bulgaria, June 9-13, 2003), p. 295. https://sgemworld.at/sgemlib/spip.php?article1717

5. C. Samara, P. Misaelides, D. Tsalev, I. Anousis, Th. Kouimtzis, *Fresenius Environ. Bull.*, **1,** 577 (1992).

6. Z. Pančevski, T. Stafilov, K. Bačeva, *IUPAC © Glob. Res. Publ.*, **9 (**1-2), 17 (2014). http://www.serialsjournals.com/serialjournalmanager/pdf/1466064067.pdf

7. BDS EN 13804:2013 Foodstuffs.

8. BDS EN 13805:2015 Foodstuffs.

9. BDS EN 14082:2003 Foodstuffs.

10. I. Karadjova, M. Karadjov, *Fresenius' J. Anal. Chem.*, **360**, 246 (1998).

11. Ordinance No 31/ 29.07.2004 of the Ministry of Health, Bulg. Gov. Gazette 88/08.10.2004 Commission Regulation (EC) No 1881/2006 of 19 December 2006 (Text with EEA relevance).

12. D. L. Massart, L. Kaufman, The interpretation of analytical chemical data by the use of cluster analysis, J. Wiley & Sons, New York, 1983, p. 237.

13. A. L. Page, A. C. Chang, M. El-Amamy, chapter 10 in: Lead, Mercury, Cadmium and Arsenic in the Environment, T. C. Hutchinson and K. M. Meema (eds.), John Wiley & Sons Ltd, 1987, p. 119.

14. G. Jansson, I. Öborn, *Ac. Agricul. Scandinavica, Sec. B . Soil & Plant Sci.,* **50** (2), 49 (2010). https://doi.org/10.1080/09064710050504982

15. G. Dziubanek, R. Baranowska, M. Ćwieląg-Drabek, A. Spychała, A. Piekut, M. Rusin, I. Hajok, *Ecotox. Environ Saf.*, **142**, 8 (2017). https://doi:10.1016/j.ecoenv.2017.03.048.

16. P. Verma, K. V. George, H. V. Singh, R. N. Singh, *Appl. Math. Model.*, **31**, 1652 (2007) https://www.sciencedirect.com/science/article/pii/S0307904X06001223.

17. Y. N. Jolly, A. Islam, S. Akbar, SpringerPlus **2**, 385 (2013) https://doi.org/10.1186/2193-1801-2-385.

18. G. Tóth, T. Hermann, M.R. Da Silva, L. Montanarella, *Env. Int.*, **88**, 299 (2016). https://doi.org/10.1016/j.envint.2015.12.017.

19. Bulgarian Food Safety Agency; Risk Assessment Center (2013) Cadmium as a pollutant in the environment - sources and toxicity to humans and animals. p. 1. babh.government.bg/uploads/File/COR_Aktualno/13-288/0147-1301.pdf.

Corrosion properties of systems based on ZrO$_2$ sol-gel films on Zn-Ni and Zn-Co alloys

N. D. Boshkova[1], V. D. Bachvarov[1], M. T. Peshova[1], I. Stambolova[2], D. Stoyanova[2], S. I. Smrichkova[1], T. N. Pham[3], T. T. Nguyen[3], D. L. Tran[3], N. S. Boshkov[1*]

[1]*Institute of Physical Chemistry "R. Kaishev", Bulgarian Academy of Sciences, Acad. G. Bonchev str., bl. 11, 1113 Sofia, Bulgaria*
[2]*Institute of General and Inorganic Chemistry, Bulgarian Academy of Sciences, Acad. G. Bonchev str., bl. 11, 1113 Sofia, Bulgaria*
[3]*Institute for Tropical Technology, Vietnam Academy of Science and Technology, 18 Hoang Quoc Viet, Cau Giay, Hanoi, Vietnam*

The presented investigations demonstrate the corrosion behavior and protective ability of two composite systems obtained on low-carbon steel in model corrosive medium of 5% NaCl solution. These systems consist of Zn-Co (3 wt.%) or Zn-Ni (10 wt.%) alloy coatings as an under-layer and very thin ZrO$_2$ sol-gel film as a top-layer. The surface morphology of the samples was studied with scanning electron microscopy (SEM). Their corrosion resistance was investigated by application of potentiodynamic polarization (PDP) curves, polarization resistance measurements (Rp) for a definite period of time (10 days) and electrochemical impedance spectroscopy (EIS). The results obtained were compared with the corrosion characteristics of an ordinary zinc coating with the same thickness. The experimental data present the positive influence of the newly developed composite systems for the enhanced protective properties of low-carbon steel in the test aggressive chloride-containing environment.

Keywords: corrosion, zinc, Zn-based alloys, ZrO$_2$ sol-gel film

INTRODUCTION

It is well known that steels are widely applied traditional materials in the transport industry, as well as for buildings, bridges, railway facilities, etc. However, their implementation often involves significant financial costs combined with the need for increased corrosion resistance. In that sense the application of low-carbon steels gives one more opportunity due to their lower cost combined with good mechanical and other parameters. Depending on the surrounding conditions these materials often demonstrate good corrosion characteristics especially if an additional protective surface film (metallic, sol-gel oxide, conversion, etc.) is available. One possible and economically viable approach for better protection of the low-carbon steel is the galvanizing [1-3].

The practical role of zinc is generally as a sacrificial coating since this metal is destroyed firstly during the corrosion processes, thus forming a protective layer of corrosion products with a low product of solubility value. It is observed that this layer can slow-down the corrosion rate depending on the aggressive medium. As well known, the protective characteristics of the zinc can be significantly enhanced by its alloying with Ni, Co, Mn, etc. [4-7].

In recent years, many researchers investigated the sol-gel coating types like TiO$_2$, ZrO$_2$, etc. which attracted considerable attention due to their ease of manufacturing, low cost, better mechanical stability and corrosion resistance. They also demonstrate good mechanical strength, hardness, wear resistance and chemical inertness. The deposition procedures are object of intensive research worldwide. In addition, multilayer systems provide in general better protective ability compared to single-layer coatings [8-11]. To the best of our knowledge the information on the deposition of such films on galvanized low-carbon steel and on Zn-based alloys, respectively, is rather scarce.

The aims of the present investigation are to obtain composite systems consisting of zinc-based alloy coatings - Zn-Co (3 wt.%) or Zn-Ni (10 wt.%) as under-layers and ZrO$_2$ sol-gel amorphous top film, to characterize their corrosion behavior in chloride-containing test medium and to compare the obtained experimental data with the corrosion properties of ordinary electrodeposited zinc.

MATERIALS AND METHODS

Sample types

Low-carbon steel plates with sizes 30 × 10 × 1 mm and composition (wt.%): C - 0.05–0.12; S ≤ 0.04; P ≤ 0.35; Mn - 0.25–0.5; Cr ≤ 0.1; Si ≤ 0.03; Ni ≤ 0.3; Cu ≤ 0.3; As ≤ 0.08; Fe - balance were used

* To whom all correspondence should be sent:
E-mail: NBoshkov@ipc.bas.bg

as substrates. Following systems were obtained on the latter:

    - System 1: Zn-Ni (10 wt.%) – under-layer / ZrO_2 – top-layer;

    - System 2: Zn-Co (3 wt.%) – under-layer / ZrO_2 – top-layer.

The zinc-based alloy coatings (as well as the ordinary zinc) were electrodeposited with practically equal thickness of about 11-12 μm, followed by deposition of ZrO_2 sol-gel layer according to the procedures described below.

System 1 – Zn-Co (3 wt.%) alloy coatings were obtained from an electrolyte containing 100 g/L $ZnSO_4.7H_2O$, 120 g/L $CoSO_4.7H_2O$, 30 g/L NH_4Cl and 25 g/L H_3BO_3 at pH 3.0–4.0, soluble zinc anodes and additives ZC-1 (wetting agent - 20 ml/L) and ZC-2 (brightener - 2 ml/L) [5]. Electrodeposition conditions: cathodic current density 2 A/dm², ambient temperature ~ 25 °C, no stirring, soluble zinc anodes, time – 20 minutes.

System 2 – Zn-Ni (10 wt.%) alloy coatings were obtained in a thermostated electrolytic cell with circulation from an electrolyte with a composition: 100 g/L $NiSO_4.7H_2O$, 100 g/L $NiCl_2.6H_2O$, 30 g/L $ZnCl_2$, 10 g/L β-alanine at pH ~ 4; cathodic current density 2 A/dm², temperature 40 °C, non-soluble Ti-Pt networks as anodes [6].

Ordinary zinc coating was electrodeposited from an electrolyte with composition 150 g/L $ZnSO_4.7H_2O$, 30 g/L NH_4Cl and 30 g/L H_3BO_3, pH 4.5-5.0, cathodic current density 2A/dm², soluble zinc anodes, 2 additives: wetting agent (AZ1), brightener (AZ2) [5].

ZrO_2 sol-gel layers were obtained from zirconium butoxide $Zr(OC_4H_9)_4$ diluted with isopropanol and some amounts of acetyl acetone and acetic acid (complexing agents). Next step was to add nitric acid and polyethylene glycol (PEG400). The final solution was diluted up to 0.2M and stirred for 2 h until appearance of yellowish-transparent color. Low-carbon steel samples, previously galvanized with Zn-Co (3 wt.%) or Zn-Ni (10 wt.%) alloy were immersed into the zirconium precursor solution and after withdrawing (rate of 30 mm/min) were dried at room temperature and subsequently at 100°C for 30 min. The deposition and drying of ZrO_2 coating were repeated 3 times [12, 13]. The final treatment was carried out at 380°C for 1 h.

SEM studies

The surface morphology of the investigated systems was studied with a scanning electron microscope INCA Energy 350 unit.

Potentiodynamic investigations

Potentiodynamic polarization (PDP) curves were obtained in a three-electrode glass cell with a volume of 300 mL. These measurements were performed in the range of ~ −1.2 to ~ +0.3 V at a scan rate of 1 mV/s. Reference electrode was saturated calomel electrode (SCE) while a platinum wire was the counter. The initial potential was chosen at ~150 mV cathodically to the corrosion potential and the scan was stopped at the moment of the fully disappearing of the protective system from the sample surface. VersaStat 4 PAR device was applied to realize these investigations [12, 13].

Electrochemical impedance spectroscopy

Electrochemical impedance spectroscopy (EIS) measurements were also realized with the VersaStat 4 PAR device in the same electrochemical cell. The measurements were carried out in the frequency range of 100 kHz to 10 mHz (potentiostatic mode) by superimposing an AC voltage of 10 mV after establishing a constant potential value.

Polarization resistance

This method was applied for checking the protective ability of the coatings toward the substrate as it is well known that the Rp value is inversely proportional to the corrosion current density according to the Stern-Geary equation [14]. The investigations were carried out with the "Corrovit" device specially designed for this type of measurements.

Corrosive medium

Electrochemical corrosion tests were performed in a 5% NaCl solution as model corrosion medium at pH 6.7 and ambient temperature.

Reproducibility

The results from the investigations were an average of 5 samples per type and per stage, i.e. for each measurement 5 replicates were conditioned for the measurements.

RESULTS

SEM studies

The surface morphology of the samples is demonstrated in Figure 1. The surface of the ordinary zinc is smooth and even, while this of System 1 is covered with some crack zones of different shape, width and depth. They are similar and somewhat reminiscent of the surface of previously well-known hexavalent chromium-based conversion films, the latter being subsequently banned for environmental reasons [15-18].
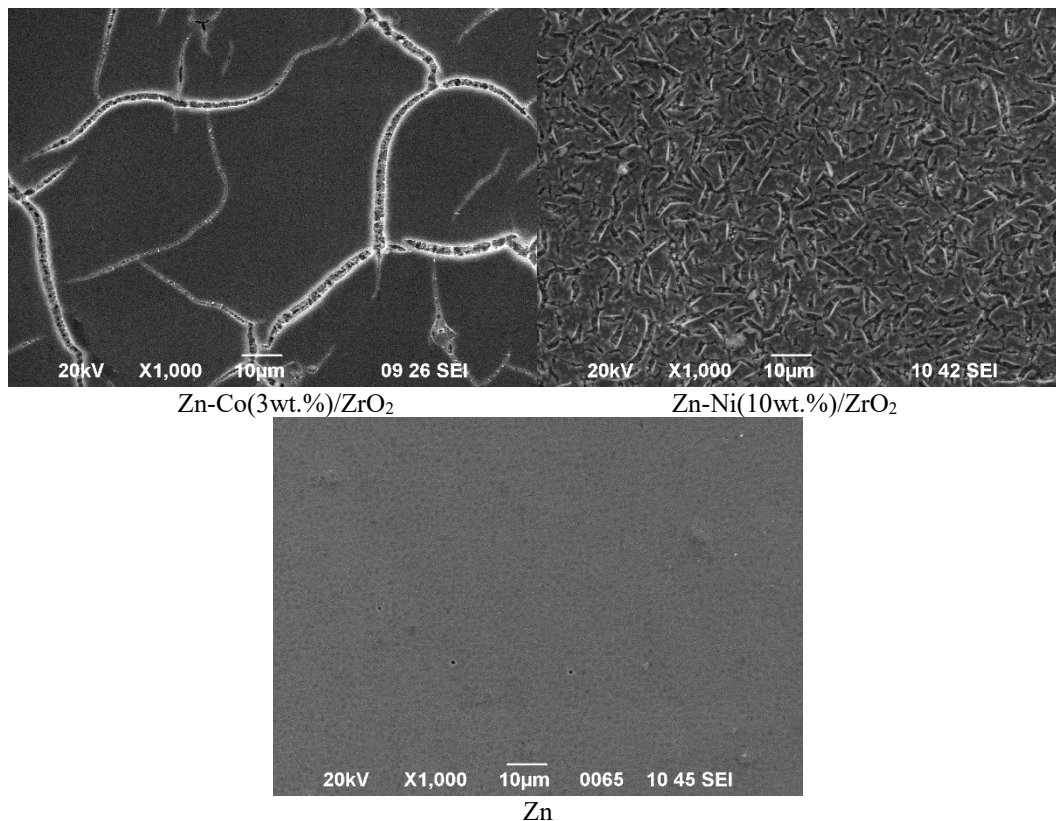
Zn-Co(3wt.%)/ZrO₂   Zn-Ni(10wt.%)/ZrO₂

Zn

Figure 1. SEM images of the investigated samples

The surface of System 2 also differs compared to both other samples - it is somewhat grooved and to a certain degree uneven. These results clearly show that the nature of the under-layer is of significant importance for the final surface morphology of the obtained systems. A possible explanation for these results could be sought in the differences in the thermal expansion coefficients of zinc (from one side) compared to Fe, Co and Ni since these parameters strongly differ, as well as in some physical and chemical parameters of the surface (morphology, hydrophobicity, etc).

Potentiodynamic investigations
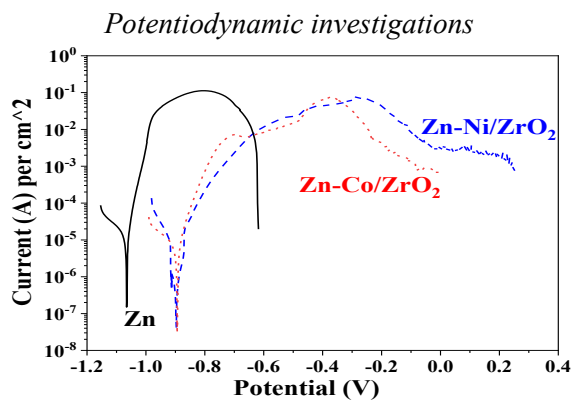
Figure 2. PD curves of the investigated samples in 5% NaCl model medium

The PDP curves of the investigated systems can be observed in Figure 2. It is evident that the ordinary zinc coating shows the shortest curve in the anodic zone which means that it lasts shorter time at external anodic polarization compared to both other samples. The curves of System 1 and System 2 are in general close in their course. Some differences appear for System 1 in the anodic branch – zones with higher and lower current density values especially in the potential interval of -0.7 – 0.35 V. The reason for this observation could be the availability of some cracks on the surface which could cause tearing off some scales during the anodic polarization leading to deeper penetration of the chloride ions. Another important parameter is the length of the anodic branch of the curves – it is well visible that System 2 shows a longer curve (with about 200 mV) which is a sign for higher corrosion resistance in that medium at these conditions.

Some important parameters of the PD curves – corrosion potential E_{corr}; corrosion current density I_{corr}; maximal anodic current density I_{max} - are summarized in Table 1.

Table 1. Electrochemical parameters of the PDP curves from Figure 2

Sample	E_{corr}, mV	I_{corr}, A.cm^{-2}	I_{max}, A.cm^{-2}
Zn	-1.065	$1.8.10^{-5}$	0.121
Zn-Co/ZrO₂	-0.895	$7.7.10^{-6}$	0.086
Zn-Ni/ZrO₂	-0.895	$5.3.10^{-6}$	0.084

Electrochemical impedance spectroscopy

The results from the EIS measurements are demonstrated in Figure 3. It can be observed that they are generally in quantitative correlation with the PDP curves. One of the most important parameters that briefly gives a reliable information concerning the protective characteristics of the investigated objects is the Z_{re} value measured on the X axe. This parameter is associated with the polarization resistance, the latter being inversely proportional to the corrosion current. It is obvious that the ordinary zinc has the lowest value – about 117 ohms. Both other investigated samples with a surface sol-gel layer demonstrate values of 158 ohms for System 1 and 162 ohms for System 2. These values are very close which could be partially explained with the nature of the film (from one side) and with short immersion times (up to receiving of a stabilized open circuit potential OCP - value).
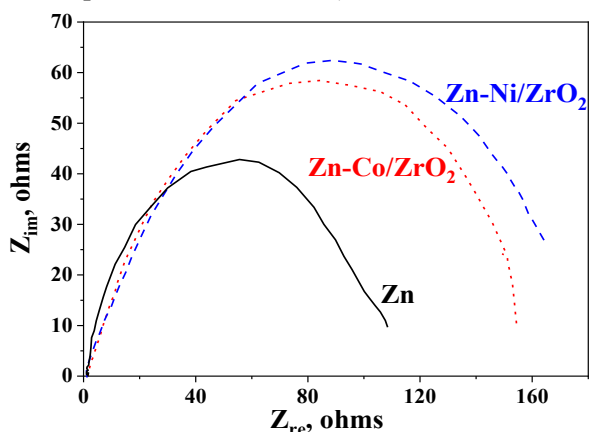
Figure 3. EIS spectra of the investigated samples in 5% NaCl model medium

Polarization resistance

The experimental results from the polarization resistance measurements for a time period of 10 days are demonstrated in Figure 4. It can be summarized that the Rp values of the ordinary zinc remain very close during the whole period being the lowest compared to both systems. Contrary to this System 1 shows gradually increasing values with a peak on the 4th day and a high Rp value of about 9000 ohms.cm^2 at the end of the test. The other investigated system – S2 – presents the highest Rp at the 10th day although very close to S1. These results clearly confirm the positive influence of the applied thin ZrO$_2$ sol-gel layer on the protective characteristics of the newly developed systems in that medium.
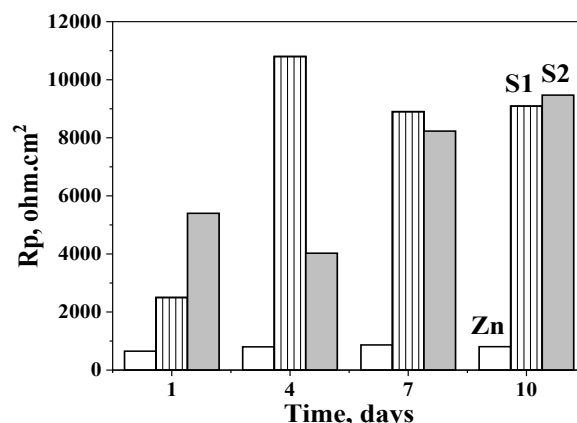

Figure 4. Polarization resistance (Rp) of the investigated samples in 5% NaCl model medium (S1 – System 1; S2 – System 2)

CONCLUSIONS

The obtained composite systems based on two types of selected zinc alloys coated with a top ZrO$_2$ sol-gel layer showed improved protective characteristics toward the low-carbon steel substrate compared to the ordinary zinc in a model medium with chloride ions as corrosion activators. The reason for this statement is the experimental data obtained by application of the selected methods. The polarization resistance of both systems at the end of the test period is about 10 times higher compared to the ordinary zinc. The other methods lead to less similar results which could be expected especially if taken into account that they are realized at much shorter test time and different conditions – for example, the potentiodynamic curves are realized at external polarization. Generally, the EIS spectra and SEM studies confirm the obtained experimental results. The latter can serve as a basis for further improvement of the protective characteristics of these systems, as well as to development of other protective types in order to prolong their service life.

REFERENCES

1. G. Koch, M. Brongers, N. Thomson, Y. Virmani, J. Payer, Corrosion cost and preventive strategies in the United States, NACE International, March 1, 2016.
2. X. G. Zhang, Corrosion and electrochemistry of zinc, New York, Plenum Press, 1996, ISBN 978-1-4757-9877-7.

3. N. Boshkov, K. Petrov, D. Kovacheva, S. Vitkova, S. Nemska, , *Electrochimica Acta*, **51**(1), 77 (2005).
4. N. Boshkov, *Surface and Coatings Technology*, **172** (2-3), 217 (2003).
5. N. Boshkov, K. Petrov, S. Vitkova, S. Nemska, G. Raichevski, *Surface and Coatings Technology*, **157** (2-3), 171 (2002).
6. V. Bachvarov, M. Peshova, S. Vitkova, N. Boshkov, *Central European Journal of Chemistry*, **12** (11), 1183 (2014).
7. A. Brenner, Electrodeposition of Alloys. Principles and Practice, Academic Press: NY, USA, 1963, p. 123.
8. R. Ayer, S. Ling, H.W. Jin, N. Pokutylowicz, J.Y. Koo, 17th International Offshore and Polar Engineering Conference, Lisbon, Portugal, July 2007, Paper Number: ISOPE-I-07-470.
9. J. B. Wachtman, A. R. Haber, Ceramic Films and Coatings, William Andrew Publishing, Noyes, New York/Norwich, 1993.
10. A. Kitiyanan, S. Sakulkhaemaruethai, Y. Suzuki, S. Yoshikawa, *Composites Science and Technology*, **66**, 1259 (2006).
11. K. P. Biju, M. K. Jain, *Sensors and Actuators B: Chemical*, **128** (2), 407 (2008).
12. K. Kamburova, N. Boshkova, N. Boshkov, G. Atanassova, Ts. Radeva, *Colloids and Surfaces* A, **559**, 243 (2018).
13. N. Boshkova, N. Tabakova, G. Atanassova, N. Boshkov, *Coatings*, **9** (8), 487 (2019).
14. M. Stern, A. L. Geary, *Journal of the Electrochemical Society*, **104**, 56 (1957).
15. , N. Boschkov, , G. Raichevski, , St. Raschkov, *Galvanotechnik*, **86** (9), 2819 (1995).
16. G. Raichevski, N. Boschkov, M. Nikolova, St. Raschkov, *Galvanotechnik*, **88** (8), 2554 (1997).
17. N. Boshkov, K. Petrov, S. Vitkova, G. Raichevski, *Surface and Coatings Technology*, **194** (2-3), 276 (2005).
18. Y. Toshev, V. Mandova, N. Boshkov, D. Stoychev, P. Petrov, N. Tsvetkova, G. Raichevski, Ch. Tzvetanov, A. Gabev, R. Velev, K. Kostadinov, Proceedings of the Second International Conference on Multi-Material Micro Manufacture (4M 2006), European Center for Micro- and Nanotechnology, Grenoble, France, **323-326**, 2006, p. 20.

Current opinion on the significance of promoting molecular modeling and simulation applications in Nigeria's future experimental catalysis and reaction engineering studies

T. Oyegoke[1,2]*, E. E. Peter[1], C. M. Igwebuike[3], B. El-Yakubu Jibril[1]

[1] Ahmadu Bello University, Chemical Engineering Department, PTDF Catalysis Research Centre, Zaria, Nigeria

[2] Université de Lyon, ENS de Lyon, Laboratoire de Chimie, 69007 Lyon, France

[3] IMT Atlantique, GEPEA, UMR CNRS 6144, 4 rue Alfred Kastler, F-44000 Nantes, France

The practice of researching any subject in the field of chemical reaction engineering and catalysis among experimentalists *via* the use of a try-and-error approach in the search for an understanding of reaction kinetics and the development of a new catalyst for the optimization of production yield is already an outdated approach going by the recent advances recorded in the aspect of computational science. The practice is often characterized by a randomized process of searching for a solution with much unclear information and an unclear direction to concentrate on where a feasible solution can be obtained. Most studies that deployed this approach have claimed a massive cost of materials demand due to the unclear direction to focus the research effort. In this report, we present simplified highlights on the modern concept of deploying saving costs often incurred in laboratory studies *via* the presentation of the molecular modeling approach concept and its potential benefits in facilitating chemical reaction engineering and catalysis studies. The mini-review would aid in educating and captivating the interest of the developing nations' experimentalists toward appreciating the place of computational studies in easing and directing the focus of their research to aid in saving possible expenses that would have been incurred in the use of the old traditional approach which is often expensive. A hybrid approach deploying computational techniques like molecular modeling and simulation to give the experimental studies direction would go a long way in facilitating research among several groups.

Keywords: Molecular modeling, Simulation, Chemical reaction engineering, Catalysis

INTRODUCTION

There is a natural urge in man to comprehend the environment he lives in and, when practical, influence nature for the greater good of mankind. The prehistoric drawings seen in the 1940s by anthropologists when they first visited the Lascaux cave in France made complete sense to them. Their forefathers had made models of the animal motions they had to rely on for survival thousands of years ago. One of the primary forces behind scientific discoveries was the primal human need to comprehend, simulate, and imitate nature. Leonardo da Vinci designed the Vitruvian Man in the 15th century to depict the proportions of the human body. The drawing was carried out to better understand the nature of the workings of the physical body. Molecular modeling aims to achieve the same goal of understanding nature. Scientists produced the first molecular models after learning about chemical structure. The first molecular representations of methane, ethane, and methyl chloride were presented by August Wilhelm von Hofmann, a German organic chemist, in 1865 at the Royal Institution in London. He also established a system of colors for distinguishing elements still in use. In 1953, Francis Crick and James Watson presented the first 3D model of DNA, which is undoubtedly the most well-known instance of this type of modeling. The contemporary era of molecular modeling has been ushered in by building upon earlier findings in attempts to comprehend nature. Even in today's fight against COVID-19, molecular modeling is a viable tool [1].

Molecular modeling is a fast-emerging area used to model and simulate small chemical and biological systems to understand and predict their behavior at the molecular level. It has many applications in various engineering sciences, such as materials science, chemical engineering, biomedical engineering, and many other fields. Knowledge of computational chemistry is essential to understanding the behavior of nanosystems; it is probably the easiest route or gateway to the fast-growing discipline of nanoscience and nanotechnology, which covers many areas of research dealing with objects that are measured in nanometers and are expected to revolutionize the

---

* To whom all correspondence should be sent:
E-mail: OyegokeToyese@gmail.com

industrial sector in the coming decades [2–4]. Since its advent, computational chemistry has grown to the state it is today and has become popular after immensely benefiting from the tremendous improvements in computer hardware and software during the last several decades. Computational chemistry can effectively solve complex chemical and biological problems with high computing power using parallel or grid computing facilities and faster and more efficient numerical algorithms [3]. This method can offer a wide range of benefits to various fields of study, like material analysis and design, reaction kinetics, catalysis, drug development, the design of corrosion-resistant materials, and many other applications. In any industry where the quality of products and improvements are centered on chemistry, the physical and electronic characteristics of materials can ideally benefit from molecular modeling [5]. The principle of molecular modeling has proven to be a valuable tool for providing predictive information ahead of any experimental studies. This can otherwise be seen as a pre-test to assess the innovative idea that a scientist or researcher experimentally synthesized in a wet laboratory. Such analysis can showcase the feasibility of such an idea and possible alternatives to achieve better the researchers' goal of synthesizing a defined material via a process and condition. In like manner, the molecular simulation tools can further find application in post-test studies where details would be explored at the molecular and atomistic scale level for the set of experimental observations made from the wet laboratory research studies.

Despite this wide range of advantages that the deployment of molecular modeling and simulation tools can potentially offer to experimental studies across different research subjects, a survey has shown that a lot of experimentalists are yet to embrace the deployment of these principles in their research works primarily in developing nations across different continents. Survey of experimental research works reported for developing countries in the literature indicates that the bulk of the reports does not deploy the use of computational approaches like molecular modeling in their studies; instead, they majorly focus on the use of only experimental methods. As the world continues to advance technologically, the need for these experimentalists (who are yet to understand the benefits this growing field can contribute to their experimental studies) to appreciate the position and significance of the computationalists (theoreticians) and not to take them for being game player who only engages in unrealizable activities is essential for experimental research advancement. There is also a need to

appreciably promote the computational science field [6–8] and tools, seeing the level of contributions it has made in advancing and guiding experimental research works in advanced countries reported in the literature [7, 9]. One of the advantages it has provided is the potential to supplement the shortcomings of experimental sciences. These supplementary aids include providing pre-information (before beginning experimental investigations) on how to appropriately approach the specified research problems in a laboratory study. Another advantage of such an approach is its ability to provide post-information (after carrying out experimental studies) to reveal theoretical details (at the molecular scale level) on why a specific experimental study failed to yield the set of expected results or details theoretical explanation for any other experimental observations made in a practical and the way forward approach for addressing the issue or challenge. In addition, some of these details are sometimes difficult to obtain, access, or understand by experimental techniques and are typically given by computer simulations.

To address this poor level of awareness about the potentials that molecular modeling and simulation (an aspect of theoretical science) can offer to complement experimental sciences, especially in developing nations where only experimental studies are appreciated while disregarding the significant values of theoretical (or computational) studies, we presented in this report the various applications of molecular modeling principles which have successfully been used in advancing the research and development of chemical reaction engineering and catalysis studies in the most developed or advanced countries. Understanding the various benefits or applications of this principle *via* a mini-review of existing literature would go a long way to educating the developing communities to embrace it and promote strong collaborations between the experimentalists and theoreticians (or computationalists) in our communities for the advancement of science and technology in general.

Identification of reaction mechanism

Molecular modeling has enabled researchers to explore the intrinsic reaction mechanism of different catalytic or non-catalytic and homogeneous or heterogeneous reactions [10, 11]. The surfaces of materials are usually modeled in the form of either clusters or slabs shown in Figure 1.
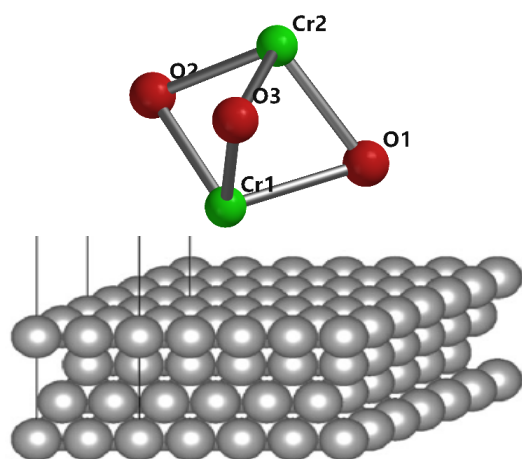
Figure 1. The Cr_2O_3 cluster model [12] and the Pt slab model [13].

The concept provides an understanding of the reaction path and the steps involved in the process. An example of a work that investigated the intrinsic reaction mechanism involved in the process is Oyegoke *et al.* [14], which studied the dehydrogenation of propane into propylene over the chromium oxide catalyst model, as shown in Figure 2. It highlights details on the effect of the participation of Cr-Cr and Cr-O sites in the oxidation of propane to yield olefin.

Understanding of reactions micro-kinetics

Chemical kinetics is a crucial study technique in the field of catalysis because the latter is fundamentally a kinetic process [16, 17]. Reactor design, reaction mechanism research, and explaining the structure-property link of a catalyst all require reaction kinetics data. Micro-kinetic modeling is utilized to better understand how to develop a catalyst to pinpoint crucial reaction intermediates and rate-determining elementary processes [18].

We now have a better understanding of the reaction involved in catalysis through the use of the micro-kinetics principle, which employs the results of molecular simulation and statistical thermodynamics calculation [19] to predict the evolution of both surface and gas-phase species throughout the reaction time for a certain amount of catalyst surface available at a specified time [19, 20]. The principles enable research to unveil the catalyst's performance in terms of yield, selectivity, and factor influencing the reaction's kinetic and catalyst deactivation.

Facilitated material selection process in catalysis

It has further facilitated the drive toward selecting the best materials to improve catalyst performance. It has equally saved materials and financial resources employed in screening a wide range of materials in the development/re-designing of catalysts for a specific reaction in question [21].

Figure 3 gives a practical deployment of the adsorption profile in the metal screening to facilitate propylene desorption (where the more negative the value, the more difficult desorption would be from such a surface). The profile predicted that introducing Mo would best improve the ease of desorption of propylene from the catalyst [22] during the dehydrogenation of propane into propylene, a vital feedstock for petrochemical production.

Another case for applying molecular modeling in material selection is the computational screening of catalysts for the Haber-Bosch process for manufacturing ammonia [23, 24] which has confirmed the optimal catalyst of iron and ruthenium [25] within the dissociative descriptor of nitrogen graphically displayed in Figure 5.

Moreover, the major factor is that the structure and composition of the optimal catalyst are a function of the prevailing reaction condition. After the successful confirmation of the traditional catalyst for the Bosch-Haber process, the same group came up with a combination of less expensive materials of Mo-Co alloy [25], which give a better catalytic property for the ammonia synthesis (see Figure 6).

Understanding of reaction energy barrier or demand

Molecular modeling has enabled theoretical studies to provide insight into the overall or approximate energy demand (in terms of the barrier) that must be met for the yield to improve, which has to be engineered by design measures that reduce the reaction barrier. The barrier is often computed *via* either the apparent activation energy model [26, 27] or the use of the energetic span approach [28–31]. A scheme in Figure 7 shows the computation approach for estimating the overall reaction energy barrier using the energetic span approach. Three elementary steps were used to illustrate different possible catalytic reaction cycles that could be obtainable in a simulation study.
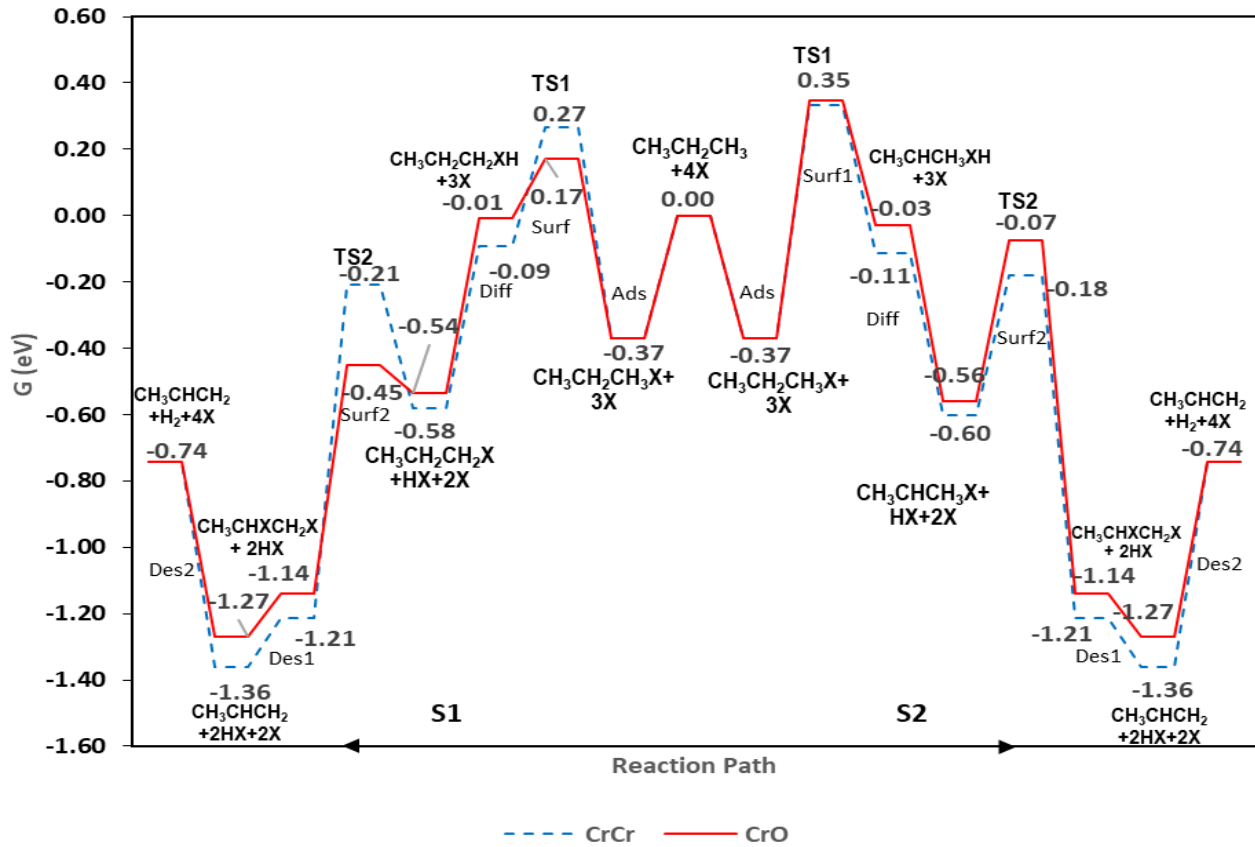
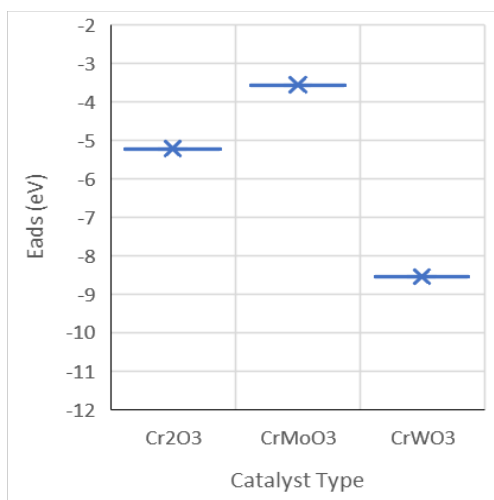**Figure 2.** Propane dehydrogenation reaction mechanism profile over Cr_2O_3 [14].

Figure 3. Adsorption profile for understanding the impact of Mo and Wo on Cr_2O_3 for ease of producing propylene [22].
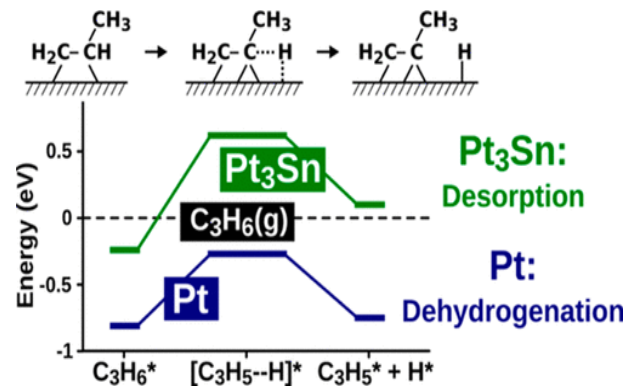

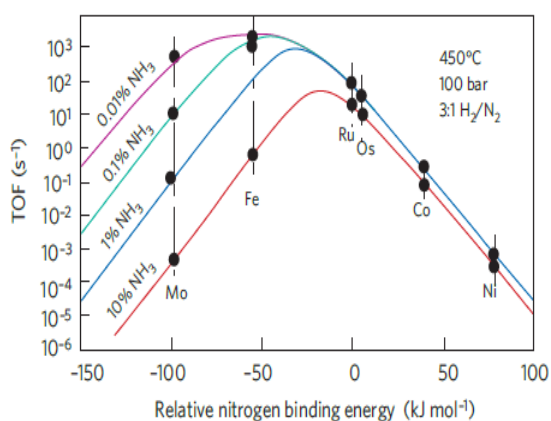**Figure 4.** Plot showing the impact of alloying Pt with Sn in a propane dehydrogenation [15].

Figure 5. Volcano curves for the turnover frequency (TOF) calculated based on micro-kinetic modeling using parameters calculated by density functional theory (DFT) [25].

Figure 6. Interpolation concept illustrating that binding energy for a CoMo catalyst is intermediate between the elemental catalyst Co and Mo [25].

The first case in Figure 7a is the single cycle model, which shows two sub-cases in blue (less energetic, flat, and efficient reaction profile) and red (low energy profile). In the blue case, a less stable intermediate compared to the reaction starting state (Io), where the energetic span was computed as the difference between the higher transition state (TDTS, that is, TOF-determining transition state) with the initial reaction state (Io) which was taken as the most stable intermediate (TDI, that is, TOF-determining intermediate) since no intermediate is less stable than Io. Another case, tagged as the red case in Figure 7a, shows a model stable intermediate (I_2) than the initial state of the reaction (Io), which makes I_2 become the TDI in such a case [28–31]. The cases presented for the single-cycle model in Figure 7a are possible cycles often expected during the catalysis of a chemical process.

However, some unexpected activities like the formation of the off-cycle intermediate, which are reversible (that is, Cx to Cy in Figure 7b), or catalyst deactivation, which are irreversible (that is, Cx to Cd in Figure 7c), are sometimes confirmed for some catalytic processes studied. In a case where the off-cycle intermediate (I_y) occurs and appears more stable than the on-cycle (I_x) one, the off-cycle intermediate (I_y) would be taken as the TDI. Using the catalyst deactivation model [31], we can compute the catalyst's turnover number (TON) in a simulation study. The TON value accounts for the mean cycle numbers a catalyst molecule can provide before deactivating. It can also be referred to as a catalyst's life span or expectancy, after which the catalyst remains inactive.
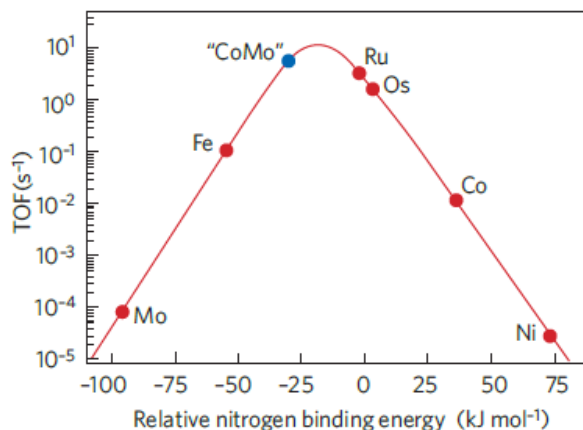
Another approach for computing the overall energy barrier in a chemical process studied is the use of a micro-kinetic simulation approach, where the reactor model and some other conditions are taken into consideration in such an approach. Some codes like MKMCXX, Micki, and many other micro-kinetic simulation codes have been developed to facilitate the deployment of the technique in chemical reaction engineering and catalysis studies. Moreover, these approaches' applications have been reported in the literature. Some works include one that attempts to evaluate the impact of Sn on the Pt [15] when alloyed together (in Figure 4), where the barrier was used to understand its role in influencing the catalysis. Figure 2 shows the effect of having a higher concentration of chromium site (Cr-Cr) in the CrO-based catalyst surface and a case of when oxygen participated (Cr-O) in the catalysis to reduce the activities of the chromium site. With the use of molecular modeling using density functional theory (DFT) calculation, Peter *et al.* [32] predicted promoting ZSM-5 catalytic activity of propane dehydrogenation with the introduction of gallium over zinc metal. The authors reached such deductions using the activation barrier of the rate-determining step identified in the study.

Improved rate of catalyst development

Every approach towards establishing atom and energy-efficient sustainable chemical technology relies heavily on catalysis. The improvement in understanding catalytic processes' fundamentals has been extensively facilitated by computational modeling and molecular simulations.
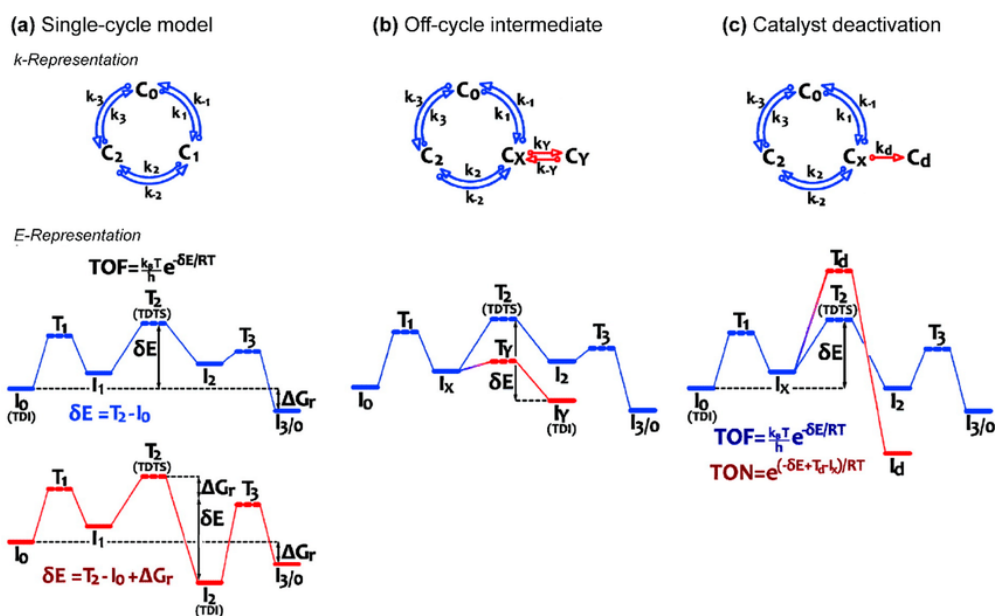
Figure 7. A pictorial illustration of the energetic span approach deployment in search for insight into the kinetics of a reaction mechanism where three cases are presented [31]: (a) single-cycle model, (b) off-cycle intermediate, and (c) catalyst deactivation.

The evaluation of spectroscopic data and the clarification of catalytic mechanisms depend very well on computations for an atomistic framework [33]. Concerns about the environment, resource use, safety, and overall process efficiency are some factors driving the continual search for the best process conditions and catalysts [7]. Previously, the majority of research in catalysis has been experimental. Although this is still the case, molecular modeling, and simulation are already widely acknowledged as crucial tools for the research and development of catalysts. Molecular modeling can offer fresh perspectives on reaction pathways, forecast the characteristics of catalysts yet to be developed, and integrate data for a given system from various experimental techniques into a single, logical image. Modeling and experimentation should work together, that is, in synergy; experiments should validate modeling while modeling should describe the results of an experimental study, indicate new ideas and scientific testing, or possibly replace laboratory tests in the screening of various process conditions or catalysts [34].

The use of computing facilities to theoretically carry out a pre-evaluation of the idea proposed on the right approach that best suits the modification/design of a catalyst for a specific reaction has dramatically promoted the speed at which the catalysts are developed across the globe, unlike the traditional approach of doing without it [20, 35].

Spectral findings by density functional theory

For a better understanding of the catalyst surface and intermediates proposed during the search for reaction mechanisms, which are the key ingredients for micro-kinetic modeling, the importance of spectroscopy must be emphasized. With the increased sophistication of the DFT and the incorporation of time-dependent DFT, the initial problem encountered with the Hartree Fork (lack of electronic correlation and calculation at ground state) in spectroscopy findings has improved significantly [36]. Theoretical spectroscopy such as ultraviolet–visible (UV-VIS), Raman, nuclear magnetic resonance (NMR), and infrared (IR) has thrown more light on experimental studies and given a better understanding of the nature of the surfaces and the intermediates involved during reaction [37–39]. Using advanced methods in molecular modeling and simulation tools, we can now effectively model and simulate different spectra for the vast range of materials synthesized in the wet laboratory. Some research in the literature [14] does deploy the use of these spectra to validate the material synthesized in the laboratory to understand better what kind of peaks are expected using the molecular modeled materials' spectra to identify if the type of material of interest is present in the product obtained using the set of peaks in the spectra. Like the case of synthesizing silicon oxide from rice husk materials [40, 41], pure silicon oxide spectra can be obtained *via* the deployment of molecular modeling tools and be used to compare with the spectra obtained for the

synthesized products instead of the traditional approach of using the standard table presented in chemistry books or literature to confirm the functional groups of the set of peaks found in the Fourier transform infrared (FTIR) spectra and many other applications.

CONCLUSIONS

Molecular-scale simulation has reached a stage of sophistication and accuracy, making it an essential field for chemical engineers and other physical scientists. These extensive applications of molecular modeling principles to reaction engineering and catalysis primarily have a strong capacity to save material resources incurred in catalyst development and chemical production process optimization studies. The promotion of the hybrid mode of studying reaction kinetics and catalysis would unfold in more detail about the factors responsible for several experimental observations made in a wet laboratory study. It would aid in providing roadmaps or compasses in terms of having preliminary insight into a clear pathway or procedure that has better feasibility of solving the defined research problem, unlike the deployment of the usual try-and-error design of experiments. Therefore, harvesting the benefits of this hybrid mode of studying the chemical processes would require the experimentalists' mutual agreement and readiness to collaborate with computationalists, otherwise known as theoreticians, to complement each other in ongoing and future research.

Conflict of Interest: *The authors declare no conflict of interest.*

REFERENCES

1. D. Chris, *eni Report*, 2020. https://www.eni.com/en-IT/scientific-research/healthcare-challenge-molecular-modeling.html.
2. P. W. Atkins, R. S. Friedman, Molecular Quantum Mechanics, Oxford University Press, New York, 1997.
3. K. I. Ramachandran, G. Deepa, K. Namboori, Computational chemistry, and molecular modeling: Principles and applications, Springer Berlin Heidelberg, 2008.
4. J. H. Warren, A Guide to Molecular Mechanics and Quantum Chemical Calculations, CA: Wavefun Inc, 2013.
5. G. Goldbeck, The economic impact of molecular modeling Impact of the field on research, industry and economic development. Cambridge: Goldbeck Consulting, 2012.
6. S. Maheshwari, S. Shetty, R. Ratnakar, S. Sanyal, *J. Indian Inst. Sci.,* **102**, 1 (2022).
7. L. Grajciar, C. J. Heard, A. A. Bondarenko, M. V. Polynski, J. Meeprasert, E. A. Pidko, P. Nachtigall, *Chem. Soc. Rev.*, **47**, 22 (2018), doi: 10.1039/C8CS00398J.
8. K. C. La, B. I. Dunlap, Molecular Dynamics - Theoretical Developments and Applications in Nanotechnology and Energy: The Roles of Classical Molecular Dynamics Simulation in Solid Oxide Fuel Cells," IntechOpen, London, 2012, doi: 10.5772/35352.
9. L. J. Broadbelt, R. Q. Snurr, *Appl. Catal. A Gen.*, **200**, (1–2) (2000), doi: 10.1016/S0926-860X(00)00648-7.
10. Y. A. Agafonov, N. A. Gaidai, A. L. Lapidus, *Kinet. Catal.*, **59**, 6 (2018), doi: 10.1134/S0023158418060010.
11. J. J. H. B. Sattler, J. Ruiz-Martinez, E. Santillan-Jimenez, B. M. Weckhuysen, *Chem. Rev.*, **114**, 20 (2014), doi: 10.1021/cr5002436.
12. T. Oyegoke, F. N. Dabai, A. Uzairu, B. Y. Jibril, *J. Serbian Chem. Soc.*, **86**, 3 (2021), doi: 10.2298/JSC200521044O.
13. K. Seok-Ho, L. Chang-Mi, L. Dong-Hee, *J. Korean Soc. Environ. Eng.*, **38**, 5 (2016), doi: 10.4491/KSEE.2016.38.5.242.
14. T. Oyegoke, F. N. Dabai, A. Uzairu, B. Y. Jibril, *Eur. J. Chem.*, **11**, 4 (2020), doi: 10.5155/eurjchem.11.4.342-350.2045.
15. L. Nykänen, K. Honkala, *ACS Catal.*, **3**, 12 (2013), doi: 10.1021/cs400566y.
16. R. W. Missen, C. A. Mims, B. A. Saville, Introduction to Chemical Reaction Engineering and Kinetics, John Wiley & Sons Inc., New York, 1999.
17. H. Lynggaard, A. Andreasen, C. Stegelmann, P. Stoltze, *Prog. Surf. Sci.*, **77**, 3–4 (2004), doi: 10.1016/j.progsurf.2004.09.001.
18. A. H. Motagamwala, J. A. Dumesic, *Chem. Rev.*, **121**, 2 (2021), doi.: 10.1021/acs.chemrev.0c00394.
19. A. Zagalskaya, I. Evazzade, V. Alexandrov, *ACS Energy Lett.*, **6**, 3 (2021), doi: 10.1021/acsenergylett.1c00234.
20. A. Ishikawa, Y. Tateyama, *ACS Catal.*, **11**, 5 (2021), doi: 10.1021/acscatal.5b01391.
21. M. Anand, B. Rohr, M. J. Statt, J. K. Nørskov, *J. Phys. Chem. Lett.*, **11**, 20 (2020), doi: 10.1021/acs.jpclett.0c01991.
22. T. Oyegoke, F. N. Dabai, S. M. Waziri, A. Uzairu, B. Y. Jibril, *J. Chem. Chem. Eng. Croat.*, **71** (9-10) (2022), doi: 10.15255/kui.2022.006.
23. S. Ghavam, M. Vahdati, I. A. G. Wilson, P. Styring, *Front. Energy Res.*, **9**, 34 (2021), doi: 10.3389/fenrg.2021.580808.
24. C. Smith, A. K. Hill, L. Torrente-Murciano, *Energy Environ. Sci.*, **13**, 2 (2020), doi: 10.1039/C9EE02873K.
25. J. K. Nørskov, T. Bligaard, J. Rossmeisl, C. H. Christensen, *Nat. Chem.*, **1**, 1 (2009), doi: 10.1038/NCHEM.121.
26. M. Carrier, L. Auret, A. Bridgwater, J. H. Knoetze, *Energy and Fuels*, **30**, 10 (2016), doi: 10.1021/acs.energyfuels.6b00794.
27. H. Chen, N. Liu, *J. Am. Ceram. Soc.*, **93**, 2 (2010), doi: 10.1111/j.1551-2916.2009.03421.x.
28. D. Garay-Ruiz, C. Bo, *ACS Catal.*, **10**, 21 (2020), doi:

10.1021/acscatal.0c02332.

29. S. Kozuch, S. Shaik, *Acc. Chem. Res.*, **44**, 2 (2011), doi: 10.1021/AR1000956.

30. A. Boje, W. E. Taifan, H. Ström, T. Bučko, J. Baltrusaitis, A. Hellman, *Catal. Sci. Technol.*, **11**, 20 (2021), doi: 10.1039/D1CY00419K.

31. M. Bourrez, F. Gloaguen, *New J. Chem.*, **39**, 10 (2015), doi: 10.1039/C5NJ00770D.

32. E. E. Peter, T. Oyegoke, A. Uzairu, A. Attah, B. Y. Jibril, Computational Design of Metal-Exchanged ZSM-5 Catalyst For Propane Dehydrogenation, ICTAC, 2022.

33. K. D. Vogiatzis, M. V. Polynski, J. K. Kirkland, J. Townsend, A. Hashemi, C. Liu, E. A. Pidko, *Chem. Rev.*, **119**, 4 (2019), doi: 10.1021/acs.chemrev.8b00361/asset/images/medium/cr-2018-00361x_0033.gif.

34. P. Kacer, M. Kuzma, D. Karhanek, J. Svrcek, L. Cerveny, *Chem. Cent. J.,* **21** (**2**), 1 (2008), doi: 10.1186/1752-153X-2-S1-P37.

35. M. Besora, F. Maseras, *Wiley Interdiscip. Rev. Comput. Mol. Sci.*, **8**, 6 (2018), doi: 10.1002/wcms.1372.

36. A. A. Altaf, S. Kausar, A. Badshah, Density Funct. Calc. - Recent Progresses Theory Application, in: Spectral Calculations with DFT, Intechopen, London, 2018, doi: 10.5772/intechopen.71080.

37. M. Katari, E. Nicol, V. Steinmetz, G. van der Rest, D. Carmichael, G. Frison, *Chem. – A Eur. J.*, **23**, 35 (2017), doi: 10.1002/chem.201700340.

38. P. Howlader, B. Mondal, P. C. Purba, E. Zangrando, P. S. Mukherjee, *J. Am. Chem. Soc.*, 1**40**, 25 (2018), doi: 10.1021/jacs.8b03946/suppl_file/ja8b03946_si_004.mpg.

39. A. G. Martynov, J. Mack, A. K. May, T. Nyokong, Y. G. Gorbunova, A. Y. Tsivadze, *ACS Omega*, **4**, 4 (2019), doi: 10.1021/acsomega.8b03500/suppl_file/ao8b03500_si_001.pdf.

40. P. P. Nayak, A. K. Datta, *Silicon*, **13**, 4 (2020), doi: 10.1007/S12633-020-00509-Y.

41. R. Yuvakkumar, V. Elango, V. Rajendran, N. Kannan, *J Exp Nanosci.*, **9**, 3 (2014), doi: 10.1080/17458080.2012.656709.

Targeting penicillin binding proteins (PBPs) by using bioactive geranial from essential oil of *Cymbopogan pendulus* against gram-positive and gram-negative bacteria: molecular docking and experimental approach

A. D. Sharma*, I. Kaur

PG Department of Biotechnology, Lyallpur Khalsa College Jalandhar, India

Worldwide antibiotic resistance developed in bacteria in response to the uncontrolled use of currently available antibiotics is a major concern. Therefore, by using computational biochemistry, it is necessary to discover and design novel antibacterial compounds with new formulations to overcome this problem. PBP (Penicillin binding proteins) have been cited as an appropriate target for therapeutic drug design. In this study, molecular docking followed by wet lab authentication was designed to estimate the effect of the potent bioactive molecule of geranial from *Cymbopogan pendulus* **e**ssential oil (LGO) against PBP1 protein. GC-FID (gas chromatography with flame-ionization detection) based composition profile, *in-silico* docking study was conducted by using Patchdock analysis followed by 2D and 3D interactions. GC-FID revealed geranial as main compound in *Cymbopogan pendulus* essential oil. The docking score indicated effective binding of geranial to PBP1. Interaction results indicated that PBP1 / eucalyptol complexes participate in both H-bond and hydrophobic interactions. Wet lab study validated the anti-bacterial potential of oil against gram-positive and gram-negative bacteria. Therefore, essential oil from eucalyptus plant may provide potential herbal treatment to mitigate bacterial infections.

Keywords: Bacteria, docking, lemon grass oil, geranial, herbal drug

INTRODUCTION

Worldwide bacterial resistance to antibiotics is a swiftly growing apprehension. It happened due to the emergence spread, and persistence of multidrug-resistant (MDR) bacteria, collectively known as "ESKAPE", which includes gram-positive and gram-negative species (*Enterococcus faecium, Staphylococcus aureus, Klebsiella pneumoniae, Acinetobacter baumannii, Pseudomonas aeruginosa,* and *Enterobacter spp.*), also known as "superbugs". These bacteria were frequently isolated in hospital environments and are resistant to traditional and conventional treatments [1]. They have been known to cause the majority of nosocomial infections. To mitigate bacterial infections, β-lactam antibiotics are excellent drugs for treatments. β-lactams were known to inhibit bacterial infections by binding to penicillin binding proteins (PBPs) which consist of high-molecular-mass (HMM) and low-molecular-mass (LMM) PBP subgroups and execute the penultimate steps of bacterial cell wall synthesis, so playing vital roles in cell survival [2]. Bacterial peptidoglycan provides resistance to bacteria not only by a capability to resist against internal intracellular pressure but also helps to maintain well-defined cell shape. The term 'PBP' has been cited in manuscripts to refer to any enzyme that recognizes and/or metabolizes β-lactams, independently of its function in the cell [3].

PBPs are involved in catalysis in transglycosylation (polymerization of the glycan strands) and transpeptidation (cross-linking between glycan chains), DD-carboxypeptidation (hydrolysis of the last D-alanine of stem pentapeptides) and endopeptidation (hydrolysis of the peptide bond connecting two glycan strands) and hence a major target for antibiotics [2].

Antibiotic resistance has emerged in response to the misuse of currently available antibiotics. Hence, by using computational biochemistry, it is indispensable to discover and design novel antibacterial compounds with new formulations to overcome serious infections [5, 6]. Bacteria possess a variable number of PBPs and among all PBP1 is a high-molecular-weight trans-peptidase, a vital enzyme involved in peptidoglycan synthesis in bacteria cell wall [4]. It was reported that blocking of either carboxypeptidation or transpeptidation reactions by β-lactam antibiotics, deteriorates the peptidoglycan and may cause cell death [5]. This influential process, which has made penicillin and its analogues the most extensively engaged antibiotics for any infectious worldwide over the past, has been confronted by the broadcast of drug-resistant strains, emphasizing the necessity for novel natural antibiotic therapies [5, 6]. In this regard, inhibition of the glycosyltransferase reaction by the natural product moenomycin against

---

* To whom all correspondence should be sent:
E-mail: arundevsharma47@gmail.com

PBP4 has also been reported to weaken the peptidoglycan and kill bacterial cells [6]. Earlier docking studies on flavonoids like kaempferol, 3-rutinoside-7-sophoroside and rutin also demonstrated a considerable binding affinity to PBP2 and suggested that kaempferol, 3-rutinoside-7-sophoroside, amentoflavone and rutin may be considered as drug candidates for therapeutic aims in several human infections associated with *Staphylococcus aureus* [7]. Hence, by virtue of its crucial role, PBP1 is considered as an appropriate target for developing bacterial inhibitors. Inhibition of PBPs protein activity would block replication of bacteria. Since in humans, not at all any PBPs with comparable cleavage specific are recognized, so inhibitors are improbable to be considered as toxic. PBP1 topology constitutes: a trans-membrane anchor, a cytoplasmic tail, and two domains joined by a beta-rich linker located on the outer surface of the cytoplasmic membrane where cell wall peptidoglycan synthesis takes place [3]. The antibacterial activity of β-lactams is arbitrated by covalent binding to PBPs, thus inhibiting the transpeptidase (TPase) activity of PBP-mediated bacterial cell wall synthesis [5, 6]. Since bacterial resistance to multiple drugs, including β-lactam antibiotics, is a main therapeutic problem, thus, development of new chemical entities as antibacterial agents is urgently needed [8]. It was argued that gram-positive and gram-negative bacteria have mostly established resistance to all the available antibiotics and pose a grave problem not only in hospitals but also for the general population [2, 9].

Lemon grass essential oil (LGO) from *Cymbopogon* species also known as lemon grass, encompasses a number of bio-activities. Due to the complex nature of the essential oil, its anti-fungal mechanism of action is still not completely understood [10]. LGO has long history of being used as complementary and traditional medicine in ancient times. In addition, various potent biological activities like anti-amoebic, anti-inflammatory, anti-filarial, anti-diarrheal, anti-malarial, anti-fungal anti-HIV and anti-bacterial agent, have been attributed to LGO, hence playing a major role as a therapeutic in the scientific community [11]. This study postulated that due to the richness of geranial, essential oil from *Cymbopogon pendulus* plants has a potential to inhibit bacterial infections. Hence, as an objective this study was designed to study molecular docking of geranial and carry out wet lab validation of the anti-bacterial potential of lemon grass oil in relation with PBP1. The present study outcomes would offer scientists and doctors with prospects to identify the key anti-bacterial drugs to combat MDR.

EXPERIMENTAL

GC-FID analysis

LGO was extracted from fresh leaves of *Cymbopogan pendulus* growing naturally on nearby areas of Lyallpur Khalsa College, Jalandhar. The *Cymbopogan pendulus* was authenticated by Dr. Upma from the Botany Department and voucher with number BT103 was deposited in the Department of Biotechnology. Hydro-distillation method was used for extraction of essential oil by using a clevenger-type apparatus (Borosil, India) [12]. To identify bioactive compounds in EO, GC-FID study was carried out (GC-FID, Chemtron 2045). The column specification was: 2 m long, stainless steel having 10% OV-17 on 80-100% mesh chromosorb W (HP). Nitrogen was used as carrier gas at a flow rate of 35 ml/min. 0.2 µl LEO sample was used. The temperatures for detector and injector were: 220 °C and 270 °C. Oven ramping conditions were: 100°C (firstly maintained) ramped to 210 °C at 3 °C/min. Bioactive constituents in LEO were identified by comparing relative retention times (RT) of GC-FID spectra of LEO with authentic standards and literature data.

Ligand preparation

For bacterial receptors (PBP1), geranial was used as a ligand for structures. To build 3D structure of the ligand, SMILES of geranial was recovered from NCBI-Pubchem database. The structure was built by using UCSF-chimera.

Molecular docking

Crystal structures of PBP1 bacterial penicillin binding protein were recovered from PDB (https://www.rcsb.org/). Before docking analysis, all target enzymes were cleaned from H_2O molecules, cofactors, co-crystallized ligand, and energy-minimized. Then all protein target structures were prepared by means of the dock prep set up in UCSF-chimera. It is the process under optimization that determines bond length, charges anomalies and corrects atomic structure. PatchDock tool was used for docking of ligands over PBP1 (https://bioinfo3d.cs.tau.ac.il/PatchDock/). To execute docking, both receptors and ligand molecules as "pdb files" were uploaded to the PatchDock and docking was performed. For 2D and 3D interactions in docked complexes, Biovia 2020, UCSF-chimera and Plip tools [13] were used.

Active sites prediction

In fungal receptors, identification and dimension of cavities on 3D active sites were computed by using CASTp web tool. For this all structures in "pdb" format were uploaded to server and prediction was executed with probe radius value of 1.4 Å.

In-vitro anti-bacterial activity

The *in-vitro* antimicrobial activity of LGO was determined through agar disc diffusion method against four test organisms, gram-negative *Escherichia coli* (MTCC 40), *Pseudomonas aeruginosa* (MTCC 424), and gram-positive *Staphylococcus aureus* (MTCC 3160) and *Bacillus subtilis* (MTCC 121). Pathogens were purchased from the Institute of Microbial Technology, Chandigarh. Sterile paper discs (10 mm in diameter) were impregnated with 100 µl of LGO. 12-h cultures were used. Inocula and OD of suspensions were adjusted to 0.6. A swab of bacteria suspension was spread on to LB-agar plates and allowed to dry for 30 min. The discs with essential oil were then applied and plates were left for 20 min at room temperature to allow diffusion of oil followed by incubation at 37°C for 24 hours. Zone of inhibition was measured. Vancomycin antibiotic (10 mg) was used as positive control.

RESULTS AND DISCUSSION

GC-FID analysis of bioactive molecules in LGO

The GC-FID chromatogram obtained is depicted in Figure 1. The peaks observed and their respective retention times are also displayed. The GC-FID analysis of lemon grass oil obtained from *Cymbopogon pendulus* revealed 26 compounds for the total of 100%. In the present study, all identified compounds were micrene, limonene, linalool, geraniol, neral, undececanone and geranial acetate. GC-FID chromatogram contained three major peaks along with many small peaks indicating the presence of minor compounds. The major and minor constituents were geraniol (45%, geranial), neral (20%), undecanone (20%), linalool (8%), myrcene (6.7%), cuparene (11%), limonene (2.3%) and micrene (2%). The small peaks may be ascribed to disintegrated major bioactive compounds. The literature studies also showed the presence and identification of mycrene, citral-a, and citral-b in lemon grass oil obtained from *C. flexuous* [11]. During the course of time, use of LGO has become a major area of health- and medical-related research due to richness of bioactivities. LGO has also been used as therapeutic agent in pharmaceutical preparations as anti-oxidative, antibacterial, antiviral, anti-diabetic, anti-tumor, antifungal, anti-obesity, anti-hypertensive, anti-histaminic, anti-cancer, anti-HIV and hepatoprotective agent [11]. In this study two major and 3 minor bioactive compounds as cited above were selected for 3D docking.

Molecular docking

Structure-based drug design (SBDD) is most widely used as *in-silico* technique in making drugs, which is based on 3-D structures. *In-silico* docking has simplified investigators to screen conformations and affinities of an assembly of bioactive components against receptors [14]. Present study aimed at docking of geranial bioactive molecule from LGO as key anti-bacterial inhibitor candidate against PBP1. From docking analysis, it was apparent that geranial ligand efficiently docked with PBP bacterial enzyme. 3D docking results illustrated that PBP1 depicted strong binding with geranial ligands (Table 1) as apparent from its docking score. 3D model displaying docking poses and 2D/3D interaction of eucalyptol with PBP1 is shown in Figure 2. Hydrophobicity view depicted that ligands sre firmly bound within binding pocket of receptors. With PBP1, geranial ligand docked with penicillin binding domain of PBP1. The C-terminal module is responsible for the transpeptidase activity of PBPs catalyzing peptide cross-linking between two adjacent glycan chains in peptidoglycan cell wall synthesis [9, 15]. It was cited that blocking of either the transpeptidation or carboxypeptidation reactions by β-lactam antibiotics or therapeutic inhibitors weaken the peptidoglycan and may engender cell death [7]. Once a PBP is acylated by therapeutic inhibitors, it is unable to catalyze hydrolysis of the covalent acyl-enzyme intermediate and is inactivated; peptidoglycan transpeptidation cannot occur, and the cell wall is weakened [16, 17]. Based on analysis, it was highlighted that LGO can be used as effective source of anti-bacterial compounds.

Through 3D docking, with site residues of receptors, the ligand could form H-bonds or hydrophobic bonds which designate the affinity of ligand toward receptor [18]. Hence, docking interactions of geranial with PBP1 were further evaluated. It was observed that geranial ligand participates in both H-bond and hydrophobic interactions with PBP1. With PBP1 receptors, hydrophobic interactions were detected *via* TRP411, ASN562 and PHE577 at 3.74, 2.68 and 3.69 Å (Figure 2).

Table 1. Molecular docking, 3D interactions of geranial with PBP1

Solution No	Score	Area	ACE	Transformation
1	3424	396.50	-90.00	0.73 -0.72 2.66 94.93 10.88 42.52
2	3274	346.10	-105.92	2.24 -0.02 3.01 98.42 39.00 54.25
3	3262	352.80	-81.80	-2.87 -0.44 -1.23 87.53 14.38 47.09
4	3122	336.50	-115.80	0.63 -1.14 0.89 96.06 38.17 55.23
5	3112	369.50	-80.45	-1.95 0.07 2.39 96.01 10.41 40.13
6	3106	414.80	-89.98	1.32 0.20 -0.05 95.51 11.70 41.86
7	2988	376.00	-88.97	-0.77 -0.66 -0.38 96.51 9.59 40.06
8	2916	340.80	-122.79	-2.03 0.95 2.88 95.65 37.49 55.58
9	2904	340.90	-144.34	-1.26 0.79 -0.38 98.08 9.86 46.52
10	2894	324.90	-95.87	0.36 0.74 2.92 98.37 7.83 39.82
11	2876	347.30	-91.53	-1.95 0.91 -2.64 75.44 28.61 24.83
12	2872	329.10	-69.69	1.89 -0.13 -1.39 101.39 34.97 51.74
13	2856	319.80	-81.93	-0.98 -0.58 0.19 99.45 37.45 52.81
14	2848	311.30	-3.62	1.42 -0.51 -2.24 102.98 14.24 39.92
15	2824	320.40	-61.45	2.08 0.71 2.31 86.56 14.71 47.20

Hydrophobic   Interactions

Index	Residue	AA	Distance	Ligand Atom	Protein Atom
1	411B	TRP	3.74	3170	1254
2	562B	ASN	2.68	3172	2420
3	577B	PHE	3.69	3170	2551

Hydrogen   Bonds

Index	Residue	AA	Distance H-A	Distance D-A	Donor Angle	Protein donor?	Side chain	Donor Atom	Acceptor Atom
1	370B	SER	3.11	3.63	115.24			933 [O3]	3178 [O3]
2	428B	SER	2.21	3.10	152.67			3178 [O3]	1400 [O2]

Table 2. Antimicrobial analysis of lemon grass essential oil

Strain	Strain type	Zone of inhibition (cm)	
		C	EO
Pseudomonas aeruginosa	Gram-negative	3.0	FI
Escherichia coli	Gram-negative	2.5	6.5
Bacillus subtilis	Gram-positive	2.6	FI
Staphylococcus aureus	Gram-positive	2.5	FI

Here: C= positive control (vancomycin antibiotic, 10 mg), EO= essential oil, FI: 100% inhibition, values are expressed as mean±SD (*n*=3).
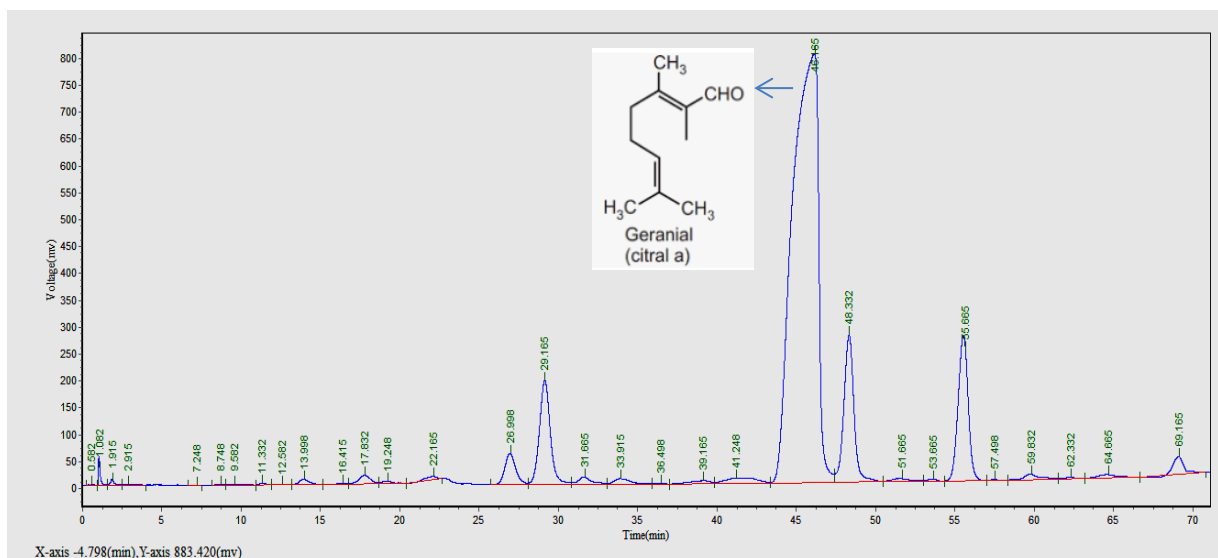
RT (min)	Compound	Concentration (%)
13	micrene	2.2
17	limonene	2.3
22	caryophyllene oxide	1.2
26	linalool	8.2
29	cuparene	11.2
31	epi-α-cadinol	2.0
33	δ-cadinol	2.1
39	aristolone	0.8
41	santalol acetate	1.9
46	geranial	45.2
48	neral	20.1
51	methyl octadecanoate	0.9
53	incensoleacetate	0.8
55	undececanone	20.0
59	heyderiol	1.3
64	hinokiol	0.6
69	geranial acetate	6.7

Figure 1. GC-FID analysis of lemon grass essential oil

It was noted that geranial exhibited H-bond by SER 378, and SER 428. CASTp active sites prediction quantified interacting residues in the active site cavities of PBP1 receptors (data not shown). In PBP1 enzymes, a main pocket was documented with volume (SA) of 214 and area (SA) of 376. Main pocket contained active site residue SER 378. Earlier study documented the role of active site residue SER 378 as a nucleophile that has been implicated in the catalytic mechanism in cell wall synthesis [4]. Meanwhile, geranial showed good affinity to PBP1 enzyme *via* SER residue, so it was conjectured that upon binding with ligand PBP1 becomes closed, thus, in-turn persuades change in conformation of bacterial enzymes and inhibits biosynthetic pathway involved in cell wall synthesis. Earlier studies also documented that β-lactam antibiotics irreversibly acylate the active-site serine of PBPs, which deprives bacteria of their biosynthetic functions and results in bacterial death [19]. All these events halt bacterial viability, thus mitigate infectivity of bacteria into the host cell. Similar *in-silico* results citing antibacterial potential of polypharmacological natural agents like flavonoids, phenolics, steroids, and terpenoids, which have the ability to inhibit and kill bacteria strains have been stated [20-22].
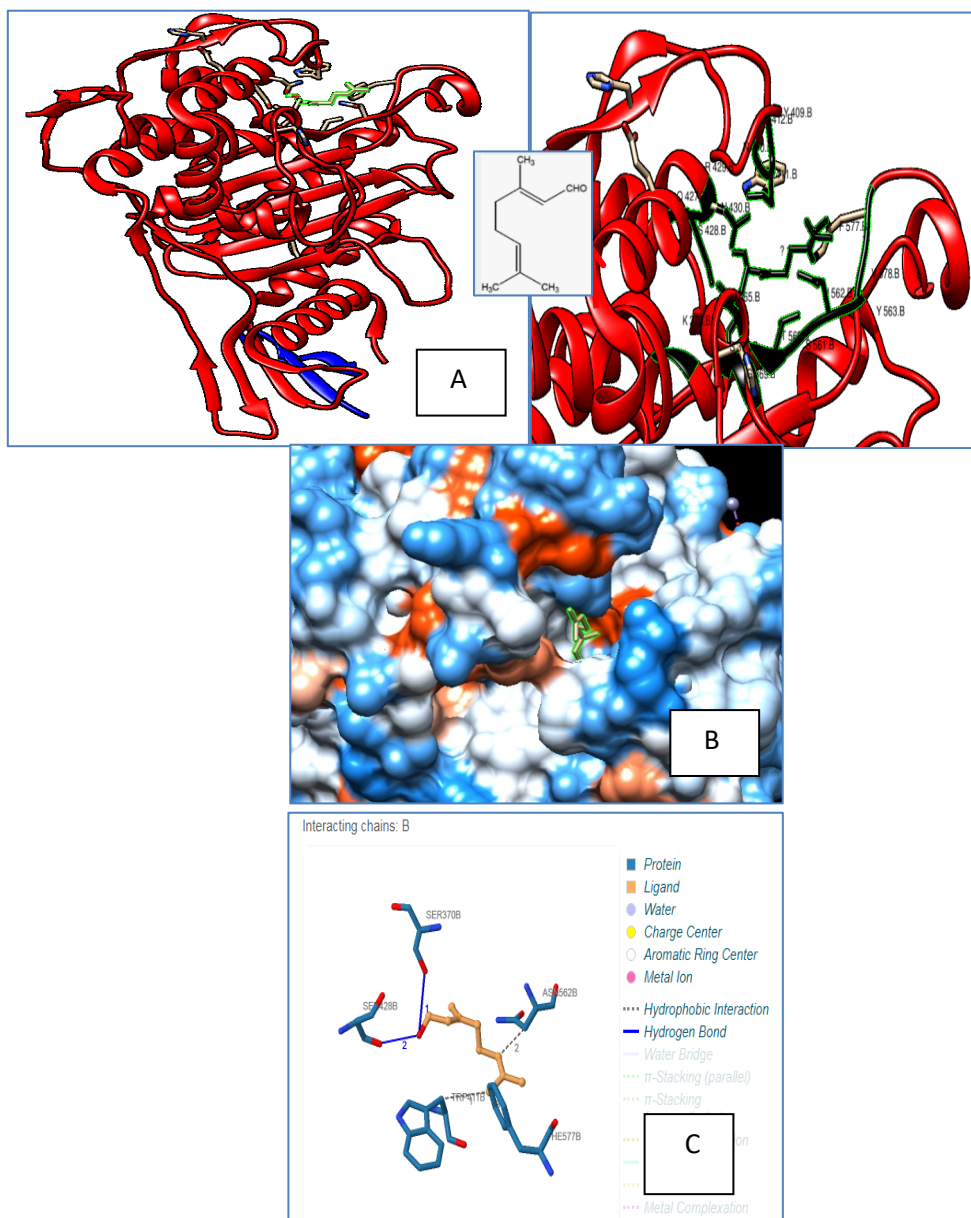
Figure 2. PBP1-citral model (A), Hydrophobic view (B) and 3D interactions of ligand-receptor. Red and green arrows indicate ligand geranial

Anti-bacterial activity

In the present study the *in-vitro* anti-bacterial activity of LGO was quantitatively assessed against drug-resistant microbial strains of *Escherichia coli* (MTCC-40), *Bacillus subtilis* (MTCC-121), *Pseudomonas aeruginosa* (MTCC-424) and *Staphylococcus aureus* (MTCC-3160), the results of which are depicted in Table 2 and Figure 3. The present study shows that LGO exhibits substantial antimicrobial activity against gram-negative *Escherichia coli* (MTCC-40) while total inhibition is seen for gram-positive *Bacillus subtilis* (MTCC-121), *Pseudomonas aeruginosa* (MTCC-424) and *Staphylococcus aureus* (MTCC-3160) as indicated in Figure 3. The variance action of LGO might be due to the incidence of a single target or multiple targets for their activity. The antimicrobial activity of LGO may arise due to the presence of major and minor bioactive components that affect hydrolytic enzyme inhibition (proteases) or inhibit partners like: cell wall enveloped proteins, microbial adhesions, and non-specific interactions with carbohydrates [23]. Earlier studies also have cited that anti-microbial activity was not always related to the high content of one chemical compound, rather than to synergic effects between major and minor components (Elaissi *et al.,* 2012) [24]. Siramon *et al.,* [25] also cited incidence of potent bioactive

molecules like flavonoids, and terpenoids behind the antimicrobial activity.

Same authors cited that bioactive molecules have tendency to pass across the cell membranes and to induce biological reactions, thus upsetting electron flow, the proton motive force, active transport and coagulation of the cellular contents. geranial, the major constituent of LGO also exhibits high antifungal, insecticidal and bactericidal activity [25].

In the present study high antimicrobial toxicity of LGO toward gram-negative bacteria was established which is a noteworthy observation as most studies suggest that the gram-negative bacteria are more resistant than the gram-positive bacteria due to the thick peptidoglycan layer, lipopolysaccharides, phospholipids of the cell wall that permit gram-negative bacteria to be resistant to most of the hydrophobic antibiotics and toxic drugs [26].
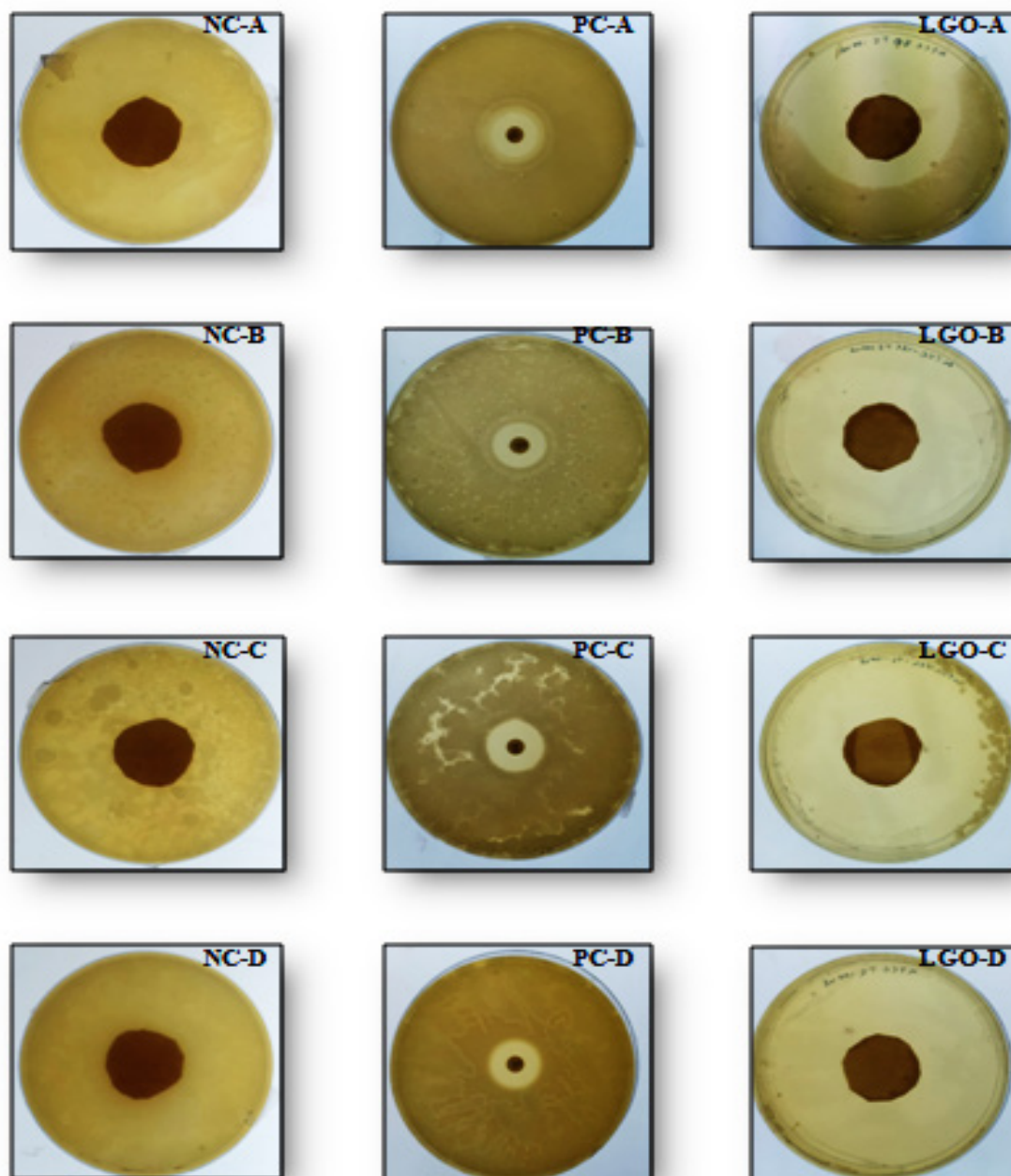
Figure 3. Anti-bacterial activity of LGO against MTCC-121, MTCC-40, MTCC-424 and MTCC-3160. Codes NC, PC and LGO are for negative control (blank), positive control and lemon grass oil and codes LGO-A, LGO-B, LGO-C and LGO-D represent MTCC-40, MTCC-121, MTCC-424, and MTCC-3160, respectively.

CONCLUSIONS

Currently, antibiotic resistance against gram-positive and gram-negative bacteria has emerged in the human population, and is a potential threat to global health, worldwide. The main target for bacterial infections are primarily PBPs. The aim of this study was to examine bioactive molecules from lemon grass essential oil that may be used to inhibit the bacterial infection pathway. Docking study revealed effective binding of ligand geranial with PBP1. Wet-lab study indicated that *Cymbopogan pendulus* **e**ssential oil was effective to inhibit tested pathogens. Therefore, we suggested that geranial may offer potential treatment options. It is found in medicinal plants that may act as potential inhibitors of bacterial PBPs. This study paved the way for researchers and a specific direction in the field of computational biochemistry and computational drug design. The present study described a new perspective that gives other researchers the opportunity to evaluate the proposed structures with more detailed studies in the field of computational biochemistry. Hence, further studies may be conducted for the validation of these compounds using *in vitro* and *in vivo* models to pave a way for these compounds in drug discovery.

REFERENCES

1. M. A. Brockhurst, F. Harrison, J. W. Veening, E. Harrison, G. Blackwell, Z. Iqbal, C. Maclean, *Nat. Ecol. Evol.,* **3,** 515 (2019).
2. E. Sauvage, A. Derouaux, C. Fraipont, M. Joris, R. Herman, M. Rocaboy, M. Schloesser, J. Dumas, F. Kerff, M. Nguyen-Distèche, P. Charlier, *PLoS One,* **9,** e98042 (2014).
3. Z. Lu, H. Wang, A. Zhang, X. Liu. W. Zhou, C. Yang, L. Guddat, H. Yang, C. J. Schofield, Z. Rao, *Mol. Pharmacol.,* **97,** 287 (2020).
4. M. A. Welsh, K. Taguchi, K. Schaefer, D. Van Tyne, F. Lebreton, M. S. Gilmore, D. Kahne, S. Walker, *J. Am. Chem. Soc*., **13,** 17727 (2017).
5. L. C. Chan, A. Gilbert, L. Basuino, T. M. da Costa, S. M. Hamilton, K. R. Dos Santos, H. F. Chambers, S. S. Chatterjee, *Antimicrob. Agents Chemother*., **60,** 3934 (2016).
6. E. A. Masters, K. L. de Mesy Bentley, A. L. Gill, S. P. Hao, C. A. Galloway, A. T. Salminen, *PLoS Pathog.,* **16,** e1008988 (2020).
7. M. Masumi, F. Noormohammadi, F. Kianisaba, F. Nouri, M. Taheri, A. Taherkhani, *Int. J. Microbiol.* **4,** 9130700 (2022).
8. N. G. Simoes, A. F. Bettencourt, N. Monge, I. A. C. Ribeiro, *Mini Rev. Med. Chem*., **17,** 1364 (2017).
9. C. Contreras-Martel, A. Martins, C. Ecobichon, D. M. Trindade, P. J. Mattei. S. Hicham, P. Hardouin, M. E. Ghachi, I.G. Boneca, A. Dessen, *Nat. Commun.,* **8,** 776 (2017).
10. F. Mancianti, V. Valentina, *Molecules*, **25** (3), 678 (2020).
11. O. S. Oladeji, F. E. Adelowo, D. T. Ayodele, K. A. Odelade, *Scientific African*, **6,** e00137 (2019)**.**
12. S. Sharma, H. Shagufta, D. Sahu, J. Gupta, *Medicinal Chemistry,* **17,** 2 (2021).
13. M. F. Adasme, K. L. Linnemann, S. N. Bolz, F. Kaiser, S. Salentin, V. J. Haupt, M. Schroeder, *Nucleic Acids Research*, **49,** W530 (2021).
14. P. Singh, K. Kumari, S. K. Awasthi, R. Chandra, *Int. J. Drug Dev. Res*., **8,** 49 (2016).
15. M. P. Barcellos, C. B. Santos, L. B. Federico, P. F. Almeida, C. H. T. P. da Silva, C. A. Taft, J. *Biomol. Struct. Dyn.*, **37,** 966 (2019).
16. D. Straume, K. W. Piechowiak, S. Olsen, G. A. Stamsås, K. H. Berg, M. Kjos, M. V. Heggenhougen, M. Alcorlo, J. A. Hermoso, L. S. Håvarstein, *Proc. Natl. Acad. Sci' U S A,* **17,** 6129 (2020).
17. E. A. Masters, K. L. de Mesy Bentley, A. L. Gill, S. P. Hao, C. A. Galloway, A. T. Salminen, *PLoS Pathog.,* **16**(10): e1008988 (2020).
18. T. M. Moon, É. D. D'Andréa, C. W. Lee, A. Soares, J. Jakoncic, C. Desbonnet, M. Garcia-Solache, L. B. Rice, R. Page, W. Peti, *J Biol Chem*., **293,** 18574 (2018).
19. S. L. Lima, A. L. Colombo, J. N. de Almeida Junior, *Front. Microbiol*., **10,** 2573 (2019).
20. P. I. O'Daniel, Z. Peng, P. Hualiang, A. Sebastian, D. Derong, S. Edward, L. Erika, A. Marc, Y. Takao, A. Valerie, *Journal of the American Chemical Society,* **136,** 3664 (2014).
21. E. Apriyanti, D. Kurnia, *Comb. Chem. High Throughput Screen.,* **23**, 1 (2020).
22. N. Soviati, A. S. Widyarman, *J. Indones. Dent. Assoc.,* **3,** 11 (2020).
23. D. Kurnia, E. Apriyanti, *Curr. Drug Discov. Technol.,* **16,** 290 (2019).
24. A. Elaissi, Z. Rouis, N. A. Salem, S. Mabrouk, Y. ben Salem, K.B. Salah, M. Aouni, F. Farhat, R. Chemli, F. Harzallah-Skhiri, M. L. Khouja, BMC Complement Altern Med. 2012 Jun 28;12:81. doi: 10.1186/1472-6882-12-81.
25. P. Siramon, Y. Ohtani, *The Journal of Wood Science*, **53,** 498 (2007).
26. J. Silva, W. Abebeb, S. M. Sousa, V. G. Duarte, *Journal of Ethnopharmacol*., **89,** 277 (2003).

Optimized zinc electrode for rechargeable zinc-air batteries

M. Slavova[1,2], B. Abrashev[1]*, E. Mladenova[1], V. Terziev[1], E. Mihaylova-Dimitrova[1], B. Burdin[1], G. Raikova[1]

[1] *Acad. Evgeni Budevski Institute of Electrochemistry and Energy Systems, Bulgarian Academy of Sciences, Acad. G. Bonchev Str., Bl. 10, Sofia 1113, Bulgaria*
[2] *Department Machine Elements, Material Science and Chemistry, Faculty of Transport Management, Todor Kableshkov University of Transport, Sofia, 158 Geo Milev Str., Sofia, Bulgaria*

In this study, two different approaches to improve the zinc anode cyclic stability are discussed: (i) optimization of the active zinc mass composition by adding different metal oxides, which aims to prevent the formation of dendrites and thus to inhibit the degradation processes and (ii) optimization of the current collector by replacing the most commonly applied tinned copper mesh with a galvanized one which aims to prevent the copper dissolution during operation of the battery. Zinc electrodes, prepared by mixing of Zn and ZnO with a binder, were pasted on both sides of the current collector and examined by charge/discharge tests in a half-cell configuration with stainless steel mesh counter electrode and reference reversible hydrogen electrode (RHE) in alkaline electrolyte. The effects of different oxides (Bi_2O_3, In_2O_3, Al_2O_3) addition to the Zn paste and copper mesh galvanization on the electrode performance were evaluated. The results show that additives significantly influence the Zn electrode capacity (about 30% improvement) and the replacement of copper mesh with a galvanized one increases its stability and cyclic efficiency.

Keywords: reversible Zn electrode, ZnO additives, optimized Zn/ZnO paste, current collector

INTRODUCTION

Zinc-air batteries stand as some of the best successfully commercialized primary metal-air batteries [1]. They have been considered to be potentially attractive as power sources for various applications such as electric vehicles and renewable energy sources. Their many advantages include: high energy density, high capacity, and operation in humid environments, aqueous electrolytes with low self-discharge and low-cost materials. In the last decades major efforts have been made especially in the development of alkaline Zn-air batteries [2-5]. However, electrically rechargeable alkaline zinc-air cells still suffer from low efficiency and insufficient cyclability, partially related to anodic passivation of the zinc electrode [6, 7] The challenge for science and industry is the development of rechargeable Zn-air batteries for accumulation of solar energy and peak shaving with load displacement [8].

The main issue for the commercialization of zinc-air batteries is their lifetime (number of discharge/charge cycles) which is related to the degradation of the electrodes during cycling and leads to a rapid decrease of their capacity [9]. Concerning the Zn-electrode, the main reasons for degradation are dissolution of Zn and passivation of the electrode with ZnO. This leads to a rapid decrease in capacity and limits the lifetime of the batteries. For a Zn electrode, zinc particle morphology is of great importance for better interparticle contact and lower internal resistance which improves electrochemical performance [10-12].

Nowadays, Zn electrode in state-of-the-art primary Zn-air batteries consists of tinned copper mesh as current collector [8] and metal Zn electrode with ppm doping levels of In, Bi and Al [13]. Bismuth is used to improve conductivity of the zinc particles [14, 15]. Indium is shown to segregate to grain boundaries of Zn and decrease dendrite formation [16]. The co-doping of both In and Bi was observed to decrease the HER dramatically [17, 18]. Aluminum minimizes the corrosion rate of the Zn electrode and provides more then 50% longer discharging time over pristine zinc in 6 M KOH [19]. The aim of this study is to investigate the effect of: i) addition of various metal oxides (Bi_2O_3, In_2O_3, Al_2O_3) to the initial zinc paste in order to prevent the formation of dendrites and thus, inhibit the degradation processes and ii) replacement of the tinned copper current collector with a galvanized one.

EXPERIMENTAL

The basic Zn anode was prepared from zinc paste made of ZnO (Pharma B-D48230) and Zn (UMICORE 100 BIA) at a ratio of 70/30 wt. %. As a binder a mixture of carboxymethylcellulose (CAS:9004-32-4), polyvinyl alcohol (Chimspectar-EC №209-183-3) and polytetrafluoroethylene

---

* To whom all correspondence should be sent:
E-mail: babrashev@iees.bas.bg

emulsion (Sigma Aldrich – CAS 9002-84-0) was applied. The active Zn mass was deposited on both sides of the current collectors: tinned copper mesh (TCM) and galvanized copper mesh (GCM). After drying in air, the electrodes were pressed at 300 kg.cm^{-2} for 3 min. Before use, the electrodes were covered with alkali-resistant paper and a separator (Zirfon) (AGFA-Zirfon Perl UTP 500). The schematic view of anode construction and a photograph of both, CM and GCM current collectors are presented on Figure 1.

Thus prepared Zn electrode was used as a starting point for electrode behavior and will be further named BL (Baseline) electrode. As the proposed zinc electrode contains an increased amount of ZnO (70 wt.%), the following additives: Bi_2O_3 (0.0113 wt.%), In_2O_3 (0.0238 wt.%) and Al_2O_3 (0.0439 wt.%), commonly used with the Zn powder, were added to the ZnO. After fine homogenization of the initial ZnO powder with the above-mentioned additives, the optimized Zn electrode was obtained by the same procedure as the BL electrode and will be further named BIA.

a)

b)
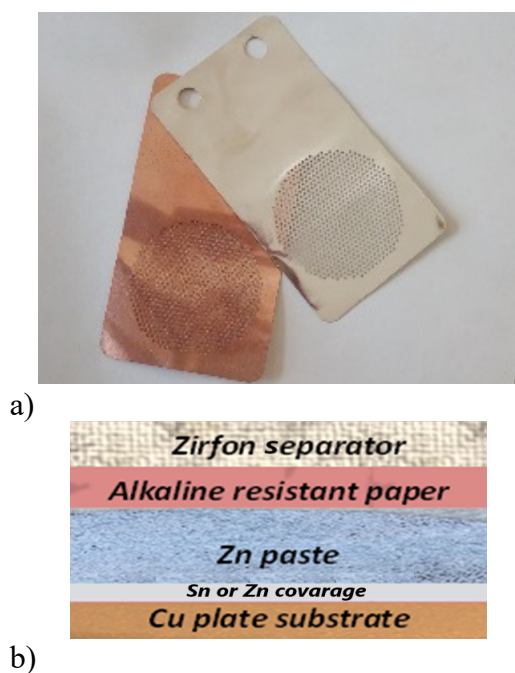
Fig. 1. Zn electrode composition: a) different current collectors, b) schematic view.

The charge/discharge tests were done in a half cell configuration in 6M KOH electrolyte using RHE, HydroFlex (Gaskatel) and stainless-steel counter electrode in a specially designed three-electrode cell with 10 cm^2 working surface area. The electrodes were loaded with $I_{Zn} \pm 15$ mA.cm^{-2} at C_{rate} = C/5. The charge/ discharge potential limit for Zn electrode was chosen -0.6 V and -0.4 V with time of 4:30 and 3:30 hours, respectively.

RESULTS AND DISCUSSION

The first generation of zinc electrodes was made by applying zinc paste to a galvanized copper mesh. Two series of electrodes were fabricated, (1) ZnO without additives (BL), and (2) ZnO with additives (BIA). Considering the bigger initial ZnO quantity a special procedure for reduction of ZnO to Zn was introduced. It involves 3 charge/discharge cycles at very low current densities. An example of BIA electrode activation is given on Figure 2. After activation, both electrodes, BL and BIA stay stable for more than 8 hours operation at C/5 rate, the results are very similar, as it can be seen on Figure 3.
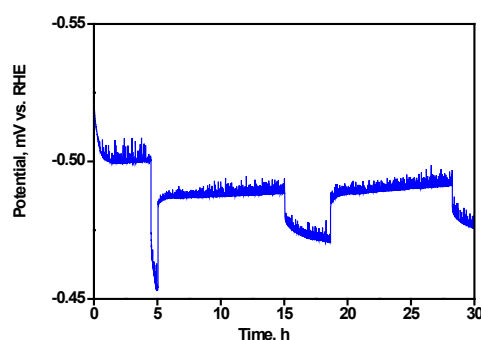

Fig. 2. Zn electrode activation procedure: first charge/discharge cycle at 10 mA.cm^{-2} (C/15 rate) followed by 2 charge/discharge cycles at 5 mA.cm^{-2} (C/10 rate).
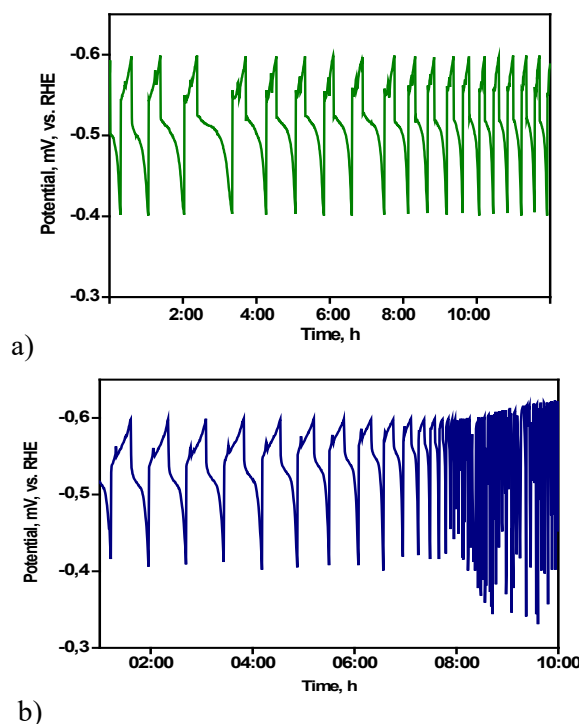

a)

b)

Fig. 3. Charge/discharge cycling tests of the first-generation Zn electrodes BL (a) and BIA (b) with tinned copper mesh (TCM) current collector.
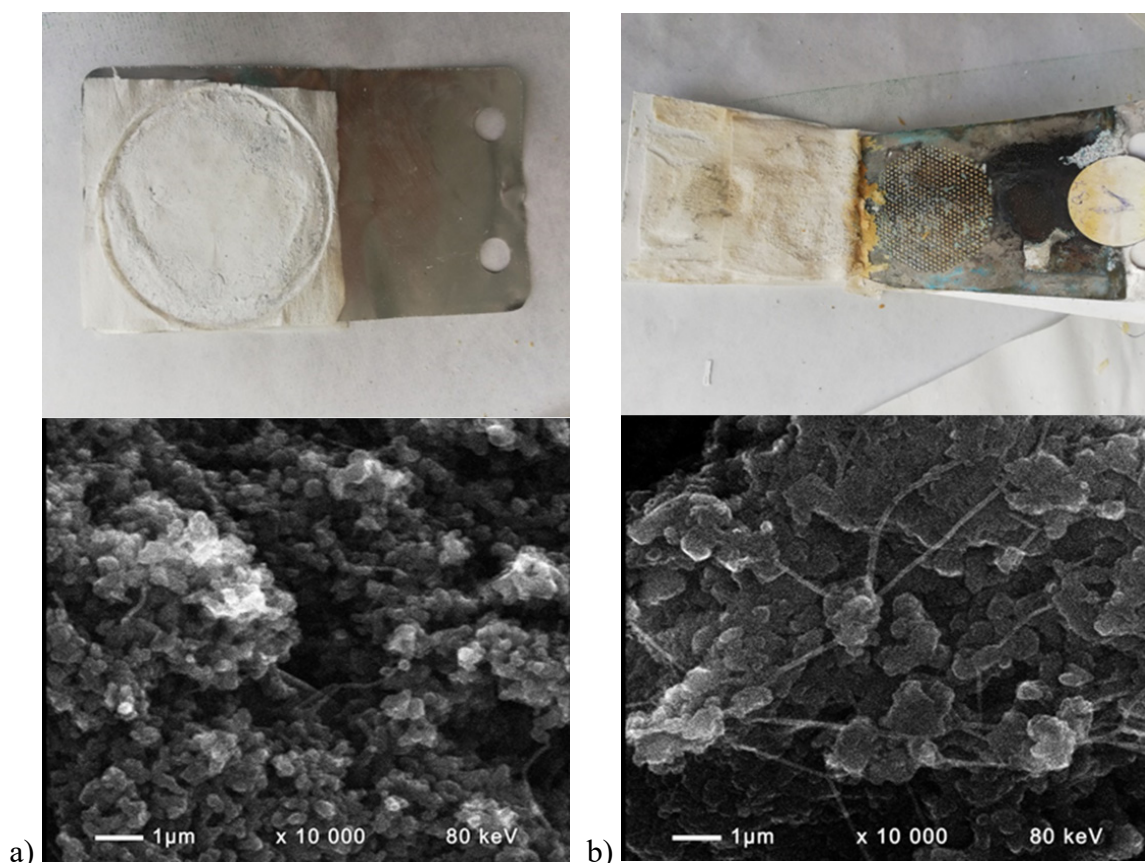
Fig. 4. Photographs and SEM micrographs of the BL electrode with GCM current collector before work (a) and after work (b).
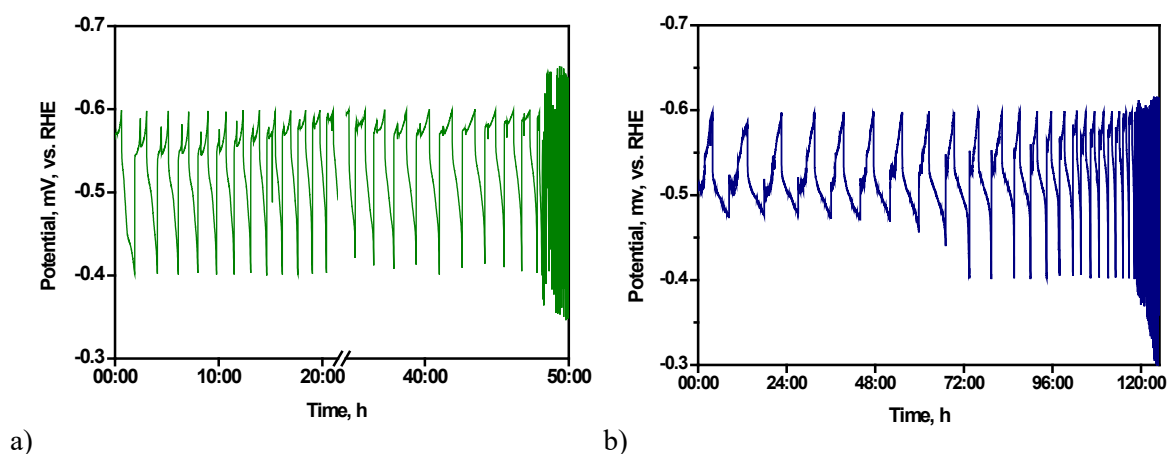

Fig. 5. Charge/discharge cycling tests of the second-generation Zn electrodes BL (a) and BIA (b) with galvanized copper mesh (GCM) current collector.

Obviously, the whole Zn paste fell out from the tinned copper mesh as a result of bad adhesion between the zinc and the tin coating, which leads to total zinc anode destruction. Therefore, the second-generation zinc electrodes were fabricated with replacement of the tinned copper mesh with galvanized cooper mesh. The cycling results are presented on Figure 5. They show a significant increase in the lifetime of the zinc electrode. The BIA electrode (Fig. 5b) operated for more than 115

hours, which is twice as long as the results obtained for BL electrode.

The discharge process in the first 70 hours of operation of the BIA electrode with GCM current collector (Fig. 5b) stops when the time limit is reached. After that the zinc electrode polarization increases and the electrode reaches the set discharge potential limit. The electrode is fully discharged after 115 hours of operation and active zinc mass dissolution is observed (Fig. 6).

50
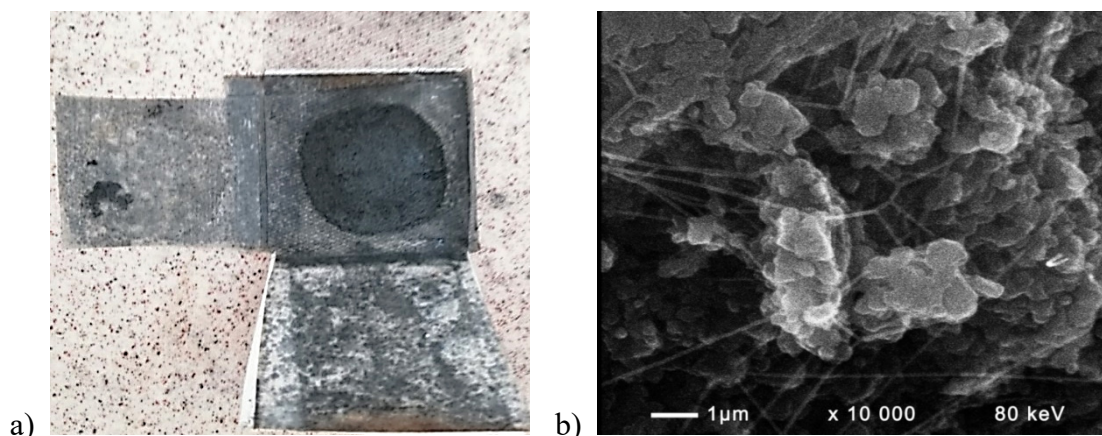
Fig. 6. Photograph (a) and SEM micrograph (b) of the BIA electrode with GCM current collector after work.

The presented *post-mortem* analysis shows the electrode surface after cyclization. The GCM current collector holds a small amount of the active mass, and it is visibly greater than that on the TCM current collector (Fig. 6a, Fig. 4b). The SEM observation (Fig. 6b) does not significantly differ from that of the BL electrode (Fig. 4b), zinc dendrite formation and characteristic polytetrafluoroethylene threads appear.

CONCLUSIONS

The increase in the lifetime of rechargeable zinc–air batteries is a challenge and its overcoming depends on a lot of obstacles, for instance, passivation and corrosion of the zinc anode leading to fast zinc degradation. A complex approach should be used to optimize several directions related to the main breakdown process observed in the original zinc electrode. The method we reported in this study is focused on the improvement of (i) the active zinc mass composition and (ii) the current collector which aims to further enhance the reversibility of the zinc anode. The obtained results showed that the addition of Bi-, In- and Al- oxides to the initial zinc paste, rather than to the ZnO which quantity is twice and half larger (70 wt.%) than the Zn content (30 wt.%), as well as the replacement of copper mesh current collector with a galvanized one, improved the electrochemical behavior of the zinc anode. The additives inhibit the Zn degradation processes and substantially improve the electrode capacity (by about 30%) over a larger number of cycles. More than 115 hours of charge/discharge operation at C/5 rate were achieved with BIA electrode and galvanized copper mesh, which fully meets the requirements for a reversible zinc anode.

REFERENCES

1. A. Kaisheva, in: Portable and Emergency Energy Sources, Z. Stoynov, D. Vladikova (eds.), Marin Drinov Academic Publishing House, Sofia, 2006, p. 301.
2. S. Clark, A. Latz, B. Horstmann, *Batteries*, **4**, 5 (2018), (http://dx.doi.org/10.3390/batteries4010005).
3. J. Zhang, Q. Zhou, Y. Tang, L. Z. Yanguang Li, *Chem. Sci.*, **10**, 8924 (2019).
4. B.Abrashev, D. Uzun, V. Terziev, G. Raikova, K. Petrov, *Bulg. Chem. Commun.*, **5 (**4), 447 (2021).
5. M. Bockelmann, M. Becker, L. Reining, U. Kunz, T. Turek, *Journal of The Electrochemical Society*, **165** (13) A3048 (2018).
6. G. Prentice, Y. C. Chang, X. Shan, *J. Electrochem. Soc.*, **138** (4), 890 (1991).
7. J. Yi, P. Liang, X. Liu, K. Wu, Y. Liu, Y. Wang, Y. Xia, J. Zhang, *Energy Environ. Sci.*, **11**, 3075 (2018).
8. EU funded H2020 project: Zinc-Air Secondary innovative nanotech-based batteries for efficient energy storage– ZAS (GA 646186), (http://sintef.no/projectweb/zas/).
9. Z. B. Stoynov, D. E. Vladikova, B. I. Abrashev, M. P. Slavova, B. G. Burdin, E. S. Mihaylova-Dimitrova, L. C. Colmenares, A. R. Mainar, J. A. Blázquez, *Bulg. Chem. Commun.*, **50** (A), 189 (2018).
10. A. R. Mainar, L. C. Colmenares, J. A. Blázquez, I. Urdampilleta, *Int. J. Energy Res.*, 1 (2017), https://doi.org/10.1002/er.3822.
11. E. Mihaylova-Dimitrova, B. Burdin, E. Mladenova, B. Abrashev, M. Slavova, D. Vladikova, *Nanosciences & Nanotechnology*, **19** (2), 19 (2019).

12. M. B. Lim, T. N. Lambert, E. I. Ruiz, *Journal of The Electrochemical Society*, **167**, 060508 (2020).
13. I. A. J. Strauven, M. L. Meeus, *Patent* CA2153330 A1 (1994).
14. H. S. Kim, Y. N. Jo, W. J. Lee, K. J. Kim, C. W. Lee, *Electroanalysis,* **27**, 2, 517 (2015).
15. M. Schmid, M. Willert-Porada, *Electrochimica Acta*, **260**, 246 (2018), doi.org/10.1016/j.electacta. 2017.12.041.
16. C. W. Lee, K. Sathiyanarayanan, S. W. Eom, H. S. Kim, M. S. Yun, *J. Power Sources,* **159**, 2, 1474 (2006).
17. S. Lysgaard, M. K. Christensen, H. A. Hansen, J. M. García Lastra, P. Norby, T. Vegge, *ChemSusChem*, **11** (12), 1933 (2018), doi:10.1002/cssc.201800225.
18. M. Yano, S. Fujitani, K. Nishio, Y. Akai, M. Kurimura, *J. Power Sources*, **74**, 129 (1998).
19. Y. Li, H. Dai, *Chem. Soc. Rev.*, **43**, 5257-5275, (2014), DOI: 10.1039/C4CS00015C.

Algae-assisted bioelectrochemical system with ammonium, sulfide removal and parallel biomethanation

A. T. Angelov*, S. G. Bratkova, R. V. Ivanov, P. G. Velichkova

Department of Engineering Geoecology, University of Mining and Geology "St. Ivan Rilski", Sofia 1700, Bulgaria

In a two-section bioelectrochemical system (BES), the processes of biomethanation of ethanol stillage in the anode zone and oxygenic photosynthesis in the cathodic zone are combined. There is a reduction of ammonium ions and removal of H_2S in the anode zone, and at the same time, there is a positive impact on the process of biomethanation from ethanol stillage in parallel to the anode anaerobic bioreactor. Chemical oxygen demand (COD) reductions ranging from 71.2% to 89.5% were achieved in the 3 BES operating modes studied. The dynamics of the main technological parameters in the bioanode and biocathode area of the BES during continuous operation of the anaerobic bioreactor and photobioreactor (PBR) at a contact time of 10 days is established. Depending on the selected variant of operation of BES - microbial fuel cell (MFC), microbial electrolysis cell (MEC) with 0.6V and 0.9V, a decrease in the ammonium concentration is found to varying degrees, as in the MEC mode with an external electrical voltage of 0.9V the highest degree of 76.5% is reached. At the same time, complete removal of H_2S is found, in the liquid and gas phases in MEC - mode and partially (78 – 84 %) in MFC -mode. The influence of the photosynthetic phases on the electrochemical parameters of MFC was also investigated, with maximum values for power and current densities of 29 W/m^2 and 115 mA/m^2, respectively.

Keywords: biomethanation, bioelectrochemical systems, aerobic photosynthesis, microalgae, microbial sulfate reduction, ethanol stillage, ammonium and sulfide removal.

INTRODUCTION

Environmental issues related to the use of carbon-based fossil fuels and their depletion determine the important role of renewable energy sources in the development of modern civilization [1].

Ethanol stillage is one of the generated waste streams from the brewing industry, with a high risk of pollution of surface water. They are characterized by high acidity (pH: 3.5–4), high organic content (COD: 50÷150 g/L), and nitrogen compounds and sulfates are often found in significant quantities [2]. The formed wastewater from ethanol stillage is difficult to treat, not only because of its characteristics, but also because of its significant volume [3]. On the other hand, the ethanol stillage is successfully utilized in the process of biomethanation [4], but its high sulfate concentrations may make difficult the further treatment of these waters. During anaerobic digestion, sulfates are converted into more toxic sulfides. In general, process inhibition by sulfides does not occur when the ratio COD/SO_4^{2-} in the effluent is > 10 g/g. The inhibition of anaerobic digestion is strong when the ratio COD/SO_4^{2-} is < 0.5 g/g [3].

Ammonium ions in high concentrations also negatively affect biomethanation [5]. Inhibition by ammonium ions can cause more than 30 % loss of methane potential in biogas reactors digesting protein-rich substrates [6]. To alleviate ammonia inhibition, different approaches are applied, but most of them are expensive and of limited application [7].

Anaerobic digestion has established itself as a baseline process for the conversion of organic waste into biogas and is a sustainable approach to its treatment [8]. However, further optimization of anaerobic digestion is limited by insufficient energy recovery and accumulation of inhibitory substances in the medium [9].

In recent years, bioelectrochemical systems (BESs) have proven to be systems that provide attractive opportunities for water treatment from organic and inorganic pollutants, electricity generation, biohydrogen production, bioelectromethanogenesis, preparation of valuable chemical products, application in biosensors for detection of various pollutants in the aquatic environment, etc. [10].

The BESs also offer further possibilities to improve the anaerobic digestion process - as an after-treatment step for the treatment of the undigested organics (by microbial fuel cell - MFC) in the output stream for further oxidation of the organics with the accompanying energy recovery, and/or bioelectromethanation (by microbial electrolysis cell - MEC) which can be achieved – increasing the methane content in the biogas at the expense of CO_2, overall stabilization of the process, reducing COD at the output, etc. [11].

An advantage of using BES is the additional possibility of removing the sulfides and hydrogen sulfide formed in the medium in the parallel (with biomethanation) process of microbial sulfate reduction. The produced biogenic H_2S is a mediator in electron transfer, being oxidized on the surface of the anode to elemental sulfur (S^0) and its other forms [12].

The use of algae in microbial fuel cells is of interest due to the possibility of obtaining biomass, energy yield and wastewater treatment for various pollutants [13]. Furthermore, algae-assisted MFCs provide a new, efficient and cost-effective solution to increase the oxygen concentration in the cathodic zone [14], and oxygen is the preferred electron acceptor in the cathode chamber of BES. In a significant part of the previous research, algae are used as biocatalysts in the cathode zone primarily in microbial fuel cells [15]. However, research on the application of algae as a biocatalyst in microbial electrolysis cells is lacking in this regard. The expectation is that applying of additional external voltage (in algae-assisted MEC), will significantly increase the current and power density of the BES and thus achieve a higher rate of pollutant removal in the anode area.

A major objective of the research is to establish the possibility of using algae-assisted BES (in the cathode zone) in combination with biomethanation (in the anode zone), to achieve a higher rate of organic substrate utilization, removal of sulfur and nitrogen compounds, and improve the biomethanation process. An important task in research is to compare two variants of algae-assisted BES – MFC and MEC, in terms of removal of ammonium ions, H_2S, COD and influence on the biomethanation process.

MATERIALS AND METHODS

Substrates, inoculum and enrichment of microbial communities

For the laboratory studies a mixed culture of microalgae dominated by *Scenedesmus sp.*, isolated from natural water sources, was used. For the cultivation of the microalgae, the modified culture medium BG11 was used, according to previous studies [16] with the following composition for 1 L – 1.5 g $NaNO_3$, 0.5 g Na_2CO_3, 0.04 g K_2HPO_4, 0.075 g $MgSO_4.7H_2O$, 0.036 g $CaCl_2.2H_2O$, 0.045 g citric acid, 0.0015 g ferric ammonium citrate, 0.045 g EDTA (disodium salt) and 1 ml trace elements solution consisting of 2.86 g/l H_3BO_3; 1.81 g/l $MnCl_2.4H_2O$; 0.222 g/l $ZnSO_4.7H_2O$; 0.39 g/l $NaMoO_4.2H_2O$; 0.079 g/l $CuSO_4.5H_2O$; 0.0494 g/l $Co(NO_3)_2.6H_2O$. The amount of microalgae

inoculum was approximately 10 % of the working volume (2.0 dm^3) of the photobioreactor. Cultivation of the microalgae was carried out at room temperature in the range of 24-26 ºC. The oxygenic photosynthesis zone in the combined photobioreactor with the cathode zone of the BES (3) was suspended with air (1.0 dm^3/60s) without further addition of CO_2 (Fig. 1).

The composition of the substrate used (ethanol stillage) for biomethanation in the UASB reactor and the anode zone of the BES is with approximately the same composition under the different operating modes investigated.

Typically, the ethanol stillage is characterized by a high organic load of up to 85-1 10 g/l COD [17], and anaerobic digestion has been found to proceed more steadily at initial COD values below 50 g/l [18].

For the biomethanation process, ethanol stillage from a winery in the village of Svetovrachene, Bulgaria, was used, which was stored in a refrigerator at a temperature of 4 °C. Before being used, the stillage was neutralized to pH 7.5 with NaOH and diluted 4 times. The anaerobic activated sludge was taken from a municipal wastewater treatment plant in Sofia, Bulgaria and was used for inoculation with methanogens. Table 1 shows the main characteristics of the substrate used – ethanol stillage (neutralized and diluted four times).

Table 1. Main characteristics of the ethanol stillage feeding the anaerobic reactor

Parameter	Value
pH	7.4-7.6
COD, g/L	9.45-11.90
SO_4^{2-}, mg/L	163-198
Total Kjeldahl nitrogen (TKN), mg/L	310-325
Dry matter, %	1.67-1.89

Description of laboratory installation

A scheme of the laboratory installation of an integrated bioelectrochemical system (BES) to a UASB (Upflow Anaerobic Sludge Blanket) reactor is shown in Fig. 1. The proposed construction is a combined column photobioreactor (PBR) with a bioelectrochemical system (BES) integrated into its volume. The combined BES-PBR system is in 2 cylindrical plexiglass volumes, "tube-in-tube" type, with the cathode zone having a volume of 2.0 dm^3 (height 400 mm, diameter 100 mm) and the anode zone being an opaque plastic inner tube with a volume of 0.65 dm^3 (height 400 mm, diameter 45 mm). In the volume of the cathode zone (PBR), 4 LED light sources with a wavelength in the range of 400÷700 nm are placed, which provide a light flow

54

with an intensity in the range of 7600 - 8500 Lx, in the mode - 12h light: 12h dark.

For the anode and cathode in the BES, 2 identical graphite rods with a diameter of 8 mm and a length of 300 mm were used. A cation exchange membrane (CEM), type CMI-7000S (Membrane International Inc.), with an internal diameter of 45 mm, separated the cathode from the anode zones of the BES. In the zone of oxygenic photosynthesis (cathode zone), the possibility of air supply is provided by a pump with a flow rate of $1.0 \ dm^3/60$ s. On the other hand, in the anode area, the possibility of recirculating organic substrate from the UASB – bioreactor for biogas production is ensured by a peristaltic pump with a flow rate of $5 \ dm^3/h$.

The anaerobic UASB biomethanation bioreactor with a geometric volume of $4 \ dm^3$ and a working volume of $3.0 \ dm^3$ was connected to the anode zone of the BES (volume $0.65 \ dm^3$), the liquid phase being continuously recirculated by a peristaltic pump with a flow rate of $5 \ dm^3/h$. The temperature in the bioreactor was maintained in the range of 33-35 ºC by an adjustable electric heater placed at the bottom of the vessel. The incoming substrate (8) is dosed into the reactor at a flow rate of 0.300 $dm^3/24h$, which provides a contact time of 10 days.

The photobioreactor (resp. the cathode zone of the BES), was daily fed with fresh nutrient medium (BG11) by a peristaltic pump (2) at a flow rate of 200 $dm^3/24h$, during which a contact time of 10 days was achieved, consistent with the exponential phase of the microalgae growth curve established below.

Analytical methods

The volume of the separated gas was measured using a MilliGascounter "Ritter MGC-1", and the content of CO_2, CH_4, O_2, H_2S and H_2 in the biogas was determined using a portable gas analyzer "Draeger X-am 7000". At various points in the laboratory installation continuous (online) measurement of dissolved oxygen, pH, voltage, electrical conductivity, temperature and illumination is provided by using Vernier[R] BTA sensors and visualization and recording of data through the interface LabQuest[R]. The dry matter of the stillage was measured using a Kern DAB moisture analyzer balance.

Chemical oxygen demand (COD) was measured with Merck reagents according to APHA (1992) [19]. pH and ORP were measured with a pH/ORP-meter Hanna HI 3220. Sulfate concentration was determined using a spectrophotometric method at λ - 420 nm, using $BaCl_2$ reagent. The concentration of hydrogen sulfide in the liquid phase was measured using Nanocolor test 1-88/05.09 at λ of 620 nm. The concentration of ammonium ions (NH_4^+-N) in the catholyte was determined spectrophotometrically by DR 6000, Nessler Method, Ammonia, 380N HACH.

A Bürker light microscope counting chamber (Boeco[R], BM-800) was used to determine the number of microalgae, as well as a parallel determination of the optical density of the cell suspension during the cultivation of the microalgae at a wavelength of 650 nm and a red filter. Scanning electron microscopy (SEM) was used for scanning the biofilm on the surface of the anode. Before SEM, the samples were fixed with 2 % glutaraldehyde in 0.1 M phosphate buffer overnight in the fridge (4 ºC) and then dried with ethanol. After that, the samples were kept in a desiccator for 48 hours and then coated with a thin layer of graphite.

BES operations and electrochemical analysis

Under the continuous operation of the anaerobic UASB reactor and the photobioreactor (PBR), 4 BES operating modes were investigated (Fig. 1). The first mode is when the electrical circuit of the BES is open (no load between anode and cathode). The second mode is when the BES is operated as a microbial fuel cell (MFC), where a load of 250 Ω is applied, found (below) to be optimal for achieving maximum power density. The third and fourth mode is when the BES is operating as a microbial electrolysis cell (MEC), with the application between the electrodes of 2 different external voltages of 0.6V and 0.9V and a load resistance of 10 Ω.

The electrical parameters of the BES were measured with a Keithley 175 digital multimeter, and a precision potentiometer with a maximum value of 11 kΩ was used for the load resistance. To provide an external voltage source, a stabilized adjustable rectifier type PS-3005D was used when operating BES in MEC mode. The maximum power value, Pmax, was established by constructing polarization curves. The current and power density was calculated based on the geometric area of the electrodes in the anode/cathode chambers and the voltage across the load resistors (R1/R2).
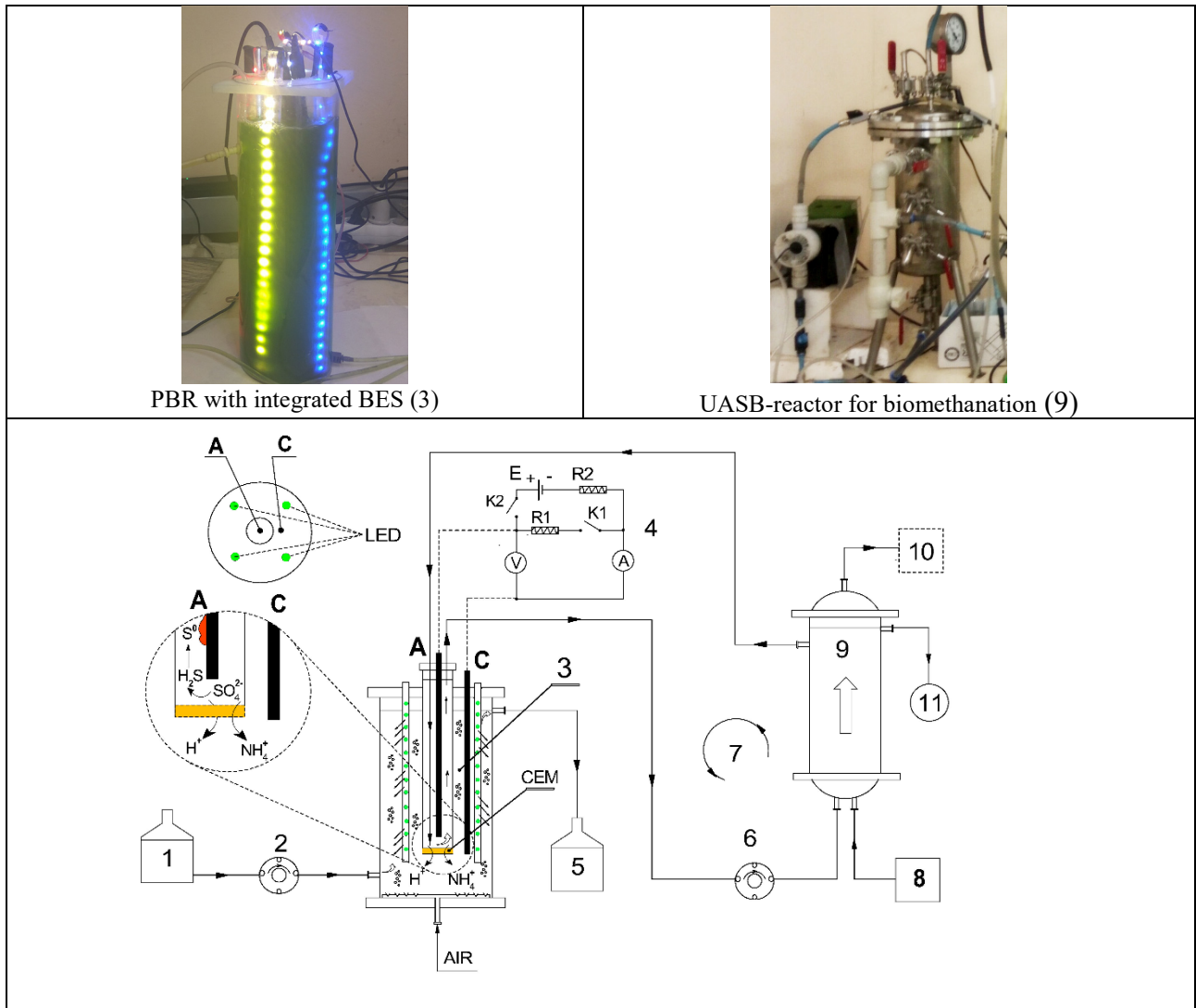
PBR with integrated BES (3)

UASB-reactor for biomethanation (9)

Fig. 1. Scheme of the laboratory installation. 1- input nutrient media for microalgae, 2- dosing peristaltic pump, 3 - integrated BES with a cathodic zone with oxygenic photosynthesis (PBR) and anodic zone with recirculation of substrate for biomethanation, 4- loading circuit of BES, 5- output of PBR (cathodic zone of BES), 6-pump for recirculation between the anode zone of the BES and UASB-reactor for biomethanation, 7-recirculation loop of the anode zone, 8- substrate inlet for biomethanation, 9- UASB-reactor for biomethanation, 10- biogas, 11- outlet spent substrate after AD.

a

b
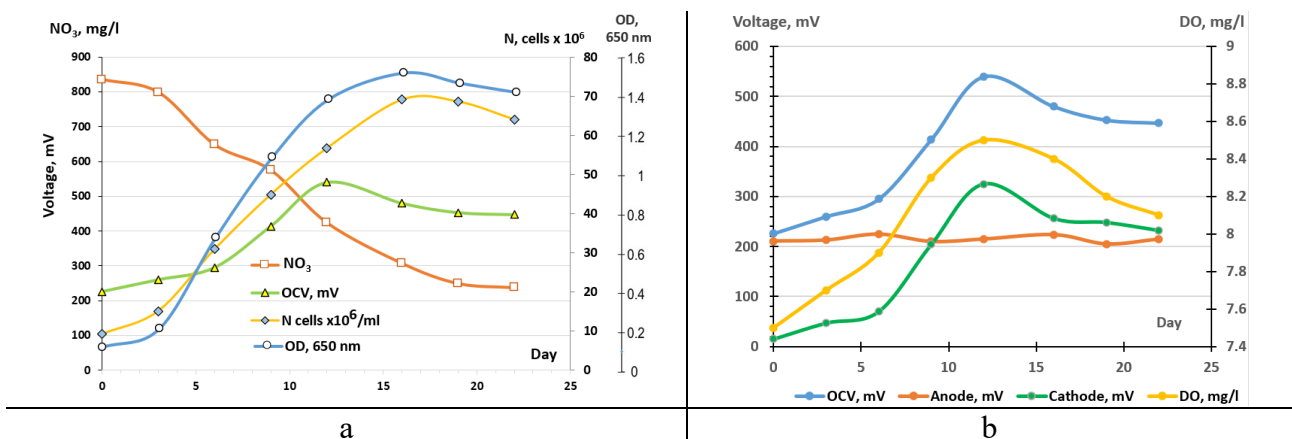
Fig. 2. Dynamics of nitrate concentration (a), anodic and cathodic potential (b), dissolved oxygen (b) and OCV (b), during the growth phases of algae in the cathodic zone of BES (a).

RESULTS AND DISCUSSION

Cultivation of microalgae and influence of BES electrochemical performance

Initially, to study the influence of microalgae as biocatalysts in the cathode zone, stationary conditions for the biomethanation process were previously established in the contour of the anode zone of the combined BES-PBR system (7). A contact time of 10 days was provided for the feed organic substrate in the UASB reactor (Fig. 1) and stabilization of the process with the uniform release of biogas from 0.92 to 0.94 dm^3/24h (Table 3).

To establish the growth curve of microalgae in the cathode zone of the BES (resp. PBR), in parallel with the measured optical density, the number of microalgae was also determined using a Bürker counting chamber. Cultivation of the microalgae continued for a period of 25 days. Periodically (every 3 days) samples were taken from the culture suspension to determine the number of cells and the optical density (OD). The obtained results (Fig. 2a) show that the stationary phase was reached in about 15 days, with the log phase of growth lasting between 4 and 12 days from the beginning of cultivation. Simultaneously with the growth curve, the nitrate concentration and open circuit voltage (OCV) in the BES were measured in parallel (Fig. 2a). A significant decrease in the nitrate concentration in the medium from 835 mg/l to 238 mg/l over a period of 22 days was found, which is expected given that nitrate is a major food source for microalgae. The highest value of the open circuit voltage (OCV= 540 mV) of the BES was measured at 12 days, which corresponds to the end of the exponential phase of the development of the mixed culture microalgae dominated by *Scenedesmus sp.* Because the anodic potential throughout the period was fairly constant (203 ÷ 224 mV, Fig. 2b), the rise in the OCV value in the BES is obviously due to the growth of the cathodic potential. The reason for this is the increase in the oxygen concentration (from 7.5 to 8.5 mg/l) in the cathode zone due to the development of algae at the end of the log phase (Fig. 2b). Similar results were obtained by Hou *et al.* (2016), who also found a direct relationship between dissolved oxygen concentration in the catholyte and OCV [20].

Also of interest is the establishment of the influence of the phases of photosynthesis of oxygenic microalgae on the bioelectrochemical characteristics of BES. For this purpose, during the period of the log-growth phase (10th day), the power curves and polarization curves of the BES in the mode of operation as MFC were lowered (Fig. 3). In these measurements, the highest values of power and current density were found during the light phase, respectively - 29.0 W/m^2 and 115 mA/m^2 and during the dark phase, respectively -22.6 W/m^2 and 112 mA/m^2. These values were obtained with a load resistance value of – R1 (Fig. 1) in the range of 200-300. The obtained results confirm again the influence of higher oxygen concentrations during the light phase (compared to the dark phase) on the bioelectrochemical characteristics of algae-assisted BES, with analogous data being commented on and observed in other studies [20, 21].
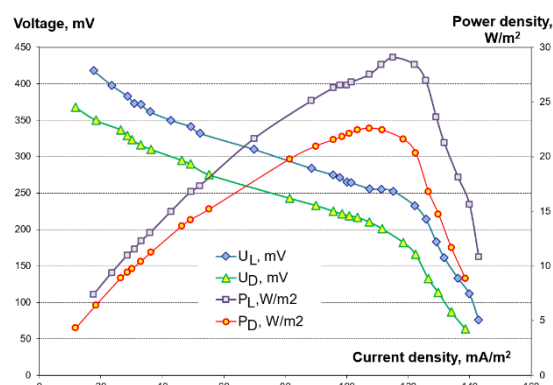

Fig. 3. Power curves and polarization curves measured through the light and dark phases of photosynthesis in the cathodic zone of the BES, during the log-phase (10th day) of the algal development. P$_D$ and P$_L$, U$_D$ and U$_L$ - power density and voltage through the light (L) and dark (D) phases.

Ammonium, sulfide and COD removal from ethanol stillage by BES system

Along with the process of biomethanation from various organic substrates (including ethanol stillage), a parallel process of ammonification takes place, which breaks down the present proteins, urea and amino acids. This process produces ammonia (NH$_3$), which is rapidly converted to free ammonium ions (NH$_4^+$). They are an important source of nutrients for microorganisms and provide buffering capacity in anaerobic digestion processes. The protein degradation process is slow and the released ammonia tends to accumulate in the medium [22]. However, substrates with high nitrogen contents inhibit the process, which can lead to reduced biogas quality and quantity [6].

The integration of the anode zone of the BES to the AD process is one of the approaches to eliminate high concentrations of ammonium ions by their migration through the CEM into the cathodic zone. In the present study, their concentration in the anode zone drops significantly (from the initial value 141÷180 mg/l), and in the cathodic zone, they also decrease, probably due to their absorption by

microalgae and a parallel process of nitrification (Table 2). The removal of ammonium ions in the anode zone (Fig. 4 and Table 2), is most established in the mode of operation - MEC with an external voltage of 0.9 V, reaching up to 25 mg/l (76.5 %), followed by MEC with 0. 6 V – 84 mg/l (53.3 %) and least in MFC mode - up to 105 mg/l (41.7 %). Besides the removal of ammonium ions, there was also a substantial decrease in COD for the 4 modes of operation studied, each characterized by a different current density in the BES. The impact of BES on the COD lowering in the anode zone was significant, with an average current density of 0.34 A/m^2 (for MEC$_{0.9V}$) reaching to 89.5%, respectively, at an average current density of 0.13 A/m^2 (for MEC$_{0.6V}$) - 80.4% and at a current density of 0.05 A/m^2 (for MFC) – 71.2 % (Fig. 4). For comparison, in the mode of operation without BES, the COD reduction in the system is in the range of 45÷55 %. Similar results were obtained by Zhang *et al.* (2019), where when treating swine wastewater in the anode chamber of MFC (a combined system with a photosynthesis process in the cathodic zone with *Chlorella vulgaris*), 85.6 % ammonium removal and up to 83.1 % reduction in total organic carbon (TOC)

were reached in 24 days [21]. The presence of high concentrations of sulfates in the organic substrate subject to anaerobic digestion makes the biomethanation process difficult. Methanogens under these conditions compete with sulfate-reducing bacteria (SRBs) for the carbon source, and the H$_2$S produced, in addition to being corrosive and toxic, also has an inhibitory effect on AD and degrades biogas [23].

By introducing the BES process-based heterotrophic microbial sulfate reduction in the anodic zone, it is possible to realize oxidation on the anode surface of biogenic H$_2$S to elemental sulfur (and other forms - Fig. 1) and thus, one can reduce the H$_2$S content in the medium and improve the composition of the obtained biogas [24]. The studies found complete removal (100 %) of H$_2$S in the gas phase (Table 3) in both MEC modes and a significant decrease (78-84 %) in MFC mode. About the liquid phase (Table 2), complete removal of H$_2$S and sulfates was also observed in MEC mode with 0.9V external voltage and partly in MFC mode with up to 70 % concerning sulfates and up to 45.3 % reduction of dissolved H$_2$S.
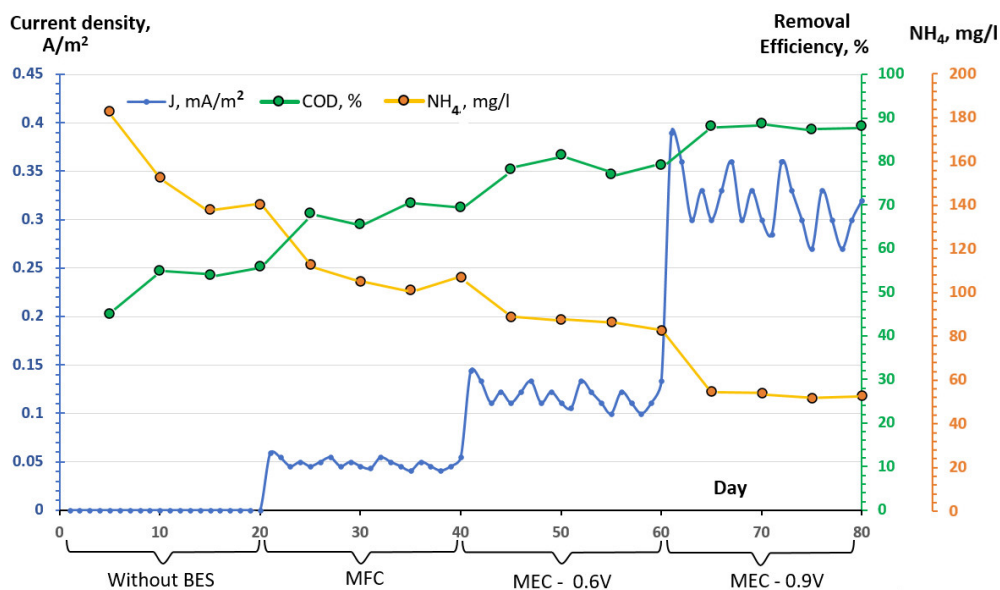

Fig. 4. Dynamics of COD and ammonium ion concentration in the anode chamber, at different current densities, for 4 modes of operation of BES.

Table 2. Main parameters of the liquid phase in the anode zone at 4 modes of the BES.

Parameter	Without BES	MFC	MEC with 0.6V	MEC with 0. 9V
pH	7.4 - 7.8	7.6-8.0	7.7 - 8.1	7.8 - 8.2
COD input, g/L	9.88 – 11.55	9.45 – 11.61	10.20 – 11.90	10.15 – 11.80
COD (anode), g/L	5.48 - 6.69	2.98- 3.67	2.14- 2.49	1.20- 1.40
NH$_4$$^+$(anode), mg/L	141-180	105-116	84-90	25-28
NH$_4$$^+$(cathode), mg/L	3- 7	10- 15	17- 25	27- 35
SO$_4$$^{2-}$, mg/L	144. 3	43. 2	<1	<1
H$_2$S (in liquid), mg/L	22.5- 21. 6	15.4- 12. 3	5.3- 4. 1	<1

Table 3. Main parameters of the biogas released from the UASB reactor in 4 modes of BES.

Parameter	Without BES	MFC	MEC with 0.6V	MEC with 0. 9V
Daily biogas yield, $dm^3/24h$	0.91-0.93	0.88 – 0.92	0.89- 0.91	0.87-0.90
CH_4, %	59-61	69-71	72-74	72-75
CO_2, %	21-24	18-20	17-19	16-18
H_2S, %	0.041- 0.044	0.009- 0.007	0	0
H_2, %	0.9- 1.0	0.42- 0.45	0.34- 0.37	0

In these results, it is also important to note the pH change during the investigated BES modes (Table 2). In this respect, a slight increase in the pH value is noticeable, the process stabilizing in the range pH = 7.8-8.2 in the $MEC_{0.9V}$ mode. In this regard, the distribution of sulfur forms at different pH values of the environment is known, where under reducing conditions, sulfur can be present in the form of H_2S (gas), HS^- and polysulfides [25]. Therefore, at such pH values, it is logical to expect hydrogen sulfide in the liquid phase to be represented mainly in the form of HS^- - ion.

The integration of algae-assisted BES to AD at the same time leads to an improvement of the quantitative and qualitative composition of the obtained biogas compared to a standalone AD process (Table 3). For example, the daily biogas yield for the entire period (of 80 days) of the experiment was relatively uniform and ranged from 0.88 to 0.93 $dm^3/24h$ in all studied variants, and in terms of qualitative composition – an increase of the CH_4 content to 72-75 % was found in MEC mode with 0.9V, and for comparison in a standalone AD process, CH_4 reaches 59-61 %. The complete removal of H_2S from the biogas when operating BES in the mode of MEC is not to be underestimated.

Fig. 5a shows photographs of SEM images of methanogenic bacteria attached to the surface of the graphite anode. The image shows the colonization of mostly coccoid bacteria measuring 1-1.5 μm. In the cathode zone (Fig. 5b) the culture suspension of microalgae was studied with a light microscope, where a mixed culture of microalgae dominated by *Scenedesmus sp*. with a cell size of 8- 12 μm was observed. The observations were made at the end of the 80 days of the experiments carried out in BES operation mode as MEC with 0. 9V external voltage.

CONCLUSION

In the present study, the possibility of using algae-assisted BES in combination with a biomethanation process was demonstrated to achieve a higher degree of utilization of the organic substrate (ethanol stillage), removal of sulfur compounds and ammonium ions and improvement of the composition of biogas.
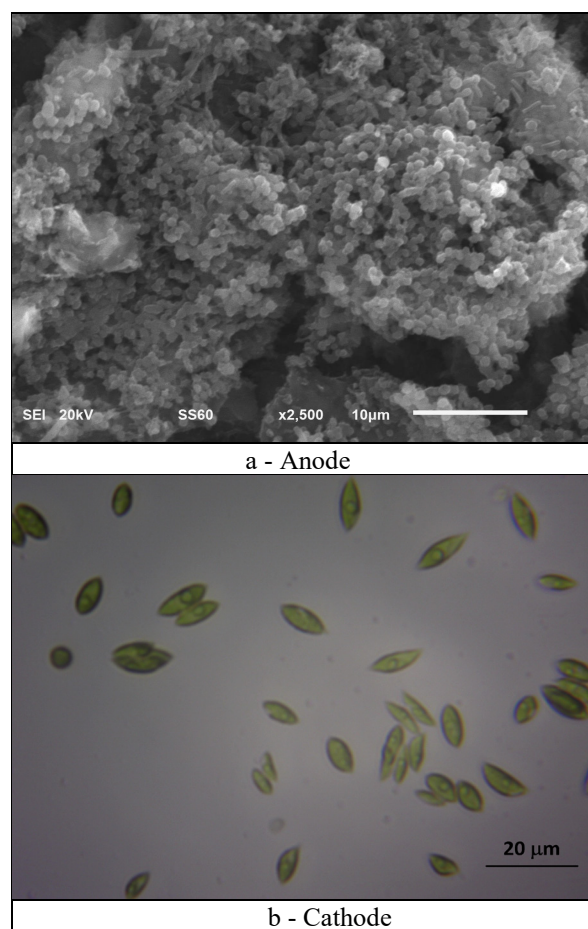

a - Anode

b - Cathode

Fig. 5. Morphological characteristics of attached on the anodic surface (Fig.5a) methanogens (by SEM) and light microscope image (Fig.5b) of a culture suspension of microalgae dominated by *Scenedesmus sp.*

The dynamics of the main technological parameters in the bioanode and biocathode area of the BES during continuous operation of the UASB reactor and photobioreactor (PBR) with a contact time of 10 days were determined. When comparing 4 different operating modes of the combined algae-assisted BES-AD system - without BES, MFC, MEC (0.6V) and MEC (0.9V), the highest removal rates of ammonium ions (76.5 %), H_2S (100 %) and COD (89.5 %) were found at $MEC_{0.9V}$ mode. The

qualitative composition of the obtained biogas was also improved, reaching up to 75 % CH$_4$ content. The influence of the phases of photosynthesis on the electrochemical parameters of BES was also established, with maximum values for power density and current, respectively - 29 W/m^2 and 115 mA/m^2.

REFERENCES

1. C. Olson, F. Lenzmann, *MRS Energy & Sustainability,* **3,** 1 (2016). doi: 10.1557/mre.2016.7

2. W. Mikucka, M. Zielińska, *Applied Biochemistry and Biotechnology,* **192***,* 770 (2020). doi:10.1007/s12010-020-03343-5

3. A. Vlyssides, E. M. Barampouti, S. Mai, A. Stamatoglou, E. Tsimas. *Water Science and Technology*, **62**(12), 2899 (2010). doi:10.2166/wst.2010.647.

4. L. Gyenge, R. Botond, S. Raduly, C. Crognale, S. Crognale, B. Ábrahám, *Environmental Engineering and Management Journal*, **17**(5), 1021 (2018), doi:10.30638/eemj.2018.101

5. K. Taeyoung, A. Junyeong, J. J. Kyung, I. S. Chang, *Bioresource Technology, S0960852415007956* (2015)*.* doi: 10.1016/j.biortech.2015.06.009

6. I. A. Fotidis, H. Wang, N. R. Fiedel, L. Gang, D. B. Karakashev, I. Angelidaki, *Environmental Science & Technology,* **48**(13), 7669 (2014). doi:10.1021/es5017075

7. H Tian, E. Mancini, L. Treu, I. Angelidaki, I. A. Fotidis, *Chemosphere,* **231**, 415 (2019) https://doi.org/10.1016/j.chemosphere.2019.05.140

8. R. Yuanyuan, M. Yu, C. Wu, Q. Wang, M. Gao, Q. Huang, Y. Liu. *Bioresource Technology*, **247**, 1069 (2018) ISSN 0960-8524, https://doi.org/10.1016/j.biortech.2017.09.109.

9. R. K. Bennett, L. M. Steinberg, W. Chen, E. T. Papoutsakis, *Current Opinion in Biotechnology,* **50**, 81 (2018) ISSN 0958-1669, doi:10.1016/j.copbio.2017.11.010.

10. L. Rathinavel, D. Jothinathan, V. Sivasankar, P. Agastian, P. Mylsamy, *Microbial Fuel Cell Technology for Bioelectricity,* **81**, 116. (2018). doi:10.1007/978-3-319-92904-0_5

11. H. Gao, Y. D. Scherson, G. F. Wells, *Environ. Sci. Process. Impacts,* **16**, 1223 (2014).doi: 10.1039/c4em00069b

12. N. Eaktasang, H. S. Min, C. Kang, et al., *Bioprocess Biosyst. Eng.,* **36**, 1417 (2013). https://doi.org/10.1007/s00449-012-0881-3

13. A. González del Campo, P. Cañizares, M. A. Rodrigo, F. J. Fernández, J. Lobato, *Journal of Power Sources*, **242**, 638 (2013). doi: 10.1016/j.jpowsour.2013.05.110

14. R. Kakarla, J. R. Kim, B.-H. Jeon, B. Min, *Bioresource Technology*, **195**, 210 (2015)*.* doi: 10.1016/j.biortech.2015.06.

15. R. G. Saratale, C. Kuppam, A. Mudhoo, G. D. Saratale, S. Periyasamy, G. Zhen, G. Kumar. *Chemosphere,* **177***,* 35–43. (2017). doi: 10.1016/j.chemosphere.2017.02.132.

16. A. Angelov, S. Bratkova, P. Velichkova*. Journal of Chemical Technology and Metallurgy*, **56** (4), 796 (2021)

17. K. Sankaran, M. Premalatha, M. Vijayasekaran, V. Somasundaram, *Renewable and Sustainable Energy Reviews,* **37***,* 634 (2014). doi: 10.1016/j.rser.2014.05.062

18. B. Wolmarans, G. H. De Villiers, *Water SA,* **28**(1), 63. (2004). doi:10.4314/wsa. v28i1.4869

19. APHA, WPCF, AWWA, Standard methods for examination of water and wastewater, 18th edn., Washington: American Public Health Association, 1992.

20. Q. Hou, H. Pei, W. Hu, L. Jiang, Z. Yu, *Bioresource Technology,* **203**, 50 (2016). doi: 10.1016/j.biortech.2015.12.049.

21. Y. Zhang, Y. Zhao, M. Zhou, *Environmental Science and Pollution Research,* **26***,* 6182 (2019). doi:10.1007/s11356-018-3960-4.

22. N. Krakat, B. Demirel, R. Anjum, D. Dietz. *Water Science and Technology*, **76** (8), 1925 (2017). doi:10.2166/wst.2017.406.

23. X. J. Xu, C. Chen, A. J. Wang, N. Fang, Y. Yuan, N. Q. Ren, D. J. Lee, *Bioresource Technology*, **116**, 517 (2012). doi:10.1016/j.biortech.2012.03.095

24. K. Rabaey, K. Van de Sompel, L. Maignien, N. Boon, P. Aelterman, P. Clauwaert et al. *Environmental Science & Technology,* **40**(17), 5218 (2006). doi:10.1021/es060382u.

25. V. Beschkov, E. Razkazova-Velkova, M. Martinov, S. Stefanov, *Appl. Sci*., **8**(10), 1926 (2018) https://doi.org/10.3390/app8101926

Gas diffusion electrodes (GDEs) with Ag/γ-MnO$_2$ bimetallic catalytic composition for metal hydride/air batteries

B. Abrashev*, V. Terziev, D. Paskalev, E. Lefterova, M. Dimitrova, O. Dimitrov, A. Gigova, K. Petrov

Acad. E. Budevski Institute of Electrochemistry and Energy Systems, Bulgarian Academy of Sciences, Acad. G. Bonchev Str., Bl. 10, 1113 Sofia, Bulgaria

The gas diffusion electrode (GDE) consists of a carbon-based gas diffusion layer (GDL) and an active layer (AL). In this study GDE with bimetallic AL containing Ag/γ-MnO$_2$ was investigated and compared with previously optimized GDE with Ag/Co$_3$O$_4$ composition. The catalytic structure was created by depositing of a mixture of catalysts containing γ-MnO$_2$ and Ag with a weight ratio between the two components of 1:1. The prepared electrodes were examined before and after work by XRD phase analysis. The morphology of the above-studied ALs and GDL was investigated with scanning electron microscopy (SEM) and BET analysis, respectively. The polarization, charge/discharge tests and impedance analysis were carried out in a half-cell configuration in 6M KOH. Long-term tests of the two GDEs showed good mechanical and electrochemical stability of over 300-500 charge/discharge cycles.

Keywords: gas diffusion electrode, bimetallic catalyst, carbon-based electrodes

INTRODUCTION

The rise in the price of electricity affects both the quality of life and the development of every sphere of the global economy. Furthermore, the constant growing need for energy in order to meet the increasing demand leads to environmental concerns. A transition to clean energy sources/renewable energy sources (RES) could help reduce the reliance on fossil fuels but in that case energy storage arises as a potential challenge for sustainability due to their intermittent character [1]. There is quite a variety of solutions for rechargeable batteries to store and release high amounts of energy in a short time when required such as: metal/air [2-4], nickel/metal hydride [5], etc. For instance, rechargeable metal hydride (MH)/air batteries are envisaged as very promising battery systems with long cycle life, possessing a high capacity. They are very appropriate for stationary applications – one of which is storing energy from RES. Another advantage of metal hydride/air systems is that they can operate in an open-air atmosphere and strong alkaline media [6-8]. A key matter in this type of batteries is the development of the bifunctional GDE which is responsible for both the oxygen reduction reaction (ORR, discharge process) and the oxygen evolution reaction (OER, charge process). Technically, GDEs can have different types of catalysts, including metal, non-metal and molecular catalysts, as well as enzymes and microbes [9].

Electrocatalysts able to sustain both oxygen reduction and oxygen evolution at high current densities are essential components of metal hydride/air secondary batteries. The most suitable electrocatalysts for ORR in alkaline media are platinum and its compounds/derivatives while IrO$_2$ and RuO$_2$ are suitable for the OER [10]. In fact, because of their high price, substitutes are sought so as to replace these materials. For the OER metal oxides with spinel structure are highly appropriate. The spinels have been broadly used as bifunctional oxygen electrocatalysts in alkaline media but their performance at practical current densities has been rarely reported. One of the reasons for that matter is that in order to operate as a bifunctional electrode at high current densities, the electrocatalyst should be placed into a GDE structure that allows a high flux of O$_2$ to the catalyst sites during battery discharge and effective removal of O$_2$ away from these sites during battery charge. Manganese has multiple crystallographic phases with different physical and chemical properties and one of its most stable forms is MnO$_2$. Generally, MnO$_2$ can exist in a number of phase structures such as α, β, γ, δ, ε, λ and so on [11-13]. In the current investigation the focus was on γ-MnO$_2$ as a catalyst for the OER due to its spinal structure. Another widely used catalyst for the OER is cobalt oxide [14]. The activity of the cobalt-based catalyst for the OER depends on the different oxidation states of cobalt (Co^{II}, Co^{III} and Co^{IV}) at the surfaces of the electrocatalysts [15, 16]. A commonly used catalyst mainly for the ORR is Ag. ORR mechanism in alkaline media may be

* To whom all correspondence should be sent:
E-mail: babrashev@iees.bas.bg

classified through two pathways, i. e. direct four-electron pathway and two-electron pathway. For the first pathway, one oxygen molecule receives $4e^-$ and is reduced to $4OH^-$. For the second pathway, the oxygen molecule is firstly reduced to o H_2O_2 or HO_2^- intermediate, then the intermediate transfers into electrolyte or is further reduced to OH^- *via* receiving $2e^-$ (indirect four-electron pathway) [17]. The silver in the general case catalyzes the direct $4e^-$ reaction pathway and also the HO_2^- anion disproportionation, being cheaper in comparison to conventional precious metal catalysts such as Pt, Au and Pd [18].

In our study we built the AL of the GDE using bimetallic catalysts and Teflon as a binder. For the gas diffusion layer, we applied teflonized carbon black and used a technology developed in IEES-BAS [19]. The aim of this study is to show the advantages of two of the most widely used electrocatalysts (γ-MnO₂ and Ag) in operation as bifunctional catalysts for ORR and OER. The obtained results were compared with the GDE with same GDL and different AL (Co₃O₄ and Ag). The focus of the current investigation is the influence of different catalysts on the electrochemical properties of GDE. Moreover, the varying ratio between the catalysts and their particle size is also studied.

EXPERIMENTAL

Electrode preparation

The GDL for both investigated GDEs was produced from Vulcan XC-72 R (Cabot corp., 30 nm particle size) which was modified by polytetrafluoroethylene (PTFE) (60 wt % dispersion in H_2O, 0.05-0.5 μm, Sigma Aldrich). The carbon blacks were teflonized up to 60 wt%. GDL was applied in a pressform completely covering its inner surface. The relative density of the layer was 50 mg.cm^{-2}. The AL was applied on the tightly placed GDL. It contains a bifunctional catalyst and 10 wt.% PTFE (10 μm particle size) powder (Sigma Aldrich), taken per the mass of catalysts. The bifunctional catalyst was composed, in one case of Co₃O₄ (Sigma Aldrich), particle size <50 nm + Ag (Ferro AG), particle size 4-30μm (30:70 wt.%) [19] and in the other case, after ratio optimization of γ-MnO₂ (EMD), particle size 40 μm and the same Ag (50:50 wt.%). The working area of the GDEs was 10 cm². The relative density of this layer is 40 mg.cm^{-2}, where the GDL was again applied by sealing the inner area of the pressform. A stainless steel mesh (Hebei Standard Filter Equipment), mesh count 100 was placed on top of the AL for the current collector.

Pressure of 300 kg.cm^{-2} was applied to the pressform for 3 minutes at 300˚C.

Experimental conditions

The charge/discharge tests were conducted using a six-channel Galvanostat 54 (PMC) testing system. The cell discharge was controlled by limiting time or voltage. The charge is defined by time up to 45 min and voltage limit up to +2 V and time up to 30 min and voltage limit -1 V for discharge, respectively. The polarization, charge/discharge tests and impedance analysis were carried out in a specially designed three-electrode half-cell configuration in 6M KOH - electrolyte and using reversible hydrogen electrode (RHE) (Gaskatel) for reference electrode, and stainless steel mesh as a counter electrode. The impedance measurements were conducted on GAMRY Instruments Reference 3000 potentiostat/ galvanostat in a frequency range of 100 kHz to 10 mHz with ten points per decade. Sine signal of 10 mV peak to peak was applied.

RESULTS AND DISCUSSION

Structure and morphology

XRD analysis (shown on Fig. 1) reveals a mixture of Ag/Co₃O₄ and a small amount of fcc-alloy (or CoC$_x$) and Ag/γ-MnO₂ for the respective catalysts. The XRD patterns do not show formation of new phases after the electrodes were used. A strong widening of the diffraction peaks of silver was observed due to the reduction in the size of the crystallites (Table 1).

The morphology of the catalysts, as well as of the GDEs prepared with them was examined using scanning electron microscopy (SEM). On Figs. 2 and 3 the microphotographs of the studied ALs of GDE at different magnifications are shown. From the SEM images in Fig. 2 it is clear how the smaller spherical Co₃O₄ particles cover the larger silver particles. At higher magnification (×3000 and × 10000) a layered structure is clearly observed. In Fig. 3, in the AL prepared from a mixture of Ag/γ-MnO₂, rough morphology and homogeneous particle distribution of the two catalysts are observed. Additionally, the smaller irregularly shaped silver particles, which are in a fairly wide range, almost completely envelop the larger particles of γ-MnO₂. The microphotographs of the different GDEs show significant differences in the particles' morphology and size as well.
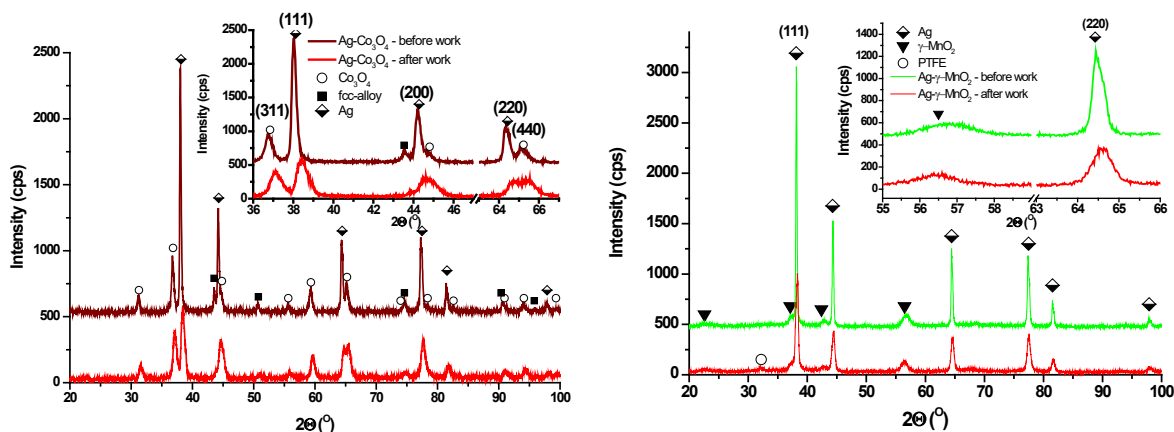
Fig. 1. XRD phase analysis of the prepared electrodes with bimetallic structure (Ag/Co$_3$O$_4$ and Ag/γ-MnO$_2$) before and after work

Table. 1. XRD parameters of GDEs with different AL

	Phases	Average crystalline size, nm	
		Ag	Co$_3$O$_4$ or MnO$_2$
Ag-Co$_3$O$_4$-before work	Ag+Co$_3$O$_4$, fcc-alloy	49	18
Ag-Co$_3$O$_4$-after work	Ag+Co$_3$O$_4$, fcc-alloy	15	13
MnO$_2$-Ag-before work	Ag+γ-MnO$_2$	50	8
MnO$_2$-Ag-after work	Ag+γ-MnO$_2$ PTFE	18	8
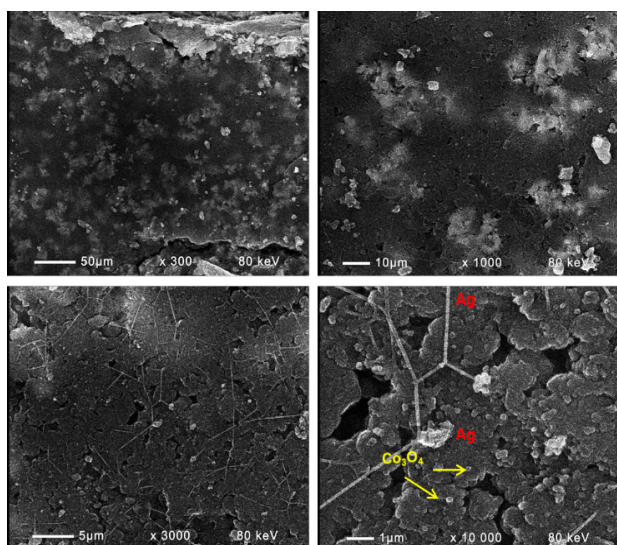
Fig. 2. SEM micrographs of GDE with bimetallic AL (Ag/Co$_3$O$_4$)

Fig. 3. SEM micrographs of GDE with bimetallic AL (Ag/γ-MnO$_2$)

BET analysis

A study by BET analysis revealed a high specific surface area of the gas diffusion layer (GDL) in GDEs with bi-metallic catalysts in the AL. The average size of the mesopores is about 10.7 nm which is a prerequisite for the predominance of Knudsen diffusion. The presence of this type of diffusion is also a prerequisite for the fastest and most efficient access of oxygen to the catalytic surface and is the reason for the high values of diffusion-limited current density i$_d$ (for ORR).The undergoing of this type of diffusion is also one of the explanations for the good discharge characteristics of these GDEs. Moreover, the BET analysis has given another important information that the GDL has a high specific surface area of 118.8 m²·g^{-1} and total pore volume (for pores smaller than 132 nm) of 0.318 cm³·g^{-1}, which is probably another reason for the facilitated access of oxygen to the AL.
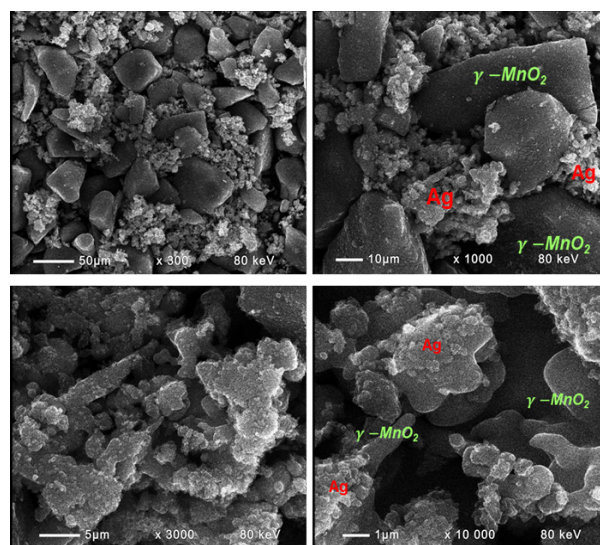
Electrochemical characterization
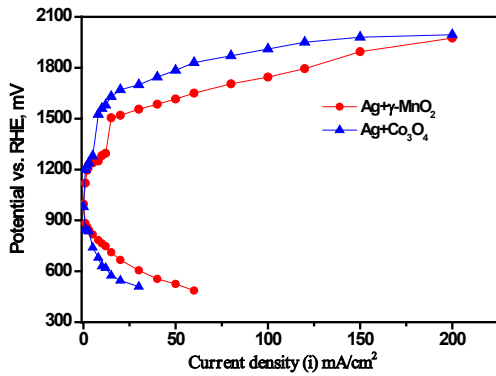
Fig. 4. Polarization curve of GDEs with different CL

On Fig. 4 the volt-ampere characteristics of the investigated GDEs are shown. It can be clearly seen that the use of the mixture Ag/Co_3O_4 for the obtaining of the AL in the GDE current density of 30 mA.cm^{-2} was achieved for the ORR. With replacement of the Co_3O_4 with γ - MnO_2 the applied current density for the electrochemical discharge considerably increases – up to 60 mA.cm^{-2}. Moreover, the GDE efficiency standard for OER is potential-E_{10} [20]. For the investigated GDEs the values were E_{10}=1295 mV for Ag/Co_3O_4 AL and E_{10}= 1282 mV for Ag/γ-MnO_2, which additionally confirmed the good electrochemical behavior of the two investigated GDEs. With the use of the two mixtures of bi-metallic catalysts a leap is observed in the interval of 1200-1550 mV in the polarization curves of the silver containing electrode. That effect was carefully studied by Amin [21] and is related to the formation of Ag_2O and/or $Ag^IAg^{III}O_2$ during the OER. Long-term tests of the two GDEs showed very good mechanical stability of over 300-500 charge/ discharge cycles (Fig. 5a) and b)). That is also confirmed by the very smooth increase (almost insignificant) of polarization between the first and last cycle at GDE with Ag/γ-MnO_2 structure (Fig. 5 b).
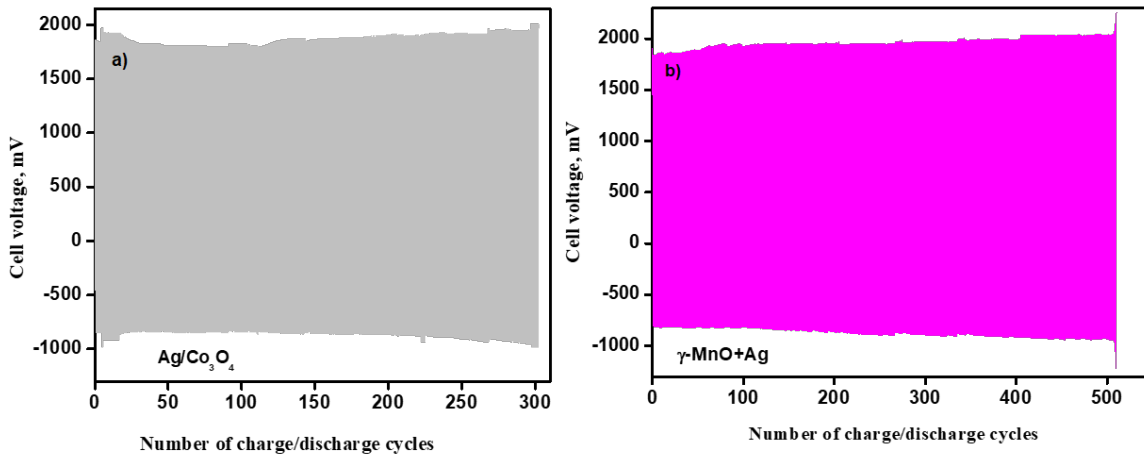
Fig. 5. Durability test of the GDEs with a) Ag/Co_3O_4 and b) Ag/γ-MnO_2
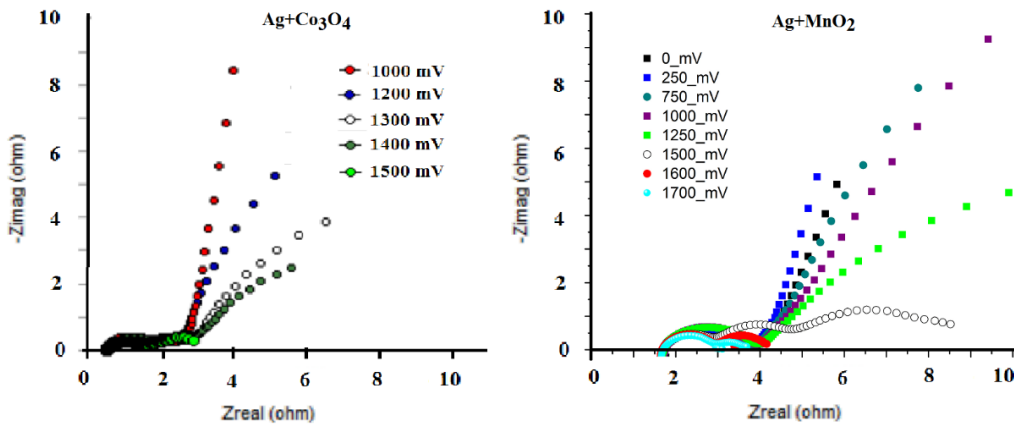
Fig. 6. Nyquist plots of impedance spectra of the GDEs with Ag/Co_3O_4 and Ag/γ-MnO_2.

EIS investigations

Fig. 6 shows the Nyquist plots of the Ag/Co$_3$O$_4$ and Ag/γ - MnO$_2$ electrodes at different potentials. From high to medium frequencies, the impedance spectra consist of partially overlapping semicircles and remain almost unchanged with increasing potential mainly due to the heterogeneous structure of the electrodes (the resistance of the pores, particles and boundaries between them) without a contribution by the electrochemical processes. Conversely, the impedance at low frequencies depends on the applied potential and reflects the electrochemical behavior of the electrodes. At lower potentials, far from the OER potential, the electrode behaves as a pseudocapacitor (slanted line) due to the formation of an electric double layer. As the potential increases, the line at low frequencies gradually bends and a new depressed semicircle with decreasing diameter is formed in a result of the OER with a decreasing charge transfer resistance (Rct). At the higher potentials (over 1500 mV) Rct becomes very small and the semicircle is not distinguished.

CONCLUSIONS

GDEs with different AL (Ag/Co$_3$O$_4$ and Ag/γ-MnO$_2$) and same GDL were investigated with modern physical and electrochemical methods. From these studies, it was found out that the equable weight distribution of the two catalysts (1:1) with Ag/γ-MnO$_2$ and their almost equal particle sizes give good results (higher than those with cobalt and silver) in the operation of the secondary GDE. Statistically, this morphology also determines a homogenous distribution of the pores (observed in the SEM microphotograph), from which it follows that the active sites for the two oxygen reactions are almost equally distributed in the volume of the catalytic layer. The EIS analysis gives the impression that the electrochemical behavior of the investigated GDEs also shows a behavior similar to that of supercapacitors. In future studies, more thorough attention will be paid to this fact.

REFERENCES

1. B. Abrashev, M. Slavova, E. Mladenova, V. Terziev, B. Burdin, G. Raikova, K. Petrov, *Journal of Chemical Technology and Metallurgy*, **56** (6), 1261 (2021).
2. C. Wang, Y. Yu, J. Niu, Y. Liu, D. Bridges, X. Liu, J. Pooran, Y. Zhang and A. Hu, *Applied Sciences*, **9** (14), 2787 (2019).
3. J. Yi, P. Liang, X. Liu, K. Wu, Y. Liu, Y. Wang, Y. Xia, J. Zhang, *Energy Environ. Sci.*, **11**, 3075 (2018).
4. L. Yaqoob, T. Noor, N. Iqbal, *Journal of Energy Storage,* **56**, 106075 (2022).
5. M. Karwowska, T. Jaron, K. J. Fijalkowski, P. J. Leszczynski, Z. Rogulski, A. Czerwinski, *J. Power Sources*, **263,** 304 (2014).
6. Y. J. Wang, B. Fang, D. Zhang, A. Li, D. P. Wilkinson, A. Ignaszak, L. Zhang, J. Zhang, *Electrochem. Energy Reviews*, **1**, 1 (2018).
7. A. G. Olabi, E. T. Sayed, T. Wilberforce, A. Jamal, A. H. Alami, K. Elsaid, S. M. A. Rahman, S. K. Shah, M. A. A., *Energies*, **14**, 7373 (2021).
8. H. Aldave, E. Andreoli, *Catalysts*, **10**, 713 (2020).
9. R. Ponnusamya, R. Venkatesanb, M. Kandasamyc, B. Chakrabortyd, C. S. Routa, *App. Surface Science*, **487**, 1033 (2019).
10. J. Zhang, Q. Zhou, Y. Tang, L. Zhang, Y. Li, *Chem. Sci.*, **10**, 8924 (2019).
11. H. Radinger, P. Connor, R. Stark, W. Jaegermann, B. Kaiser, *Chem. Cat. Chem.*, **13**, 1175 (2021).
12. S. Dey, V. V. P. Kumar, *Current Research in Green and Sustainable Chemistry,* **3**, 100012 (2020).
13. D. Pletcher, X. Li, S. W. T. Price, A. E. Russell, T. Sönmez, S. J. Thompson, *Electrochim. Acta*, **188**, 286 (2016).
14. J. Shin, J. K. Seo, R. Yaylian, A. Huang, Y. S. Meng, *International Materials Reviews*, **65**, 6 (2020).
15. X. He, F. Yin, G. Li, *Int. J. Hydrog. Energy*, **40**, 9713 (2015).
16. H. Osgood, S. V. Devaguptapu, H. Xu, J. Cho, G. Wu, *Nano Today*, **11,** 601 (2016).
17. Q. Liu, Z. Pan, E. Wang, L. An, G. Sun, *Energy Storage Materials*, **27**, 478 (2020).
18. F. W. T. Goh, Z. Liu, X. Ge, Y. Zong, G. Du, T. S. A. Hor, *Electrochim. Acta*, **114**, 598 (2013).
19. B. Abrashev, D. Uzun, A. Kube, N. Wagner, K.Petrov, *Bulg. Chem. Comm.*, **52** (2), 245 (2020).
20. M. Tahira, L. Pana, F. Idreesd, X. Zhanga, L. Wanga, J. J. Zoua, Z. L. Wangb, *Nano Energy*, **37**, 136 (2017).
21. H. M. A. Amin, H. Baltruschat, D. Wittmaier, K. A. Friedrich, *Electrochim. Acta*, **151**, 332 (2015).

Acknowledgement to Reviewers for vol. 54 (2022)

A

A. Ahmedova
A. Angelov
A. Angelova
A. Chandra
A. Dakova
A. Das
A. Georgiev
A. Ivanova
A. Kacal
A. Kazakova
A. Kudussov
A. Kumar
A. Kurutos
A. Momchilov
A. Naydenov
A. Nedelcheva
A. Petkova
A. Stoyanova
A. Tajer
A. Trendafilova
A. Viraneva
A. Wordu
A. Zlatkov

B

B. Angelova
B. Banov
B. Izgi
B. Nagaraja
  Ganesh
B. Todorov
B. Trusheva

C

C. Andreeva
C. Doncheva

D

D. Christova
D. Dakova
D. Dimitrov
D. Dzhonova
D. Grabcheva
D. Karashanova
D. Sakar
D. Tsekova
D. van der Merwe
Dh. Singh
Dr. Yankov
Dzh. Uzun

E

E. Balabanova
E. Chorbadzhijska
E. Kirilova
E. Razkazova-
  Velkova
E. Velcheva
E. Yakar

F

F. Sapundzhi

G

G. Antova
G. Cholakov
G. Dyankov
G. Exner
G. Issa
G. Kadinov

H

H. Suleman
Hr. Boyadjiev

I

I. Belovski
I. Dimitrova
I. Hinkov
I. Iordanov
I. Ivanov
I. Ivanova
I. Karadjova
I. K. Petkov
I. Mihailova
I. R. Nasrra
I. Filipova
I. Tsibranska
I. Vlaeva
I. Zagranyarska
Il. Ivanov

J

J. Hristov
J. Kaneti
J. Neikova
J. Petkova
J. Raikova

K

K. Alipieva
K. Boshnakov
K. Girginov
K. Danova
Kr. Dobreva
K. Ivanov
K. Jotovska
K. Kamarska
K. Nikolova
K. Petrov
K. Temelkov
K. Tomova

L

L. Ljutskanov
L. Vezenkov

M

M. Abrashev
M. Aleksandrova
M. Atanasova
M. Chaikova
M. Kamenova-
  Racheva
M. Gaidarova
M. Goel
M. Krysteva
M. Lazarova
M. Marudova
M. Mitov
M. Mitrev
M. Nikolova
M. Popova
M. Ravutsov
M. Rogozherov
M. Slavova
M. Stoev
M. Stoyanova
M. Traikov
M. Yamashita

N

N. Boshkov
N. Burdzhiev
N. Dimitrova
N. Dishovski
N. Markova
N. Minkovski
N. Petkova
N. Rizov
N. Sertova

N. Velinov

O

O. Ismail

P

P. C. Tomar
P. Denev
P. Ivanov
P. Phuenghphai
P. Popova-
  Krumova
P. Tashev
Pl. Angelov
Pl. Petkov

R

R. Arora
R. Bakalska
R. Georgieva
R. Kumar
R. Lyapchev
R. Popov
R. Rashkov
R. Tomova
R. Vasileva

S

S. Angelova
S. Barman
S. Gulia
S. Gyurov
S. Karakashev
S. Kasarova
S. K. Samanta
S. Lavrova
S, Manev
S. Marinova
S. N. Gummadi

S. Nenkova
S. Singh
S. Vladimirova
S. Vlaev
Sh. Agraval
Sh. K. Djain
Sh. Yu
Sn. Bakalova
St. Damyanova
Sv. Danova
Sv. Simeonov
Sv. Zhivkova

T

T. Paipanova
T. Petrova
T. Sandu
T. Stefanova
T. Stoyanov
T. Yoncheva
T. Yovcheva
Ts. Babeva
Ts. Doncheva
Ts. Rangelov

U

U. Sampath

V

V. Bankova
V. Bagdasarian
V. Beschkov
V. Cholakov
V. Chonova
V. Deneva
V. Gandova

V. Gochev
V. Deneva
V. Ilcheva
V. Karadzhova
V. Kozhuharov
V. Kurteva
V. K. Gupta
V. Kulkarni
V. Manev
V. Mihailova
V. Pandey
V. Toteva

Y

Y. Georgiev
Y. Yalcin
   Gurkan
Ya. Mitrev
Ya. Petkova

Z

Z. Burieva
Zh. Petkova
Zh. Wing

Instructions about Preparation of Manuscripts

General remarks: Manuscripts are submitted in English by e-mail. The text must be prepared in A4 format sheets using Times New Roman font size 11, normal character spacing. The manuscript should not exceed 15 pages (about 3500 words), including photographs, tables, drawings, formulae, etc. Authors are requested to use margins of 2 cm on all sides.

Manuscripts should be subdivided into labelled sections, e.g. INTRODUCTION, EXPERIMENTAL, RESULTS AND DISCUSSION, *etc*. **The title page** comprises headline, author(s)' names and affiliations, abstract and key words. Attention is drawn to the following:

a) **The title** of the manuscript should reflect concisely the purpose and findings of the work. Abbreviations, symbols, chemical formulae, references and footnotes should be avoided. If indispensable, abbreviations and formulae should be given in parentheses immediately after the respective full form.

b) **The author(s)'** first and middle name initials and family name in full should be given, followed by the address (or addresses) of the contributing laboratory (laboratories). **The affiliation** of the author(s) should be listed in detail (no abbreviations!). The author to whom correspondence and/or inquiries should be sent should be indicated by an asterisk (*) with e-mail address.

The abstract should be self-explanatory and intelligible without any references to the text and containing up to 250 words. It should be followed by keywords (up to six).

References should be numbered sequentially in the order, in which they are cited in the text. The numbers in the text should be enclosed in brackets [2], [5, 6], [9−12], etc., set on the text line. References are to be listed in numerical order on a separate sheet. All references are to be given in Latin letters. The names of the authors are given without inversion. Titles of journals must be abbreviated according to Chemical Abstracts and given in italics, the volume is typed in bold, the initial page is given and the year in parentheses. Attention is drawn to the following conventions: a) The names of all authors of a certain publications should be given. The use of "*et al*." in the list of references is not acceptable; b) Only the initials of the first and middle names should be given. In the manuscripts, the reference to author(s) of cited works should be made without giving initials, e.g. "Bush and Smith [7] pioneered...". If the reference carries the names of three or more authors it should be quoted as "Bush *et al*. [7]", if Bush is the first author, or as "Bush and co-workers [7]", if Bush is the senior author.

Footnotes should be reduced to a minimum. Each footnote should be typed double-spaced at the bottom of the page, on which its subject is first mentioned. **Tables** are numbered with Arabic numerals on the left-hand top. Each table should be referred to in the text. Column headings should be as short as possible but they must define units unambiguously. The units are to be separated from the preceding symbols by a comma or brackets. Note: The following format should be used when figures, equations, *etc*. are referred to the text (followed by the respective numbers): Fig., Eqns., Table, Scheme.

Schemes and figures. Each manuscript should contain or be accompanied by the respective illustrative material, as well as by the respective figure captions in a separate file. As far as presentation of units is concerned, SI units are to be used. However, some non-SI units are also acceptable, such as °C, ml, l, etc. Avoid using more than 6 (12 for review articles) figures in the manuscript. Since most of the illustrative materials are to be presented as 8-cm wide pictures, attention should be paid that all axis titles, numerals, legend(s) and texts are legible.

The authors are required to submit the text with a list of three individuals and their e-mail addresses that can be considered by the Editors as potential reviewers. Please note that the reviewers should be outside the authors' own institution or organization. The Editorial Board of the journal is not obliged to accept these proposals.

The authors are asked to submit **the final text** (after the manuscript has been accepted for publication) in electronic form by e-mail. The main text, list of references, tables and figure captions should be saved in separate files (as *.rtf or *.doc) with clearly identifiable file names. It is essential that the name and version of the word-processing program and the format of the text files is clearly indicated. It is recommended that the pictures are presented in *.tif, *.jpg, *.cdr or *.bmp format.

The equations are written using "Equation Editor" and chemical reaction schemes are written using ISIS Draw or ChemDraw programme.

EXAMPLES FOR PRESENTATION OF REFERENCES

REFERENCES

1. D. S. Newsome, *Catal. Rev.–Sci. Eng*., **21**, 275 (1980).
2. C.-H. Lin, C.-Y. Hsu, *J. Chem. Soc. Chem. Commun*., 1479 (1992).
3. R. G. Parr, W. Yang, Density Functional Theory of Atoms and Molecules, Oxford Univ. Press, New York, 1989.
4. V. Ponec, G. C. Bond, Catalysis by Metals and Alloys (Stud. Surf. Sci. Catal., vol. 95), Elsevier, Amsterdam, 1995.
5. G. Kadinov, S. Todorova, A. Palazov, in: New Frontiers in Catalysis (Proc. 10th Int. Congr. Catal., Budapest (1992), L. Guczi, F. Solymosi, P. Tetenyi (eds.), Akademiai Kiado, Budapest, 1993, Part C, p. 2817.
6. G. L. C. Maire, F. Garin, in: Catalysis. Science and Technology, J. R. Anderson, M. Boudart (eds.), vol. 6, Springer Verlag, Berlin, 1984, p. 161.
7. D. Pocknell, *GB Patent* 2 207 355 (1949).
8. G. Angelov, PhD Thesis, UCTM, Sofia, 2001, pp. 121-126.
9. JCPDS International Center for Diffraction Data, Power Diffraction File, Swarthmore, PA, 1991.
10. CA **127**, 184 762q (1998).
11. P. Hou, H. Wise, *J. Catal.*, in press.
12. M. Sinev, private communication.
13. http://www.chemweb.com/alchem/articles/1051611477211.html.

Texts with references which do not match these requirements will not be considered for publication!!!

CONTENTS